Thèse n° 9196

Skyrmion Control and Phase Transitions in Cu_2OSeO_3

Présentée le 5 juillet 2022

Faculté des sciences de base
Laboratoire de magnétisme quantique
Programme doctoral en physique

pour l'obtention du grade de Docteur ès Sciences

par

Thomas SCHÖNENBERGER

Acceptée sur proposition du jury

Prof. L. Villard, président du jury
Prof. H. M. Rønnow, Prof. F. Carbone, directeurs de thèse
Prof. A. Rosch, rapporteur
Dr J. White, rapporteur
Dr M. Cantoni, rapporteur

École
polytechnique
fédérale
de Lausanne

2022

Abstract

Magnetic skyrmions are nanometric and non-trivial spin textures with non-zero topological charge. Their robustness against perturbations and the possibility to control them using external stimuli make them ideal candidates for future spintronic applications. In particular the magnetoelectric skyrmion host Cu_2OSeO_3 holds a lot of promise for low power devices since skyrmions in this compound can be controlled by electric fields alone. Using Lorentz transmission electron microscopy to perform real space and real time biasing experiments on thin lamellas of Cu_2OSeO_3 in a geometry that is most suitable for technological applications, we observe reproducible creation and annihilation of skyrmions. For a more quantitative analysis, we develop new feature detection algorithms to reliably extract skyrmion positions even in noisy images. We further produce first prototypes of a multiarray device to enable local skyrmion switching.

Due to its low pinning, Cu_2OSeO_3 allows for the formation of large and well-arranged triangular skyrmion lattices. This makes this compound a perfect testbed to study the evolution of skyrmion configurations under external stimuli. Experiments are carried out again using Lorentz transmission electron microscopy on thin lamellas of Cu_2OSeO_3. We investigate how defects in skyrmion lattices are arranged at grain boundaries and develop algorithms to extract them and to directly visualize their alignment. These defects are at the core of the melting of skyrmion lattices in this system. We show that a controlled magnetic field ramp can induce skyrmion ensembles in Cu_2OSeO_3 to transition from a two-dimensional solid through a thus far unknown ordered liquid phase called the hexatic phase, to a liquid. We find that this transition is a topological defect-induced two-step process as predicted by the Kosterlitz-Thouless-Halperin-Nelson-Young (KTHNY) theory. Finally, we go beyond equilibrium phenomena to explore the effect of quenching the system from its liquid phase to its solid phase using different quench rates and find first evidence that our system belongs to the Kibble-Zurek universality class.

Keywords: magnetism, skyrmions, magnetoelectric materials, focused ion beam, Lorentz transmission electron microscopy (LTEM), image analysis, defects, dislocations, disclinations, grain boundaries, phase transitions, melting, skyrmion solid phase, skyrmion hexatic phase, skyrmion liquid phase, KTHNY theory, Kibble-Zurek mechanism

Zusammenfassung

Magnetische Skyrmionen sind topologisch nicht-triviale Spin-Strukturen auf der Nanometerskala, die sich durch eine ausserordentliche Stabilität gegenüber äusseren Störungen auszeichnen. Gleichwohl können sie kontrolliert manipuliert werden und sind dadurch Gegenstand aktiver Forschung im Hinblick auf zukünftige spintronische Anwendungen. Insbesondere Cu_2OSeO_3 ist aufgrund seiner einzigartigen magnetoelektrischen Eigenschaften ein potentieller Kandidat für energieeffiziente Anwendungen, da Skyrmionen in diesem Material durch elektrische Felder allein kontrolliert werden können. Mittels Lorentz Tranmissionselektronenmikroskopie untersuchen wir im direkten Raum und in Echtzeit erstmalig die Erzeugung und Vernichtung von Skyrmionen in Cu_2OSeO_3 in einer für technologische Anwendungen nutzbaren Geometrie. Zur quantitativen Datenauswertung des Bildmaterials entwickeln wir eine Reihe neuer Algorithmen zur Merkmalerkennung, mit einem besonderen Augenmerk auf eine zuverlässige Idenfikation von Skyrmionen in verrauschten Bildern. Wir entwicklen darüber hinaus erste Prototypen eines 4-bit grossen adressierbaren Skyrmionenspeichers.

In Cu_2OSeO_3 lösen sich Skyrmionen effizient aus der atomaren Kristallstruktur heraus und bilden daher geordnete und grosse Skyrmionengitter aus. Deswegen eignet sich diese Verbindung besonders um die Entwicklung von Skyrmionen-Ensembles unter dem Einfluss von äusseren Anregungen zu untersuchen. Die Experimente werden wieder mit Hilfe der Lorentz-Transmissionselektronenmikroskopie an Lamellen aus Cu_2OSeO_3 durchgeführt. Wir untersuchen, wie sich Defekte in Skyrmionengittern an Korngrenzen anordnen und entwickeln Algorithmen, um sie zu extrahieren und ihre Ausrichtung direkt zu visualisieren. Diese Defekte stehen im Mittelpunkt des Schmelzprozesses von Skyrmionengittern in diesem System. Wir zeigen, dass eine kontrollierte Magnetfeldrampe Skyrmionen-Ensembles in Cu_2OSeO_3 von einem zweidimensionalen Festkörper über eine bisher unbekannte geordnete flüssige Phase, die sogenannte hexatische Phase, in eine Flüssigkeit übergehen lässt. Wir stellen fest, dass dieser Übergang ein durch topologische Defekte induzierter zweistufiger Prozess ist, wie er von der Kosterlitz-Thouless-Haplerin-Nelson-Young-Theorie (KTHNY) vorhergesagt wird. Schließlich gehen wir über Gleichgewichtsphänomene hinaus und untersuchen den Übergang von der flüssigen in die feste Phase bei erschiedenen Kühlraten und finden erste Hinweise darauf, dass dieses System zur Kibble-Zurek-Universalitätsklasse gehört.

Schlüsselwörter: Magnetismus, Skyrmionen, magnetoelektrische Materialien, fokussierter Ionenstrahl, Lorentz-Transmissionselektronenmikroskopie, Bildanalyse, Defekte, Disloka-

tionen, Disklinationen, Korngrenzen, Phasenübergänge, Schmelzen, Skyrmion-Festphase, Skyrmion-Hexatphase, Skyrmion-Flüssigphase, KTHNY, Kibble-Zurek-Mechanismus

Résumé

Les skyrmions magnétiques sont des textures de spin nanométriques et non triviales avec une charge topologique non nulle. Leur robustesse face aux perturbations et la possibilité de les contrôler à l'aide de stimuli externes en font des candidats idéaux pour les futures applications spintroniques. En particulier, l'hôte magnétoélectrique de skyrmions Cu_2OSeO_3 est très prometteur pour les dispositifs à faible consommation puisque les skyrmions dans ce composé peuvent être contrôlés uniquement par des champs électriques. En utilisant la microscopie électronique à transmission de Lorentz pour réaliser des expériences de polarisation en espace réel et en temps réel sur de fines lamelles de Cu_2OSeO_3 dans une géométrie qui convient le mieux aux applications technologiques, nous observons la création et l'annihilation reproductibles de skyrmions. Pour une analyse plus quantitative, nous développons de nouveaux algorithmes de détection de caractéristiques pour extraire de manière fiable les positions des skyrmions, même dans des images bruitées. Nous produisons également les premiers prototypes d'un dispositif multi-array permettant de contrôler les skyrmions localement.

En raison de son faible pinning, le Cu_2OSeO_3 permet la formation de grands réeseaux triangulaires de skyrmions bien rangées. Cela fait de ce composé un banc d'essai parfait pour étudier l'évolution des configurations de skyrmions sous l'effet de stimuli externes. Les expériences sont menées en utilisant à nouveau la microscopie électronique à transmission de Lorentz sur de fines lamelles de Cu_2OSeO_3. Nous étudions comment les défauts dans les réseaux de skyrmions sont arrangées aux bords de domaines et développons des algorithmes pour les extraire et visualiser directement leur alignement. Ces défauts sont au cœur de la fusion des réseaux de skyrmions dans ce système. Nous montrons qu'une rampe de champ magnétique contrôlée peut induire la transition des ensembles de skyrmions dans le Cu_2OSeO_3 d'un solide bidimensionnel à un liquide en passant par une phase liquide ordonnée jusqu'ici inconnue dans ce système, appelée phase hexatique. Nous constatons que cette transition est un processus en deux étapes induit par un défaut topologique, comme le prédit la théorie KTHNY. Enfin, nous allons au-delà des phénomènes d'équilibre pour explorer l'effet d'un refroidissement rapide du système, de sa phase liquide à sa phase solide en utilisant différents taux de refroidissement et nous trouvons une première preuve que notre système appartient à la classe d'universalité de Kibble-Zurek.

Mots clés : magnétisme, skyrmions, matériaux magnétoélectriques, faisceau d'ions focalisé,

microscopie électronique à transmission de Lorentz, analyse d'images, défauts, dislocations, disclinaisons, bords de domaines, transitions de phase, fusion, phase solide du skyrmion, phase hexatique du skyrmion, phase liquide du skyrmion, KTHNY, mécanisme de Kibble-Zurek

Contents

List of Figures

1 Introduction

Ancient cultures used myths and legends to explain our existence and the phenomena people observed. The Greek mythology in particular has a lasting impression on us still today. Just think about all the allusions in everyday life: a Sisyphean task, Cupid's arrows of love, the box of Pandora, the Midas touch… Companies also capitalize on the reputation of some Greek gods: Nike's shoes carry runners to victory and Venus' razors promise smooth legs just like the ones of the Greek goddess. A less well-known legend tells the story of the Greek shepherd Magnes who climbed Mount Ida located in what is now the northwest of Turkey with his flock of sheep. Suddenly, his iron-cleated sandals and staff stuck to the ground. It turned out to be lodestone, which is a rock rich in magnetite – an iron oxide. The first account of Magnes is found in Pliny the Elder's Naturalis Historia, almost 1000 years after a puzzled Magnes supposedly tried to kick off the magnetic lodestone from his sandals. It is the same mount Ida from which Zeus, the god of lightning, watched the fall of Troy. Indeed, lodestone becomes particularly magnetic when a bolt of lightning strikes. It passes a current of up to a million amps into the ground for a short time, which is sufficient to strongly magnetize lodestone in the near vicinity. Little did Magnes know that a whole scientific field would be named after him [1]. [1] While Zeus was less popular among the Chinese, they were way ahead of the Greeks to use lodestone in its first technological application as a compass. The earliest records date back to the first century BC. The Chinese were not a seafaring nation but used the compass for example to orient the streets of their cities from north to south. The changing true north of the earth magnetic field manifests in a misalignment of streets that were constructed in different ages, notably in ancient cities such as Beijing and Nanking [1].

For the longest time, the origin of magnetism were speculated about on a mostly metaphysical level. Only from the 17th century on it started to become common practice to test scientific theories with actual experiments and progress in our understanding of nature accelerated dramatically as a result. Alessandro Volta set out to conduct his own experiments in 1791

[1] Or according to some different accounts after the region of Magnesia not far away from Mount Ida, where lodestone is common as well [1].

soon after he heard about the "animal electricity" that his colleague Galvani discovered when dissecting frog legs. After he noticed an acidic taste when putting tin foil on his tongue, he realized that it was metals that generated electricity and not the animal tissue itself as originally reported by Galvani. This led him to construct the first battery, named Voltaic pile in his honour, composed of alternating layers of copper and zinc separated by a brine-soaked piece of cloth [1]. Volta invented a continuous source of electricity, which would go on to define the world we live in today. It would also allow physicists in the 19th century to actually understand magnetism on a fundamental level. As it turns out both of these phenomena are intimately related.

Then and now, many great discoveries are the result of a lucky coincidence. This was not different for Hans Christian Oersted, when he discovered how a current-carrying wire (fed by a Voltaic pile) deflected a compass needle. Ampere grasped the importance of these experiments when he reasoned that if one current-carrying wire behaves like a magnet, two current-carrying wires should likewise repel or attract each other depending on which direction the current would flow. Indeed, this is what he found in his experiments, which in turn led Biot and Savart to find that the force between those wires decreases with the distance as an inverse square law, known as Biot-Savart's law today.
The impact of Michael Faraday on the understanding of magnetism still resonates today. The autodidact merged electricity and magnetism to spawn the new field of electromagnetism. He discovered how a surge of current in one copper wire coil induced a current in another coil. With this, not only did he discover electromagnetic induction, but also a prototype transformer. He also devised the first dynamo, and most famously, the enclosure to shield electromagnetic fields, the Faraday cage. His investigations into how light interacts with magnetism led to the discovery of the Faraday-effect, which describes how the polarization of linearly polarized light rotates under the influence of a magnetic field [1]. He further speculated whether the opposite would be true as well: namely an oscillating field which would give rise to a magnetization. Almost two centuries later, the inverse Faraday-effect is at the heart of cutting edge research in controlling magnetism on ultra-short timescales using femtosecond lasers [2].
James Clerk Maxwell finally formalized many of Faraday's ideas into a simple and elegant form known as the Maxwell equations. They describe how electric fields, magnetic fields, charges and currents are related to each other and are valid for any material at any length scale. A direct consequence of these equations is that light propagates as an electromagnetic wave. About two decades later in 1886, Heinrich Hertz for the first time generated and detected electromagnetic waves in the radio frequency range.

But why are current carrying wires magnetic and what makes a fridge magnet stick to the fridge door? What does magnetic even mean? This leads to one of the most famous theories in physics: the special theory of relativity as developed by Einstein in the early 1900s. The title of the paper was actually "On the Electrodynamics of Moving Bodies" hinting at its origin in describing the electrodynamics of moving charges [3]. Imagine a current-carrying wire with a positively charged bee flying along its side. The wire itself is electrically neutral with the stationary positive charges in the wire compensating for the moving electrons. But these electrons create a magnetic field such that the moving positive bee is deflected off its straight trajectory. In the frame of reference of the bee, though, the positive charges in the wire are contracted such that to the bee, the wire looks positively charged and it is repelled from the wire. Therefore, it is purely a result of the frame of reference one chooses that determines whether one sees a magnetic field, an electric field or a combination of both. Magnetism and electricity in fact are manifestations of each other and not separate phenomena. In other words: magnetism is the result when electrostatics meets special relativity [3].

What about magnetic lodestone then? Nothing is moving there, right? In fact, a whole lot is moving. Electrons zoom in orbits around the atomic nuclei and the same relativistic effects are at play to give rise to an orbital magnetic moment, which however only plays a minor role in the overall magnetism that for instance makes a magnet stick to the fridge door.
To fully understand magnetism in matter we need quantum mechanics, also developed at the beginning of the 20th century by Bohr, Heisenberg, Schrödinger, Pauli, and Dirac, just to name a few. It describes how objects both have a particle and wave nature, physical quantities are quantized and that there are limits to how accurate measurements can be. For our everyday world, it is the theory of everything to describe how things are the way they are and how they work [4]. People soon realized that magnetism is an important consequence of electrons moving in atomic orbits. A full relativistic quantum mechanical treatment furthermore explains the existence of a fundamental particle property: the spin.
Put simply, it is as if a particle was rotating around itself to create its own magnetic moment. Quantum mechanics tells us how the orbitals and shells that electrons can occupy in an atom look like (determined by the solution of the Schrödinger equation) and in which direction the electron spins are pointing. In filled electron shells, all electrons are paired. They whiz in opposite directions and their spins add up to zero. But in half-filled shells all spins point the same way and add up. This is why elements at the edge of the main group of the periodic table with filled or almost filled outer electron shells tend to be non-magnetic, while elements in the middle of the main group tend to be magnetic, such as chromium, manganese, iron, cobalt and nickel.
On a crystal level, and in a first approximation, these atomic magnetic moments can either align (ferromagnetic) or anti-align (antiferromagnetic). Which of the two applies is dictated by how the wave functions of the electrons and atoms overlap and what this means in terms of the resulting energy. A little more explanation is provided in the following chapter. As a result, the spins in a ferromagnet such as iron align along the same direction giving rise to a magnetic field, while for example Chromium is one of the most antiferromagnetic materials. In his Nobel prize lecture, Louis Néel, who discovered antiferromagnetism, famously said that antiferromagnets are “extremely interesting from a theoretical point of view, but do not seem to have any application” [5]. Nevertheless, today it is an active field of research and applications may be found in the next generation of fast and dense storage devices [6]. Néel also generalized antiferromagnetism to a case where the anti-aligned spins do not fully cancel out, giving rise to a net magnetization, and which he called ferrimagnetism. It is magnetite in

fact, used in Chinese compasses millennia ago and sticking to the shoes of old Magnes, that falls precisely into this category.

This is one reason why magnetism is such a fascinating field: it spans across such a wide range of physics and applications and it continues to be an exciting field full of surprises. A whole new arena of fundamental research opened up when experimental evidence for a completely different kind of spin configuration, magnetic skyrmions, were first found in 2009 [7]. Skyrmions are tornado-like swirling spin structures with unique properties that make them ideal candidates for a whole range of possible devices from magnetic storage media, spintronic devices to computing.

Thesis outline

This thesis deals with skyrmions both from an applied and fundamental perspective and with a strong experimental focus. All observations are performed in real space and real time using Lorentz transmission electron microscopy (LTEM) and the focused ion beam (FIB) plays a central role in sample preparation. Both these techniques will be present throughout this thesis. This work is organized in the following way:

- After a historical introduction into magnetism in the first chapter, we introduce basic notions of magnetism in the second chapter: from the basic interactions between electron spins to how this can give rise to complex magnetic textures such as skyrmions. An overview of various skyrmion hosting compounds is presented with a focus on the magnetoelectric skyrmion host Cu_2OSeO_3 that most experiments in this work have been performed on. The main experimental techniques are introduced. The basics of photolithography and clean room processes are briefly outlined. A strong emphasis is put on the description of the FIB technique that has been used for every sample studied in this work and best practices to reproducibly fabricate high quality lamellas for TEM observation. Last but not least, the TEM is introduced. Using the Lorentz mode, it is an ideal technique for real space and real time in-situ experiments on magnetic materials and for the study of nanoscale magnetic structures.

- The third chapter deals with one of the main projects of this thesis: real time observations of the electric field control of skyrmions in Cu_2OSeO_3. The sample preparation procedure is presented for a geometry that is most suitable for technological applications: when the active device – the TEM lamella – is sandwiched between a pair of electrodes. We manage to reliably create and erase skyrmions and develop robust image analysis algorithms that can extract skyrmions in noisy images for further quantitative analysis. These include switching behaviour over time, write and erase times and hysteresis loops. We further develop first prototypes with a multiarray geometry, a first step towards the first 4-bit random access skyrmion memory.

- The third part of this thesis comprises chapters four, five and six, whose common theme is topology and defects. The fourth chapter introduces the concept of defects in a two dimensional lattice and presents an algorithm to systematically extract strings of defects in an automated manner to study and visualize the misalignment of adjacent skyrmion domains. In the fifth chapter, the melting of skyrmion lattices is investigated. We show that the melting is a two-step defect-mediated process in accordance with the famous theory of melting developed by Kosterlitz, Thouless, Halperin, Nelson and Young in the 1970s. As a result, we discover a new phase, the so called skyrmion hexatic phase between the known skyrmion solid and skyrmion liquid phases. Finally, in the sixth chapter, non-equilibrium phenomena are studied when freezing skyrmion liquids into their solid phase using quench rates covering multiple orders of magnitude. The higher the quench rate, the sooner the system falls out of equilibrium, meaning that it cannot follow the change of the control parameter (temperature or magnetic field) fast enough and therefore freezes. We find first evidence that the skyrmion domain sizes at the freeze-out point as a function of the quench rate follow a universal scaling law known as the Kibble-Zurek mechanism that was originally proposed to account for the structure of our universe after the big bang.

To slightly adapt Louis Néel famous quote: all this is very interesting from a theoretical point of view, and who knows, maybe it will be useful as well at some point!

2 Theory and Experimental Methods

In this chapter we introduce the basic notions of magnetism, from ferro-, ferri-, antiferro- and chiral magnets. We introduce the concept of skyrmions, their main properties and material classes they appear in. We focus on one particular skyrmion host, Cu_2OSeO_3, which is most relevant in this thesis. Furthermore, we discuss the essential techniques used throughout this work, from the focused ion beam (FIB), cleanroom microfabrication and Lorentz transmission electron microscopy (LTEM).

2.1 Magnetism

One can distinguish two types of magnetic order: order induced by an external magnetic field (diamagnetism and paramagnetism) and spontaneous magnetic order without any applied field (ferro-, ferri-, and antiferroamgnetism). In that case, a spontaneous alignment of spins below the so called Curie temperature T_C in the case of ferromagnets and ferrimagnets and Neél temperature T_N in the case of antiferromagnets can be observed. Those three types of magnetic order are shown in figure 2.1.

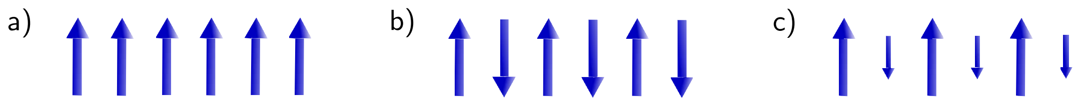

Figure 2.1: Various magnetic ground states: ferromagnetic order (a), antiferromagnetic order (b) and ferrimagnetic order (c).

In the ferromagnetic ground state all magnetic moments are parallel, whereas in the antiferromagnetic ground state all moments are antiparallel, so that the system can be subdivided into two-sublattices with equal magnetization. In the ferromagnetic case, a spontaneous magnetization can be measured whereas in the antiferromagnetic case there cannot. The ferrimagnetic ground state is a mixture of both, however a spontaneous magnetization can be measured. Therefore, ferromagnets such as iron, nickel or cobalt, are magnetically ordered even without any applied external field. The force that aligns the spins is due to the exchange interaction, which is a consequence of the interplay between Pauli principle, Coulomb- and Fermi-energy. When aligned parallel, the Pauli principle pushes the spins apart thus reducing the Coulomb energy. At the same time, the Fermi energy is raised for parallel alignment since there is only one spin orientation. This interplay leads to an effective interaction between spins. The same argument can be made for antiparallel spin alignment. Both parallel and antiparallel spin alignment can be expressed in terms of symmetric and antisymmetric wave functions. The energy difference of those states is the so called exchange integral or exchange constant J. For $J > 0$ parallel alignment is favoured (ferromagnetism) whereas for $J < 0$ antiparallel alignment is favoured (antiferromagnetism). For localised magnetic moments as created e.g. by the unfilled 4f-electron shells in rare earth metals, this can be cast into the Heisenberg-Hamiltonian as suggested by Heisenberg and Dirac. Its exchange part reads [8]

$$H_{ex} = -\frac{1}{2}\sum_{i,j} J_{ij}^{x} S_i^x S_j^x + J_{ij}^{y} S_i^y S_j^y + J_{ij}^{z} S_i^z S_j^z, \tag{2.1}$$

where J_{ij}^{α}, $\alpha = x, y, z$, are the exchange integrals between spins at lattice sites i and j with the unit of energy. The vectors $\boldsymbol{S}_i = \boldsymbol{\mu}_i/\mu_i$, with μ_i being the magnetic moment, denote the renormalised magnetic moments so that $|\boldsymbol{S}_i| = 1$. They can be referred to as "spin". It is customary to split up the interaction into an isotropic part, J_{ij}, and the deviation thereof in each direction, d_{ij}^x, d_{ij}^y and d_{ij}^z. Assuming $J_{ij} = J_{ij}^x$, then $J_{ij}^y = J_{ij} + d_{ij}^y$ and $J_{ij}^z = J_{ij} + d_{ij}^z$ so that the Hamiltonian can be rewritten as [8]

$$H_{ex} = -\frac{1}{2}\sum_{i,j} J_{ij}\boldsymbol{S}_i \cdot \boldsymbol{S}_j - \frac{1}{2}\sum_{ij} d_{ij}^y S_i^y S_j^y - \frac{1}{2}\sum_{ij} d_{ij}^z S_i^z S_j^z. \tag{2.2}$$

The first term describes the isotropic exchange while the other two describe an anisotropy in y- and z-direction, the so called two-ion anisotropy, which can be very strong, since it originates directly from the exchange interaction. However, in systems with high symmetry, this contribution is usually negligibly small.

The exchange interaction is very short ranged since wave functions decay rapidly with distance (at least in the case of localised electrons) and so does their overlap. Hence, it is sufficient in most cases to just consider nearest neighbour interaction, denoted by $< ij >$ in the sum. For a ferromagnet this means J_{ij} can be replaced by the constant J, which means isotropic exchange in space. The simplified exchange Hamiltonian then reads [9]

$$H_{ex} = -J \sum_{<ij>} \boldsymbol{S}_i \cdot \boldsymbol{S}_j \tag{2.3}$$

for a ferromagnet.

2.1.1 Anisotropic Contributions

Another anisotropic contribution is given by the magnetocrystalline anisotropy, or on-site anisotropy, originating from spin-orbit coupling and therefore related to the crystal structure. The spins align along a certain crystallographic axis. The simplest case is the so called uniaxial anisotropy, which for a ferromagnet with an easy z-axis reads [9]

$$H_K = -K \sum_i \left(S_i^z\right)^2, \tag{2.4}$$

with K being the anistropy constant. Other anisotropic contributions include for example the magnetostriction effect [10] that stretches a magnetic body in certain directions or the Dzyaloshinksii-Moriya interaction caused by a break of symmetry such as an impurity on the sample surface, an interface or a broken inversion symmetry of the crystal structure.

2.1.2 Dzyaloshinksii-Moriya Interaction

The Dzyaloshinksii-Moriya interaction (DMI) is an asymmetric exchange interaction originating from spin-orbit coupling that arises is systems with broken inversion symmetry [11, 12, 13]. Its contribution to the Hamiltonian is given by

$$H_{DM} = \boldsymbol{D}_{ij} \cdot (\boldsymbol{S}_i \times \boldsymbol{S}_j), \tag{2.5}$$

where $\boldsymbol{D}_{ij}$ is the DMI vector, whose direction and size is given by the symmetry of the surrounding ions. In contrast to the exchange interaction described before that aligns spins parallel, the DMI favours a canted spin arrangement. Together with the normal exchange interaction and the Zeeman contribution (see below) the DMI can generate complex magnetic textures such as spin helices or magnetic skyrmions, the main focus of this work.

2.1.3 Dipolar Contributions

Another anisotropic contribution has its origin in the shape of the magnetic sample due to dipolar interactions between the spins. It is much smaller than the exchange interaction but long-range so that more than only nearest neighbours need to be considered. The dipole-dipole interaction is also responsible for creating domains in a large magnetic system, which reduce the overall stray field and are therefore energetically favourable. The dipolar contribution to the Hamiltonian is given by [9]

$$H_\omega = -\sum_{i<j} \omega_i \frac{3(\boldsymbol{S}_i \cdot \boldsymbol{e}_{ij})(\boldsymbol{e}_{ij} \cdot \boldsymbol{S}_j) - \boldsymbol{S}_i \cdot \boldsymbol{S}_j}{r_{ij}^3}, \tag{2.6}$$

with $\omega_i = \mu_0 \mu_i^2 / 4\pi a^3$ describing the strength of the dipolar interaction with μ_0 being the vacuum permeability, μ_i the i-th magnetic moment and a being the lattice constant. $\boldsymbol{r}_{ij}$ is the vector connecting $\boldsymbol{S}_i$ and $\boldsymbol{S}_j$.

Zeeman Contribution

The last important contribution is the so called Zeeman term, which describes the interaction with an external magnetic field $\boldsymbol{H}$ and reads [9]

$$H_B = -\mu_0 \mu_s \boldsymbol{H} \cdot \sum_i \boldsymbol{S}_i. \tag{2.7}$$

2.2 Magnetic Skyrmions

The concept of skyrmions was originally proposed by Tony Skyrme in the 1960s as a concept in particle physics to describe the stability of hadrons from a topological point of view [14, 15, 16]. Thereafter the idea of skyrmions has been found to apply to various condensed matter systems from Bose-Einstein condensates, liquid crystals, quantum Hall systems [14] to ferromagnetic materials, which has recently spawned the whole new field of skyrmionics [17, 18]. They can be easily manipulated by external stimuli while being stable against perturbations because of their topology, which physically speaking translates into a high energy barrier. Extensive research efforts are hence undertaken to evaluate the possible role of skyrmions in low power storage devices [19, 20, 21], neuromorphic computing [22] and magnonic devices [23].

Skyrmions, as we understand them in the following, are localised spin textures with non-trivial topology. They feature a non-zero topological charge Φ defined by [14]

$$\Phi = \frac{1}{4\pi} \int \left(\frac{\partial \boldsymbol{n}}{\partial x} \times \frac{\partial \boldsymbol{n}}{\partial y} \right) d^2 \boldsymbol{r}, \tag{2.8}$$

where $\boldsymbol{n} = \boldsymbol{m}/|\boldsymbol{m}|$ is a unit vector parallel to the local magnetic moment $\boldsymbol{m}$. Typical spin configurations are shown in figure 2.2.

A topological charge of e.g. $\Phi = 1$ means the spins of a skyrmion wrap the unit sphere exactly once, see figure 2.2. Skyrmions generally have integer topological charge. Other parameters that characterise a skyrmion are its polarity p, its vorticity m and its helicity γ [25]. The polarity describes how the core spin is aligned with respect to the z-axis ($p = \pm 1$). The magnetization density can be expressed in spherical coordinates with azimuthal angle θ and polar angle ϕ. Since the magnetization density is continuous, the polar angle wraps around in multiples of 2π yielding the vorticity m. The differences in in-plane magnetizations are accounted for by the helicity γ. It is the angle of rotation around the z-axis of spins in a skyrmion with respect to a Neél skyrmion, which has helicity zero [24]. Bloch and Néel skyrmions both have equal topological charge and polarity, but different helicity. They are the most common magnetic skyrmions and shown in figure 2.2.

Various mechanisms are known to stabilize skyrmions. The combination of dipole-dipole

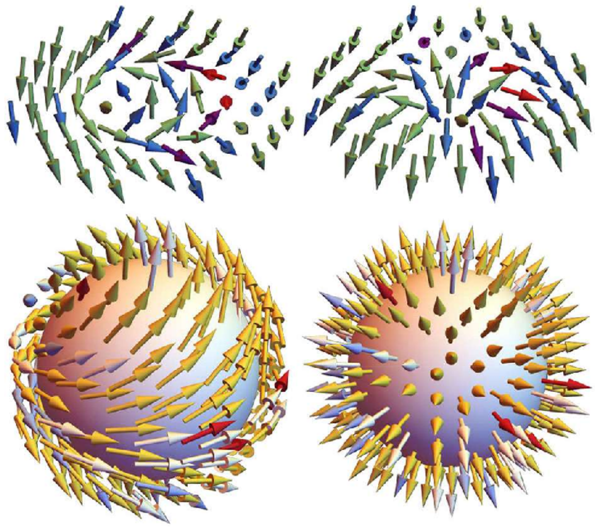

Figure 2.2: Bloch skyrmion (top left) and Néel skyrmion (top right) with topological charge $\Phi = 1$ and polarity $p = 1$. Bottom: a stereographic projection shows how spins wrap around the unit sphere in the case of a Bloch skyrmion (left) and a Neél skyrmion (right). Taken from [24].

interaction and magnetic anisotropy for example can give rise to a magnetic domain structure known as bubbles with integer topological charge, which led to commercially available bubble memories in the 1980s [26]. However, the comparatively large size of bubbles of around 1 μm inhibited further development. Other stabilization mechanisms include frustrated exchange interactions [25], higher order exchange interactions, especially four-spin interactions [27], and the RKKY interaction [28]. Most importantly, DMI stabilizes skyrmions in most known materials today and comes in two flavours: bulk DMI and interfacial DMI. The key ingredient for DMI is always a broken inversion symmetry.

2.3 Skyrmion Hosting Bulk Materials

One of the most prominent materials to host skyrmions are the cubic but non-centrosymmetric B20 compounds with the chiral space group $P2_13$. The first experimental evidence for magnetic skyrmions was found in MnSi [7]. Another early metal compound was FeGe [29], which hosts skyrmions close to room temperature. The only magnetoelectric insulator to host skyrmions known to this date is the multiferroic Cu_2OSeO_3 [30], with the same space group $P2_13$ as the B20-type skyrmion hosts. Recently, high temperature skyrmions have been found in B20 CoSi [31]. A whole zoo of skyrmion hosting compounds were found in the β-Mn-type structure CoZnMn with the chiral space group $P4_132$, including the compositions $Co_8Zn_8Mn_4$, $Co_8Zn_{10}Mn_2$ and $Co_9Zn_9Mn_2$, which host skyrmions at and above room temperature [32]. All of these materials mentioned above host Bloch-type skyrmions. Néel-type skyrmions were found in the multiferroic semimetal GaV_4S_8 with a polar rhombohedral structure [33] .

2.4 Skyrmion Hosting Multilayers

Apart from single crystal bulk systems, inversion symmetry can also be broken at interfaces of thin film ferromagnets and heavy metal bilayers, where strong spin-orbit coupling generates interfacial DMI [34]. These stacks typically host Néel-type skyrmions. Pt, Ta, Ir and W are among the most common heavy metal layers used for multilayered skyrmion systems. The ferromagnetic layers are often Co- or CoFeB-based due to their relatively high DMI [35]. The lower and upper interface of the ferromagnetic layer give rise to an effective DMI. Heavy metal layers at these two interfaces induce a DMI with opposite sign respectively, and therefore further increase the overall DMI strength. The DMI can be further tailored by the thickness of the ferromagnetic film: the thinner the film the higher the DMI. This way, multilayers can be engineered to host skyrmions of the size of only a few nanometers. There is a trade-off between skyrmion size and temperature stability. Stacks with thicker ferromagnetic layers and repeated multiple times have shown to host larger skyrmions in the range of 50 to 250 nm above room temperature [35]. The possibility to tune these parameters based on the choice and thickness of materials makes multilayer systems especially interesting for technological applications, such as racetrack memories [36].

2.5 Properties of Cu_2OSeO_3

The vast majority of experiments in this work have been performed on TEM lamellas of bulk Cu_2OSeO_3. We therefore give an overview of its main properties in the following.

Cu_2OSeO_3 has the same $P2_13$ space group as the B20 alloys FeGe and MnSi, the latter of which was the first material where magnetic skyrmions were discovered in a condensed matter systems [7]. The crystal structure is characterised by two inequivalent Cu^{2+} (spin $S = 1/2$) sites with different oxygen coordinations : either surrounded by a square pyramid (Cu1 sites) or by a trigonal bipyramid of O^{2-} ions (Cu2 sites) [37], as depicted in figure 2.3 A. These two types occur with a ratio of Cu1:Cu2 of 3:1 [30]. The magnetic ground state is found to be a three up one down ferrimagnetic spin configuration (see figure 2.3 B) below the transition temperature of $T \approx 60\,\mathrm{K}$. Cu_2OSeO_3 is an insulator with unique magnetoelectric properties making it an ideal candidate material for spintronic devices.

While the skyrmion phase occupies only a small pocket in the phase diagram of bulk Cu_2OSeO_3, it extends down to the lowest temperatures and across a much larger magnetic field range in its thin film form. Due to stray fields, a flux-closure state is energetically more favourable, which is the case for skyrmions compared to other magnetic textures. One of the key results in this thesis is that we establish a more complete version of the phase diagram depicted in figure 2.3 since we find that the skyrmion phase not only consists of the lattice phase, but also of a liquid and a semi-ordered so called hexatic phase.

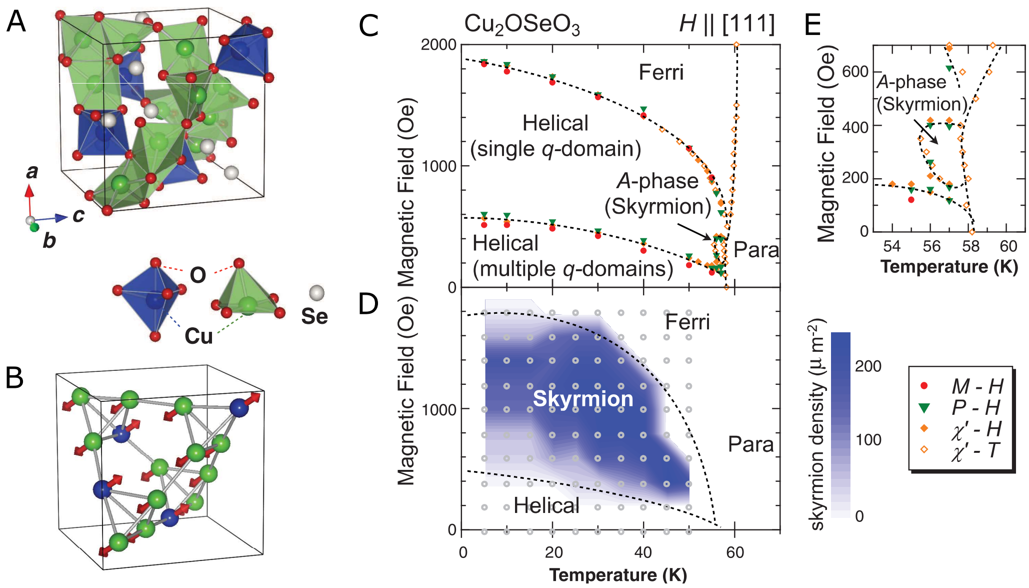

Figure 2.3: A: crystal structure of Cu_2OSeO_3 with two inequivalent Cu^{2+} sites with different oxygen coordination. B: Three up one down ferrimagnetic spin configuration. C: phase diagram for bulk Cu_2OSeO_3 crystal with magnetic field $H \parallel [111]$ as measured by magnetic field scans of magnetization, electric polarization and AC magnetic susceptibility. D: phase diagram for thin film Cu_2OSeO_3 measured by counting skyrmions via Lorentz TEM imaging. Adapted from [30].

2.6 Magnetoelectric Coupling

A magnetically induced electric polarization P in Cu_2OSeO_3 emerges in all of its magnetic phases: the ferrimagnetic, helimagnetic and skyrmion lattice phase [38], opening the avenue of manipulating magnetic textures by electric fields. Particularly the magnetoelectric control of skyrmions is highly interesting for technological applications. The polarization in Cu_2OSeO_3 emerges as a result of the modulation of the covalency between the metal d- and ligand p-orbitals as a function of the local magnetization via spin-orbit coupling, known as the d-p-hybridization mechanism [38]. Thus each skyrmion induces an electric dipole or quadrupole, making it in principle possible to control skyrmions individually using electric fields. The d-p-hybridization model predicts a local electric dipole along the bond direction $\boldsymbol{p}_{ij}$ of $\boldsymbol{p}_{ij} \propto (\boldsymbol{e}_{ij} \cdot (<\boldsymbol{m}_i>)^2 \boldsymbol{e}_{ij}$ with $\boldsymbol{e}_{ij}$ being a unit vector along the bond between sites i and j and $<\boldsymbol{m}_i>$ the magnetic moment of the Copper ion. For any spin texture $\boldsymbol{m}(\boldsymbol{r})$ the emerging polarization is given by [38]

$$\boldsymbol{P} \propto \frac{1}{\int d\boldsymbol{r}} \int \sum_{i,j} [\boldsymbol{e}_{ij} \cdot \boldsymbol{m}(\boldsymbol{r})]^2 \boldsymbol{e}_{ij} d\boldsymbol{r}, \tag{2.9}$$

with the sum carried out over 80 Cu-O bonds in a crystallographic unit cell and the integral over a magnetic unit cell. The magnetization $\boldsymbol{M}$ is given by [38]

$$\boldsymbol{M} \propto \int \boldsymbol{m}(\boldsymbol{r})d\boldsymbol{r} \Big/ \int d\boldsymbol{r}. \tag{2.10}$$

For a collinear spin state this means $P = 0$ for $M \parallel [001]$, $P \parallel [001]$ for $M \parallel [110]$ and $P \parallel [111]$ for $M \parallel [111]$. When we plug in the magnetization distribution of a skyrmion lattice into equation 2.9 for various magnetic field directions [38],

$$\boldsymbol{m}(\boldsymbol{r}) \propto \boldsymbol{e}_z M + \sum_{a=1}^{3} [\boldsymbol{e}_z \cos(\boldsymbol{q}_a \cdot \boldsymbol{r} + \pi) + \boldsymbol{e}_a \sin(\boldsymbol{q}_a \cdot \boldsymbol{r} + \pi)], \tag{2.11}$$

where $\boldsymbol{q}_a$ is the propagation vector of the helices perpendicular to the magnetic field H, $\boldsymbol{e}_a$ a unit vector perpendicular to $\boldsymbol{e}_z$ and $\boldsymbol{q}_a$, we obtain the local polarization distribution as shown in figure 2.4 as well as the local electric charge via the relation $\rho(\boldsymbol{r}) \propto \nabla \cdot \boldsymbol{p}(\boldsymbol{r})$.

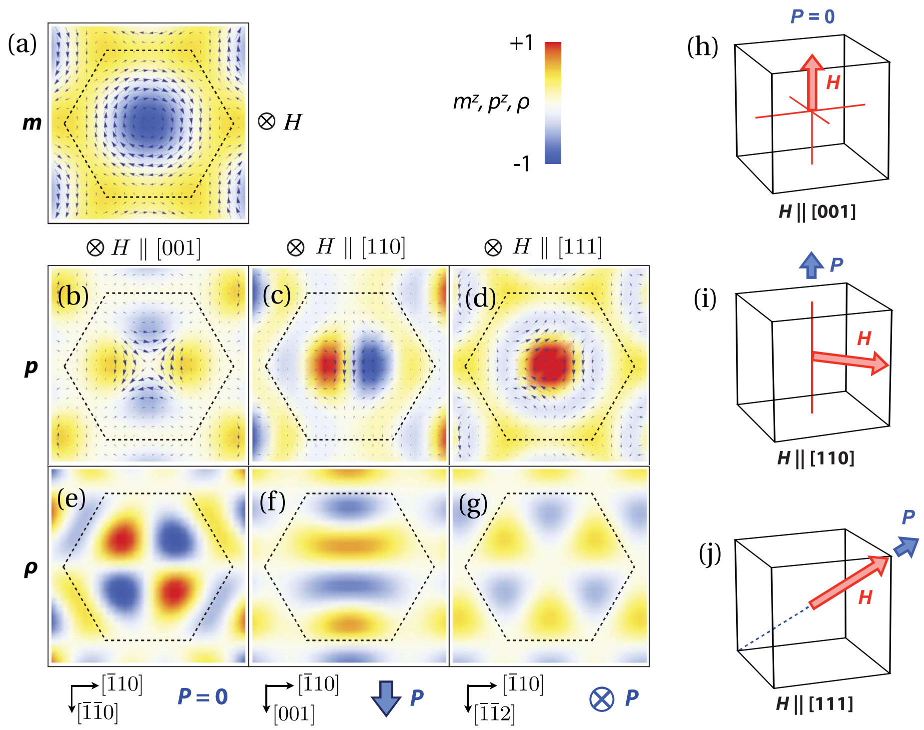

Figure 2.4: Spatial distribution of the local magnetization (a), and local electric polarization p according to equation 2.9 for different magnetic field directions (b-d). Local electric charge ρ based on the respective polarization (e-g). Overview of direction of induced polarization P as a function of the direction of the magnetic field H (h-j). Adapted from [38].

From figure 2.4 we can deduce that each skyrmion locally induces an electric quadrupole moment for $H \parallel [001]$ and an electric dipole moment for $H \parallel [110]$ (along [001]) and $H \parallel [111]$

(along [111]).

It has been shown experimentally using small angle neutron scattering (SANS) and theoretically that the emerging polarization can be used to tune the magnetic phase diagram of Cu_2OSeO_3 when applying external electric fields [39], as presented in figure 2.5.

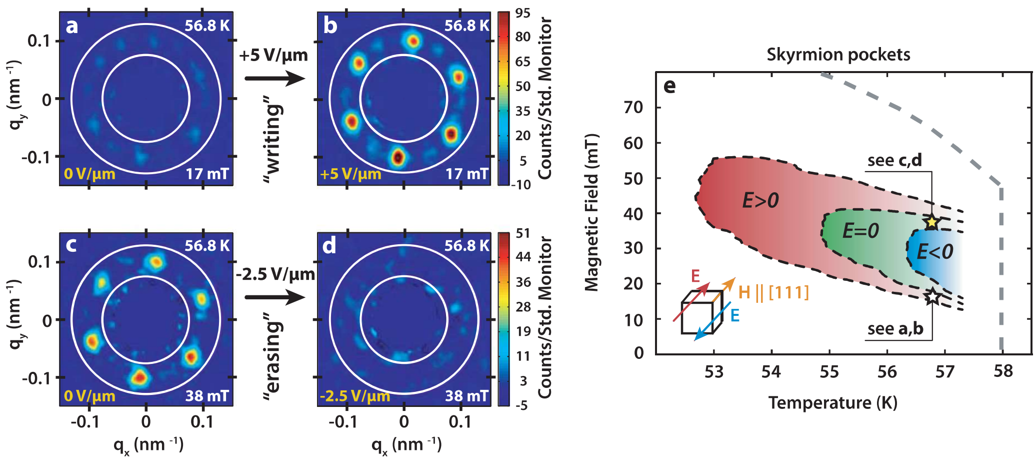

Figure 2.5: Panels a-d are the SANS patterns at different electric biases at the indicated temperature and for $E \parallel H \parallel [111]$. Panel e shows the change of the size of the skyrmion phase upon application of an external electric bias. Adapted from [39].

Skyrmions can be created from a conical state close to the equilibrium skyrmion phase when applying a positive bias and can be erased upon application of a negative bias. The neutron scattering experiments have been performed for various electric biases while scanning the magnetic field and temperature in the $H \parallel E \parallel [111]$ geometry. The scattered intensity was evaluated to yield the bias-dependent phase diagram. In fact, the polarization appears as an additional term in the free energy and therefore can be used as a handle to change the energy landscape depending on the applied electric field which it couples to. This opens a whole new field of external skyrmion control and low dissipation skyrmionic devices. A first successful step in that direction was performed with the LTEM experiments by Huang et al. [40] on thin slabs of Cu_2OSeO_3, where the [110] geometry has been chosen to repeatedly switch between helical and skyrmion states. A main goal of the present thesis is to explore the more challenging but technologically more viable [111] geometry, since it allows in principle to locally address skyrmions.

2.7 Experimental Techniques

In the following we will give a short overview of the main experimental techniques used for this thesis. They include sample fabrication in the clean room using photolithography, sample preparation using the focused ion beam (FIB) microscope and the experimental observation carried out using the transmission electron microscope (TEM).

2.7.1 Photolithography

We prepare small TEM substrates with electrodes produced by clean room microfabrication techniques to place samples on them for in-situ TEM biasing experiments. We use commercially available 'Silson' p-doped silicon chips with a 50 nm thick silicon nitride membrane. They are shipped as an array of 3×3 individual 2 mm wide squares each with one 100 μm wide square hole in its center (covered by 50 nm of SiN) embedded in a square frame 1 cm wide. All chips are 100 μm thick and the individual small chips can be manually broken out at pre-etched notches. The lift-off technique is adopted for the deposition of the electrodes. The process is illustrated in figure 2.6.

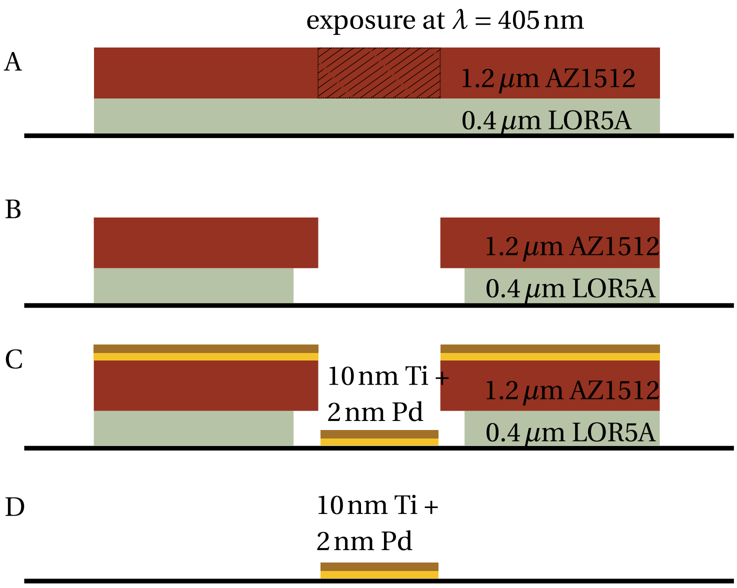

Figure 2.6: Schematic of the photolithographic lift-off process.

A bilayer of a soluble sacrificial layer (LOR5A) and positive photoresist (AZ1512) is spincoated on the chip. The coating is performed on one of CMi's manual coaters, the ATMsse OPTIspin SB20. The surface of the chip must be first dehydrated (10 min. at 135 °C) to improve resist adhesion. The chip is glued using quickstick to a dummy wafer, vacuum clamped on the rotation disc on the coater and a droplet of LOR5A resist is dispensed on the chip. A rotation speed of 4000 rpm leads to a final thickness of 0.4 μm. After a softbake at 100 °C, a second droplet of the AZ1512 resist is dispensed on the chip. A rotation speed of 5000 rpm leads to a final thickness of 1.2 μm.

The solubility of AZ1512 is changed when exposed to UV light. This process is done using a maskless laser writer (MLA150). It exposes the desired pattern on the photoresist. When put into a solvent (MIF716), the exposed AZ1512 is dissolved and frees the underlying layer of LOR5A. Since it is soluble in any solvent, it dissolves further in, creating an underetch. Now the metal, in our case a bilayer of Ti-Pd is evaporated in a dedicated electron beam evaporator that deposits the material straight down. Then the actual lift off happens when the chip is immersed in a solvent (remover 1165) for a sufficiently long time (usually overnight). It dissolves the photoresist, but especially the sacrificial layer and with it 'lifts off' the metal deposited on top so that only the desired structure remains.

2.7.2 Focused Ion Beam

The majority of sample preparation in this thesis is carried out using the focused ion beam (FIB). It is a precision micromachining tool that generates a sharp beam of ions that locally mills away material. It usually comes as a dual column design, essentially upgrading a conventional scanning electron microscope (SEM). Observations can therefore be performed live either in SEM mode or FIB mode. The typical FIB configuration is shown in figure 2.7. It

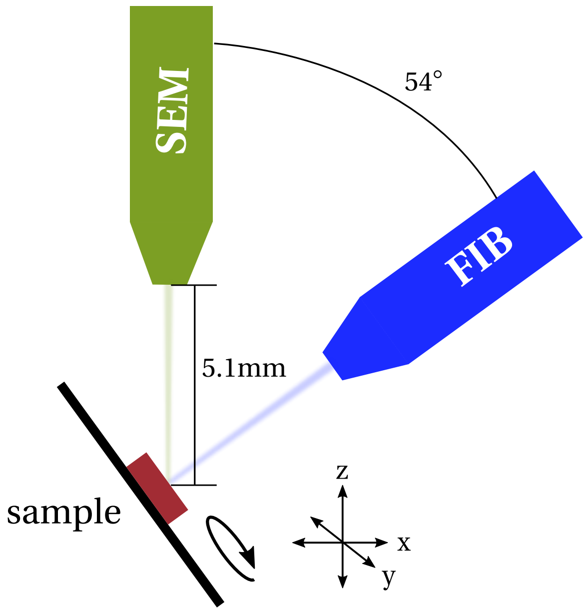

Figure 2.7: Basic setup of a FIB: vertical SEM column with FIB column at an angle of 54° in the case of a Zeiss NVision40. The point of coincidence of the electron and ion beam is at 5.1 mm working distance.

consists of a vertically mounted electron column and an ion column at an angle, in the case of the Zeiss NVision40 used in this work it is 54°. The sample is mounted on a stage that can be moved in all three directions x, y, z and be rotated around its normal direction. This allows to access a sample from wide range of directions. The default operation mode is in coincidence, i.e. that sample is brought to the default height of 5.1 mm in the case of the NVision, which is where the electron an ion beam cross each other and therefore the region of interest on the sample can both be observed in SEM and FIB mode.

The basic setup of an ion column is similar to that of a SEM. It consists of an ion source, electromagnetic and electrostatic lenses and apertures to guide and form the beam of ions. Most commonly FIBs feature a liquid metal ion source (LIMS) which due to its low melting temperature is often chosen to be gallium. Strong electric fields shape the liquid into a sharp tip, the exact shape of which is given by the strength of the field and the surface tension. As in solid sources (e.g. LaB_6 crystals in electron microscopes) the ions are emitted from the sharpest point of the tip where electric fields are highest and which therefore acts as a point ion source.

The interactions between matter and electrons and ions are depicted in figures 2.8 and 2.9. When electrons impinge on the surface, multiple signals can be detected, the most important of which are secondary electrons, back scattered electrons and X-rays. Secondary electrons are generated when primary electrons ionize atoms. These electrons have the lowest energy of all electrons leaving the sample and only those coming from close to the surface are detected. Therefore they provide information about the sample topography. The Everhart-Thornley detector is most commonly used for the detection of secondary electrons. It is composed of a positively charged Faraday cage to attract the electrons. A scintillator within that cage converts them to light which a photomultiplier then amplifies. The detector is typically mounted at an angle on the side of the FIB chamber for highest detection efficiency. Figure 2.8 shows how the collision cascade of incident ions creates secondary electrons close to the surface as well, so that the same detector can be used both for ions and electrons.

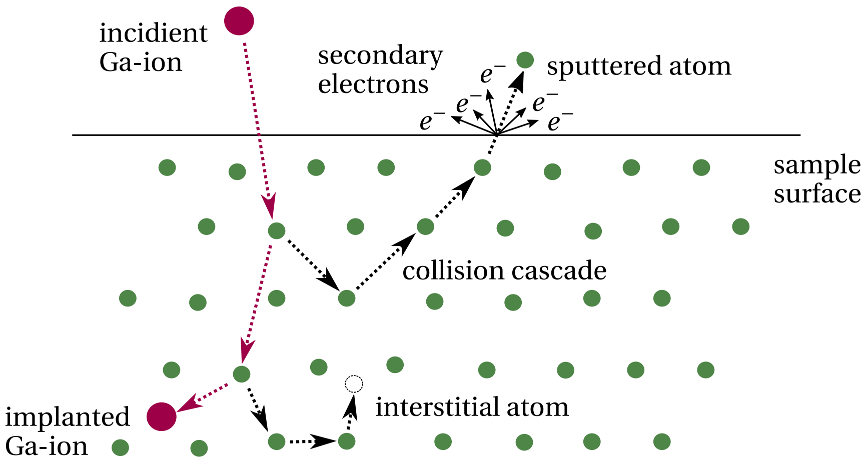

Figure 2.8: Collision cascade of incoming gallium ions. After colliding with atoms they can be implanted into the sample, atoms can be knocked into different positions and agitated atoms close to the surface can emit secondary electrons.

Backscattered electrons (BSE) come from deeper within the interaction volume and are scattered off atoms. The scattering cross section increases with atomic number and hence backscattered electrons can provide information about the atomic composition of a sample. BSE detectors are usually solid state detectors based on p-n-junctions. The created electron-hole pairs generate a current proportional to the incoming electrons. The detector is annular and mounted at the bottom of the objective lens with the electrons passing through the center.

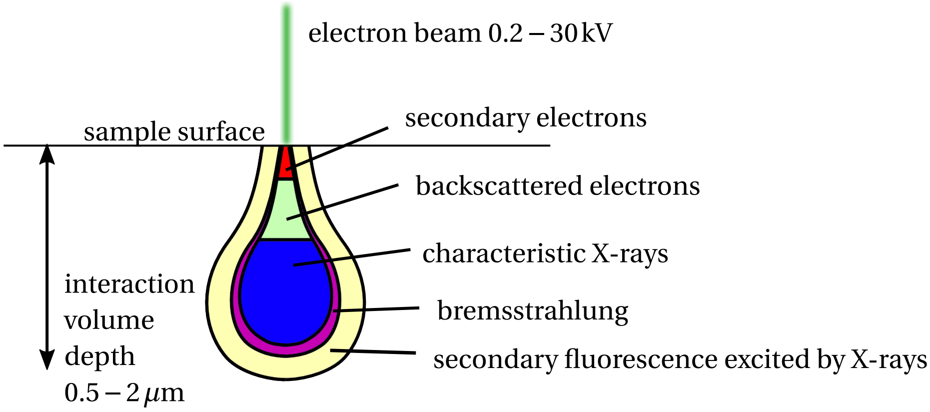

Figure 2.9: Drop-shaped interaction volume of electrons with matter. Secondary electrons are emitted from close to the surface and a small cross section leading to a high resolution signal. Backscattered electrons come from within deeper in the sample and provide less good resolution but compositional information. X-rays and fluorescence are generated deep within the interaction volume.

Finally, FIBs are often equipped with X-ray detectors for element specific analysis.

Both electrons and ions can be used for imaging. However, while most non-organic samples do not suffer from any electron beam damage, due to its much higher mass ions always damage and ablate the sample even at low acceleration voltages. There is also significant Ga-ion implantation in the surface layer, as illustrated in figure 2.8. While the gradual ablation of material can be used for imaging purposes (e.g. 3D tomography [41]) our main focus in this work is to use the milling capabilities for precise fabrication of high quality TEM samples. In this context it is important to understand the implications of the interaction volume of Ga-ions as a function of their acceleration voltage, as illustrated in figure 2.10. At the default

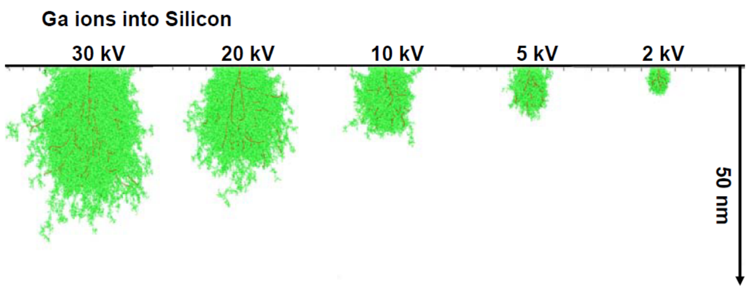

Figure 2.10: Interaction volume of Ga ions of different energy in silicon. Taken from [42].

milling voltage of 30 kV the damage and Ga-implantation layer reaches up to 30 – 40 nm below the sample surface. Especially for thin TEM samples with a thickness in the range of 100 nm and milling from both sides, this may mean that barely any crystalline material is left for observation. Lower voltages lead to much thinner damage layers and should always be considered to reduce the thickness of the original damage layer and Ga-ion implantation.

Ion-Assisted Gas Deposition

The FIB can not only be used for top down micromachining but also for bottom up microfabrication by locally depositing materials through ion- or electron beam induced gas deposition. Precursor gases are injected into the chamber close to the sample surface via a retractable gas nozzle and cracked up under irradiation of electrons or ions. Depending on the gas, this leads to the deposition of the desired material, e.g. carbon or platinum (in the case of the NVision40 at EPFL). Phenanthrene ($C_{14}H_{10}$) is used as a precursor for C deposition and trimethlplatinum ($(CH_3C_5H_4)(CH_3)_3Pt$) for platinum deposition [43]. Electron-beam-induced deposition (EBID) is slow and typically leads to more resistive deposits compared to ion-beam induced deposition (IBID) [43]. As a function of the size of the deposition area, the ion beam current needs to be chosen appropriately so as to both induce sufficient deposition but reduce the ablation of the deposited material at the same time.

2.7.3 Sample Handling Using Micromanipulators

Two Kleindieck micromanipulators are available on the NVision at EPFL, one mounted to the chamber roof and the other to the chamber door, allowing to access a sample from different directions as illustrated in figure 2.11.

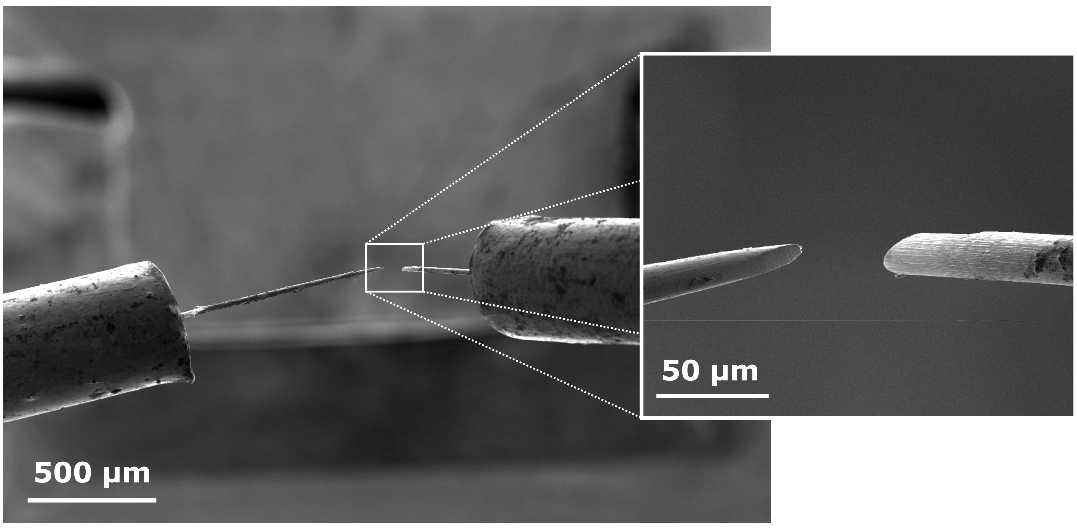

Figure 2.11: Both micromanipulators in CIME's NVision40 deployed for use.

Their tungsten tip can be sharpened directly in the FIB and typically samples are attached to either of the micromanipulators with a bit of carbon. They can be inserted/retracted and veered around two axes. Control is performed by stepper motors for rough adjustment and Piezo motors for fine adjustment. Both manipulators are equipped with BNC plugs and can be used for current measurements.

2.7.4 TEM Sample Preparation

After aligning, cutting, and mirror polishing the crystal, it is recommended to coat insulating samples such as Cu_2OSeO_3 with a few nm of carbon or gold, to avoid charging when imaging in SEM mode. The crystal, ready for processing in the FIB, is shown in figure 2.12. The first step is to deposit a carbon capping layer with the rough dimensions of the future lamella (see figure 2.13). The purpose is twofold: on the one hand it protects the top part of the sample from Ga-implantation and on the other hand it helps to mill a straight and smooth surface from both sides. The sputter yield is highest for an angle of around 75° and almost zero at grazing incidence, referring to how much material is ablated. Therefore the top part of a sample will adopt a dome-like shape. However we would ideally like to have a homogeneously thick lamella, which is why the carbon capping layer is used. Next, trenches about 20 μm deep are milled on three sides of the lamella choosing the highest current available (27 nA or 45 nA on the NVision), see figure 2.13. The current is reduced to about 3 nA when the lamella is 2 μm thick which is when it is ready for lift out and to be transferred on a TEM Omniprobe grid (typically made of copper, sometimes molybdenum, which is stiffer and more suitable for some applications).

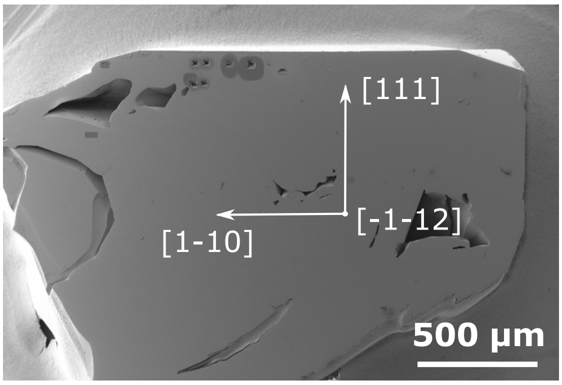

Figure 2.12: Oriented, cut and polished crystal of Cu_2OSeO_3 ready for FIB.

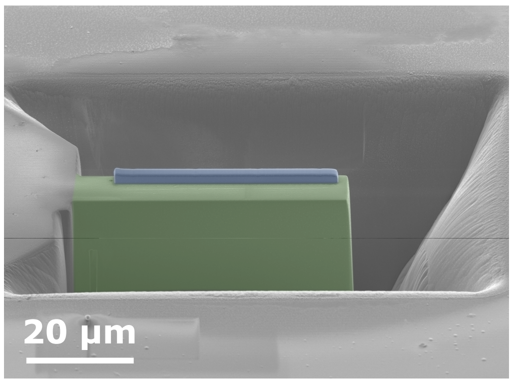

Figure 2.13: Pre-thinned and undercut lamella ready for lift-out.

The lamella is undercut at 9° and cut on the left so that it is only attached to the rest of the crystal by a small bar. Note that the undercut (usually performed at a beam current of 3 nA) can produce a conductive path at the bottom edge of the sample and should be removed if necessary. In a next step, the micromanipulator is brought in and glued to the lamella by some carbon deposition, see figure 2.14. Then the connection to the crystal is cut and the lamella can be freely moved to the Omniprobe TEM grid to be attached there, see figure 2.15.

This is where the final thinning is performed. In this work we are interested in large fields of views to image a large amount of skyrmions. When thinning large areas down to a few

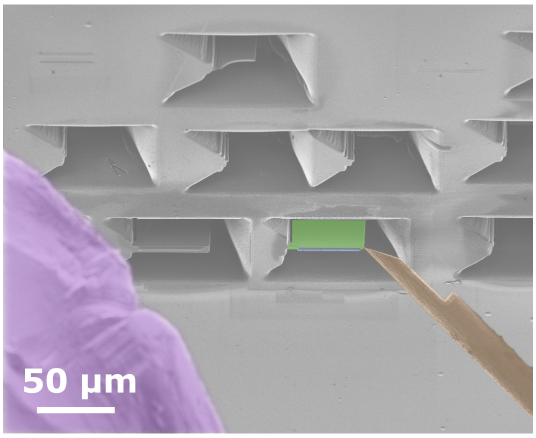

Figure 2.14: Lift-out of lamella with manipulator.

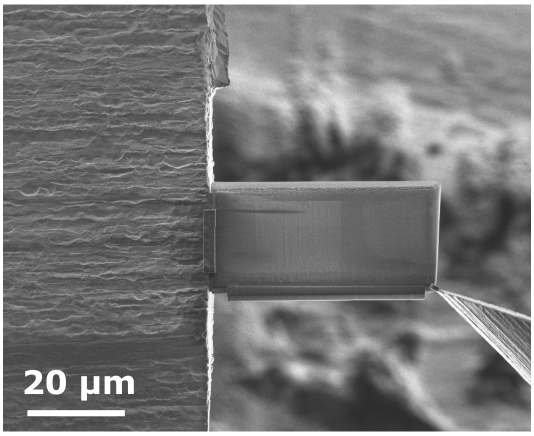

Figure 2.15: Transfer of the lamella to an Omniprobe sample grid.

hundred nanometers, they often tend to curl up (stress by Ga-implantation plus heat). To prevent this, most lamellas in this work retain a U-shaped frame to provide sufficient stability for the thin area with the added benefit of having enough rigidity for lamella transfers to other substrates if necessary, see figure 2.16.

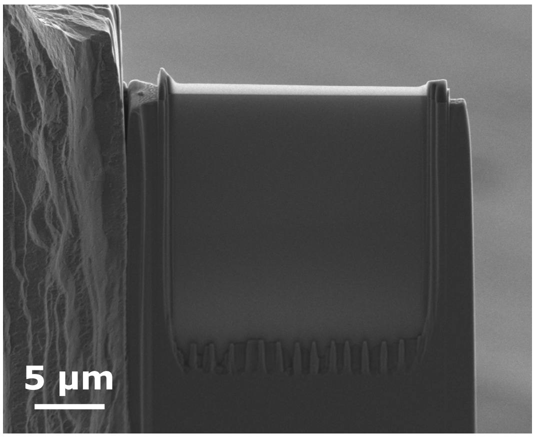

Figure 2.16: U-shaped lamella. Onset of brightness indicates final thinning stage.

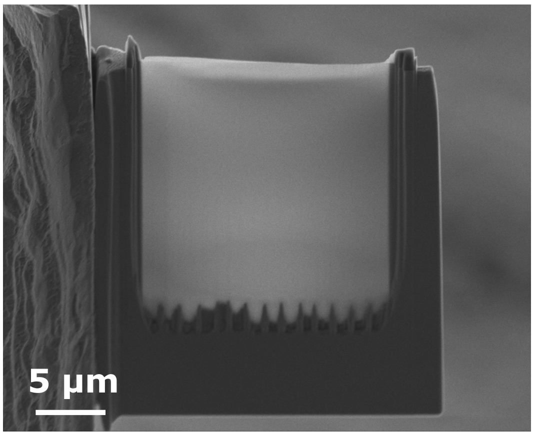

Figure 2.17: Final lamella.

From experience, lamellas of Cu_2OSeO_3 appear bright in SEM for secondary electrons at 5 kV (default) acceleration voltage when they reach around 150 nm in thickness. The increase in brightness comes about when the film becomes so thin that electrons from both sides of the surface reach the detector. In order to perform adjustments in the fibbing angle early enough to produce a homogeneously thick lamella, one can increase the electron voltage e.g. to 10 kV and gradually go down in voltage as the sample is thinned down. At 5 kV at the onset of increasing brightness, we recommend to switch the ion beam acceleration voltage from 30 kV down to 5 kV and carry out the final thinning at this voltage. This way, as illustrated in figure 2.7, the interaction volume of Ga-ions is drastically reduced and the final result will both have less conductive Ga-implantation (important to maintain the insulating properties of Cu_2OSeO_3) as well as only a very thin damage layer. The final result is shown in figure 2.17.

2.7.5 Lorentz Transmission Electron Microscopy

After the initial studies on skyrmion hosting materials have been performed using neutron scattering [7, 44, 45], moving towards real space imaging techniques soon opened a wide avenue for new discoveries [46, 47, 29, 48]. Among these, Lorentz transmission electron microscopy (LTEM) turns out to be one of the most versatile tools available for the study of magnetic phenomena since it allows for high resolution in-situ experiments and observations in real time. The accessible time scales depend on the flavour of LTEM, ranging from a few tens of milliseconds for a standard setup with a Ceta CMOS camera as used on the Titan Themis in CIME down to a few picoseconds for ultrafast LTEM [49].

A simplified scheme of a Lorentz transmission microscope is depicted in figure 2.18. Modern

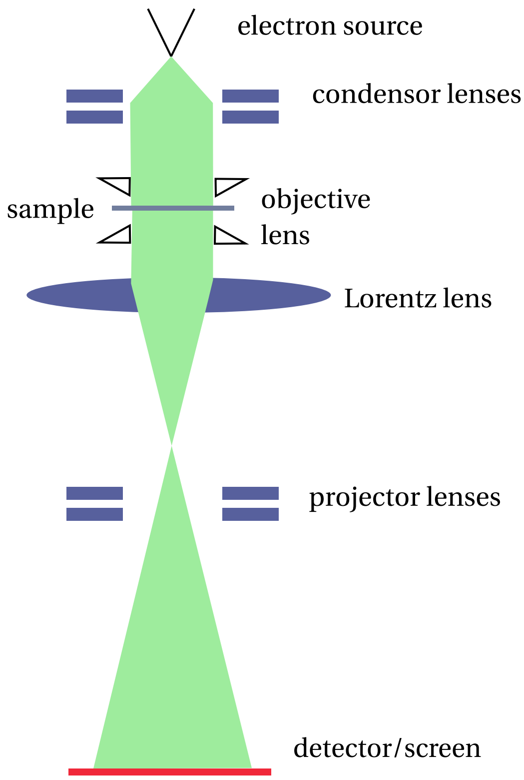

Figure 2.18: Simplified schematic of a Lorentz TEM. The key difference to a standard TEM is the additional Lorentz objective mini lens.

TEM feature a field-emission electron gun as an electron source. Electrons are emitted from a sharp tip upon application of a high electric field. A set of condenser lenses brings the electrons on the sample either as a convergent or parallel beam. Projector lenses guide the

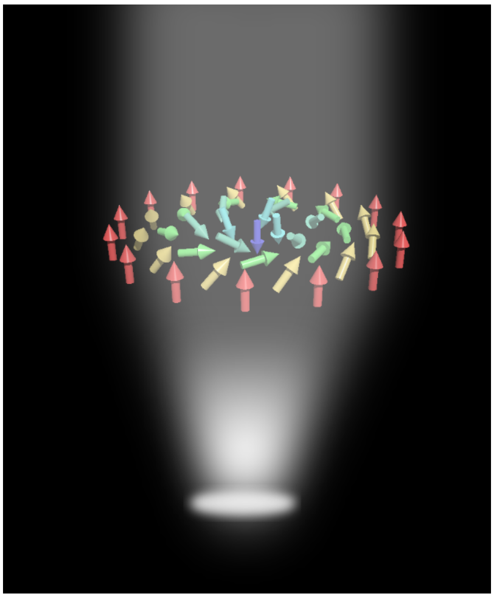

(a) Right-handed skyrmion.

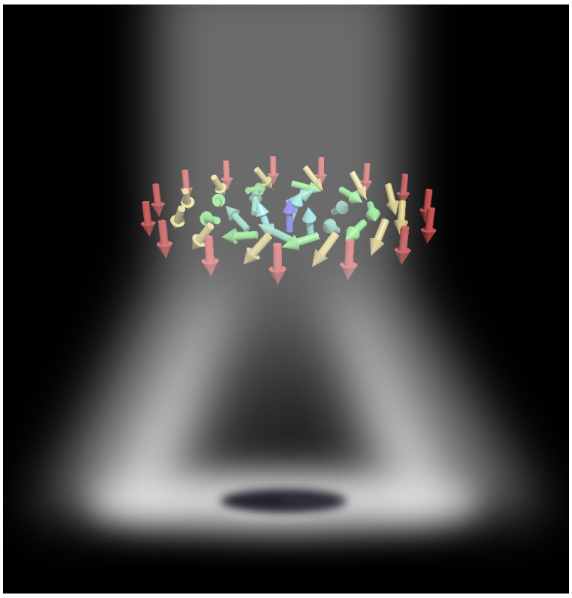

(b) Left-handed skyrmion

Figure 2.19: LTEM in overfocus. A right-handed skyrmion (a) produces a white dot on the screen while a left-handed skyrmion produces a black dot (b) due to the electrons (white beam) being deflected by the Lorentz force. Note that in reality the electron beam is much larger than the size of a skyrmion.

transmitted beam to the detector. The key difference to a standard TEM setup is an additional dedicated objective lens, the so called Lorentz mini lens, that is placed below the actual objective lens and is used to produce the image. In this configuration the objective lens is switched off to provide a magnetic-field free environment since it typically generates around 2 T of magnetic field and would completely saturate most magnetic samples. It can however be used to apply any desired magnetic field perpendicular to the sample between zero and the maximum excitation by tuning the current in the lens. To see the magnetic contrast which is generated by the Lorentz deflection at the in-plane components of a magnetic sample, a defocus of typically a few hundred microns is used (Fresnel imaging mode)[1]. When there are in plane magnetic components present in a sample, the incident electrons will be deflected according to the Lorentz force:

$$\mathbf{F} = q(\mathbf{E} + \mathbf{v} \times \mathbf{B}), \tag{2.12}$$

where q is the charge, **E** is the electric field and **B** is the magnetic field. This deflection manifests itself as a magnetic contrast on the detector on top of the other contrast generating mechanisms in TEM bright field imaging. However, this deflection can only be seen when defocussing the image, as can be understood from figure 2.19. We see how the electrons are

[1] This passage is copied mostly verbatim from the author's published work [50]

deflected at the in-plane magnetization such that for a right-handed skyrmion a white dot appears at a defocus, while a black dot appears for a left-handed skyrmion. Similarly, the contrast is reversed when either a positive or negative magnetic field is applied. This is why in some images presented in this thesis skyrmions appear as white dots, while in others they appear as black dots.

While the information limit for CIME's Titan is $\leq 0.7\,\text{Å}$, the spatial resolution in Lorentz mode is much lower due to the higher aberrations of the Lorentz mini lens and most importantly due to the defocus values to observe magnetic contrast (up 1 mm to image skyrmions in Cu_2OSeO_3). This leads to a spatial resolution limit of LTEM of typically 5 nm – 10 nm [51].

3 Electric field biasing

One of the most coveted applications of skyrmions are their use in low power electronic devices and storage media. Here we report the electric creation and annihilation of skyrmions in the magnetoelectric skyrmion host Cu_2OSeO_3 using electric fields in a geometry that is most suitable for technological applications. We perform our observations in-situ using Lorentz transmission electron microscopy. We successfully and repeatedly create and erase skyrmions at the phase boundary between the skyrmion and helical phase and provide new insights into the switching procedure by looking at write and erase times and hysteresis loops. Moreover, we make first attempts to control skyrmions locally using electric fields. Our experiments further pave the way for using skyrmions in low dissipation electronic devices.

3.1 Electric Field Biasing on Cu_2OSeO_3

In terms of using skyrmions for magnetic storage applications much effort has been invested into the race-track concept, where skyrmions are moved along a wire by an electric current under a read and write head [19, 52]. While this concept was originally developed for magnetic domain walls [53], skyrmions can be moved by much lower current densities. In this thesis we want to explore a different paradigm to exploit the magnetoelectric coupling in Cu_2OSeO_3 in favour of an all-electric creation, detection and annihilation of skyrmions. Since no electric currents need to flow, this approach is in principle dissipation free and opens an avenue for future ultra-low power electric devices. LQM has pioneered electric field investigations on Cu_2OSeO_3 through various bulk measurement techniques, in particular magnetoelectric susceptibility measurements [54], small angle neutron scattering (SANS) [55, 39] and Lorentz transmission electron microscopy [40]. We build up on these efforts to make the first steps towards the development of a new type of addressable and all-electric skyrmion-based memory. As discussed in chapter two, skyrmions can be induced from a helical background by an electric field in various crystallographic directions in Cu_2OSeO_3, notably when both magnetic field and electric field are oriented along the [111]-direction.

3.2 Sample Preparation and Experimental Procedure

The entire device fabrication procedure must be in line with the requirements of in-situ Lorentz transmission electron microscopy at cryogenic temperatures. This includes the dimensions of the device which are restricted by the available sample holder and the fact that the device needs to be electron-transparent as a whole for at least 300 kV. In order to study the electric field biasing effect, we sandwich a TEM lamella between two electrodes in the [111]-geometry. This geometry was not used in the previous LTEM study [40] since it proved to be too tricky to have the electrons to pass through a thick stack of lamella and electrodes. Yet this is the configuration which is of most interest for potential applications since it allows in principle to control skyrmions locally.

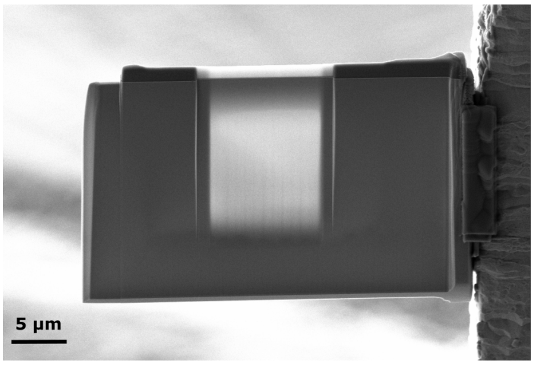

Figure 3.1: Preparation of U-shape lamella. Almost flat on one side, profile (gap) on other side.

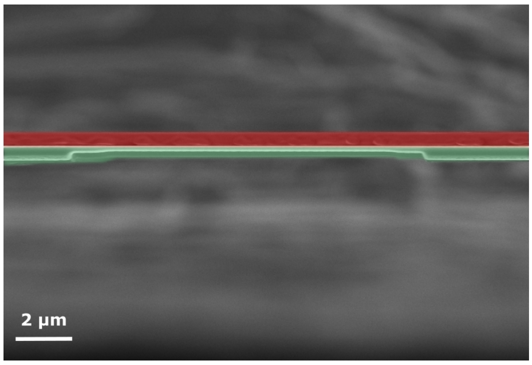

Figure 3.2: Flat front of lamella (green), and bottom part of U-shape on back side (red) creating gap.

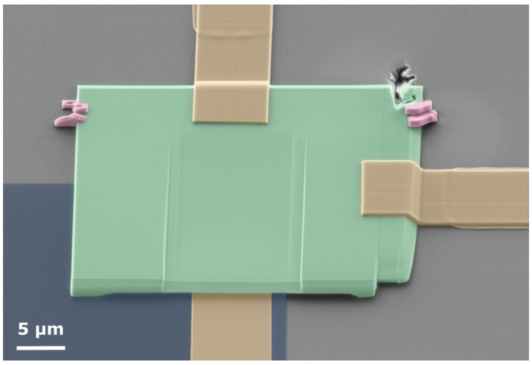

Figure 3.3: Ready device after transfer and electric connection. Lamella (green), electric connections (gold), carbon connections (pink).

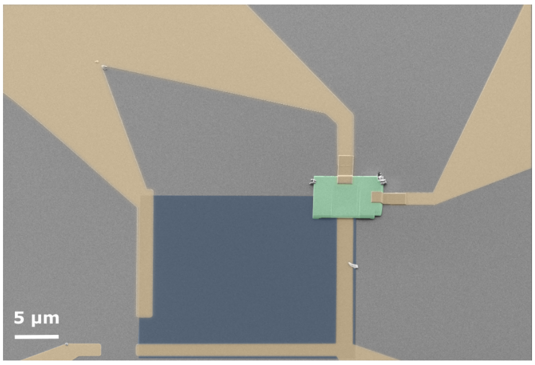

Figure 3.4: Ready device, electric connections (gold), lamella (green), SiN window (blue).

To prepare the TEM lamellas, we follow the procedure outlined in chapter two to provide the lamella depicted in figure 3.1. We prepare electrodes on commercially available SiN chips manufactured by Silson. Each chip is square, 100 μm thick, 2 mm wide, has a 50 nm thick

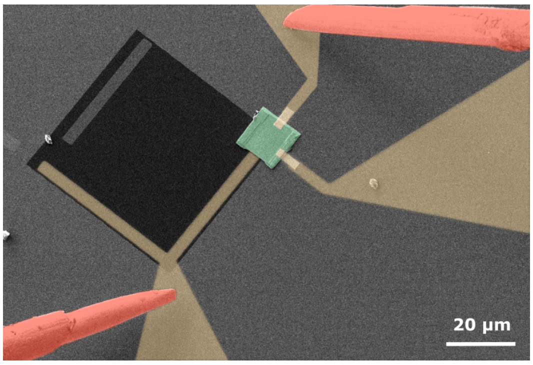

Figure 3.5: Testing leakage current of device using micromanipulators (red).

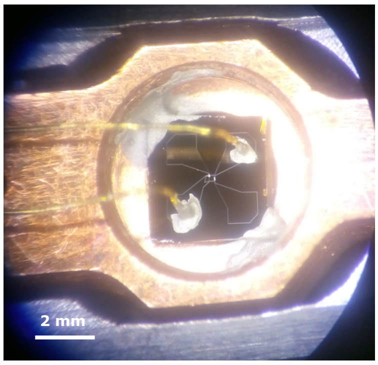

Figure 3.6: Device electrically connected to the biasing cryo-holder.

nitrite window for TEM use, and is embedded in a 9x9 pre-diced array on a 1 cm wide chip. The contacts are deposited using the lift-off technique as described in chapter two. The metal contact is a bilayer of 10 nm of Ti and 2 nm of Pd, the latter of which is used as a capping layer and to stop oxidisation of the Ti film. Ti was used for its properties in thin film deposition since it forms rather smooth films with small grains. Most importantly, its low atomic number makes it less absorbing for passing through electrons. At the same time when depositing on the SiN membranes we deposit the same bilayer on one side of the TEM lamella such that it acts as the top electrode while the bilayer on the membrane acts as the bottom electrode. This is illustrated in figure 3.2 where the green shading indicates the side of the lamella on which the metals are deposited.

Prior to the deposition, the TEM lamella undergoes a final cleaning procedure in the FIB at low voltage removing most of the amorphous layer and gallium implantation that could increase leakage current once a bias is applied to the device. In a final step, the lamella is cleaned in an oxygen plasma to remove other organic contaminants.

Then the lamella is transferred onto the chip and on top of the bottom electrode on the nitride window using the micromanipulators in the FIB. The connections from the top electrode on the lamella to the contact leads on the chip are made using ion beam deposited Pt in the FIB, see figure 3.3 and figure 3.4. To test the quality of the contacts and to make sure we actually apply an electric field across the sample, we use the two micromanipulators in the FIB for current measurements, see figure 3.5.

The device is finally mounted and electrically connected to a helium cryo-TEM holder, see figure 3.6. Using cryo-LTEM we can observe stable skyrmion lattice configurations after field cooling below 40 K. We acquire movies from a few seconds to a few minutes at different points in the magnetic field versus temperature phase diagram both while dynamically changing the magnetic field and electric bias.

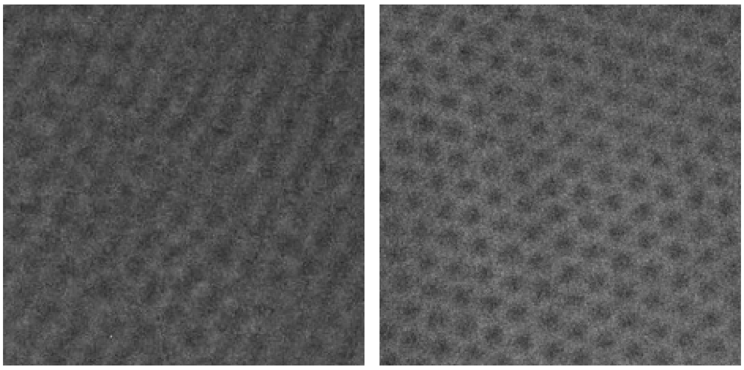

(a) Helical background (b) Mostly skyrmions

Figure 3.7: Example of grainy image in the device (a) versus clean image from a bare lamella only (b).

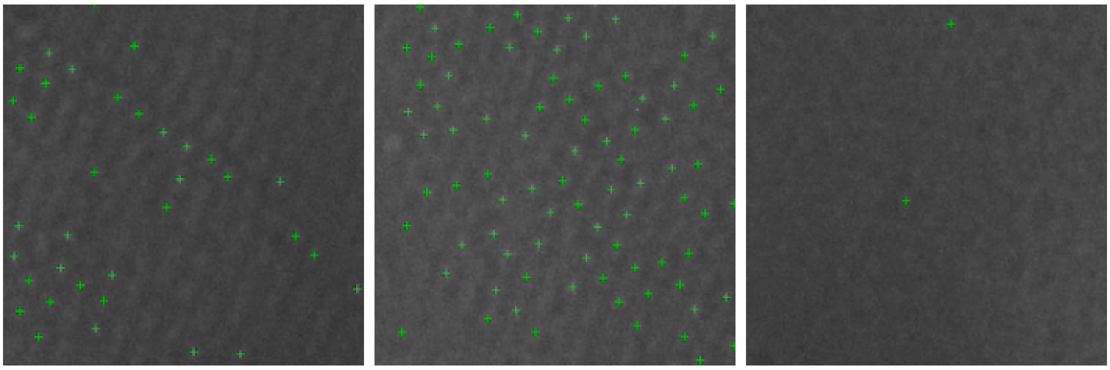

(a) Helical background (b) Mostly skyrmions (c) Bad contrast

Figure 3.8: Example of skyrmion identification in different phases: from skyrmions embedded in a helical background (a), to mostly skyrmions (b) and an intermediate phase between helices and skyrmions with bad contrast (c).

3.3 Skyrmion Identification Routine

Our goal is twofold: to prove that our device works in this new geometry and to extract quantitative information about the generation and annihilation of skyrmions. The latter is more challenging than in the previously studied geometry since the electrons need to pass through a stack of layers: the lamella itself but also the SiN membrane as well as most critically the two electrodes. Both the substrate and electrodes are not perfectly smooth and are naturally grainy. This becomes problematic in Lorentz mode when we use a large defocus to see the magnetic contrast since at the same time this blows up the grains in the electrodes and substrate in size. It just so happens that the optimal defocus of close to 1 mm brings these grains to a size comparable to skyrmions in Cu_2OSeO_3, which makes their identification somewhat more challenging and error-prone. This is illustrated in figure 3.7 (a) where we see some grainy contrast in our device that could perhaps be identified as skyrmions and for comparison skyrmions in a bare TEM lamella in figure 3.7 (b), which appear very crisp and can very easily be identified as such. To solve this problem, we develop an identification method specifically for the purpose of identifying skyrmions in a helical background and noisy environment. An example of identified skyrmions can be found in figure 3.8. In figure 3.8 (a) we identify a few skyrmions in a helical background, in figure 3.8 (b) we have mostly skyrmions, in figure 3.8 (c) we are in a phase between helical and skyrmion phase with particularly bad contrast and hence correctly identify almost no skyrmions. The details of the identification method can be found in the appendix. Note that the resulting number of extracted skyrmions is affected both by a systematic and statistical error. In constant imaging conditions we observe a constant offset of the skyrmion number with respect to the real number (e.g. we obtain a certain skyrmion count within the helical phase).

3.4 Magnetic Field Ramping at Different Electric Fields

To move towards an addressable skyrmion memory based on Cu_2OSeO_3, the electric field needs to be applied in the same direction as the magnetic field, hence we choose the [111]-direction for the lamella. We can directly observe the effect by scanning through the magnetic field range at constant electric biases (-10 V, 0 V, +10 V) while acquiring an LTEM movie, see figure 3.9, where the respective skyrmion count is displayed for a series acquired at 23 K.. The data in figure 3.9 (a) shows the case when the magnetic field is ramped starting at negative magnetic fields deep in the skyrmion phase at the transition to the paramagnetic phase, through the skyrmion phase and then through the helical phase around zero field. The magnetic field switches its sign to become positive and the field is ramped further to enter the skyrmion phase again. The blue data points trace the zero bias case, while the red ones are for positive bias (10 V) and green ones for negative bias (-10 V). The protocol to achieve this data is first to zero-field cool the sample to the target temperature (e.g. 23 K), ramp the field well into the skyrmion phase (negative sign), ramp the field up to the same field value only with the opposite sign (again in the skyrmion phase) and ramp the field down again to the starting field in the skyrmion phase. This procedure is repeated three times, for zero electric bias, +10 V and -10 V. Each field ramp in the positive direction yields a curve in figure 3.9 (a) and each field ramp in the negative directions yields a curve in figure 3.9 (b).

For all curves we clearly see a peak in the skyrmion count when going through the skyrmion phase between about -800 Oe and -300 Oe before it rapidly decreases upon entering the helical phase and finally goes up again when entering the skyrmion phase again at around 400 Oe. The well of the helical phase with low skyrmion count is widest for positive bias and most narrow for negative bias, in line with previous observations that a negative bias extends the size of the skyrmion pocket (and shrinks the size of the helical phase) while the opposite is true for positive bias [40]. A qualitatively similar behaviour can be observed in the case when the magnetic field is ramped down, see figure 3.9 (b). Hysteresis is considerable and the boundary of the skyrmion phase changes by up to 600 Oe as a function of the ramping direction, as can be seen in figures 3.9 (c) and (d) where we compare the skyrmion count

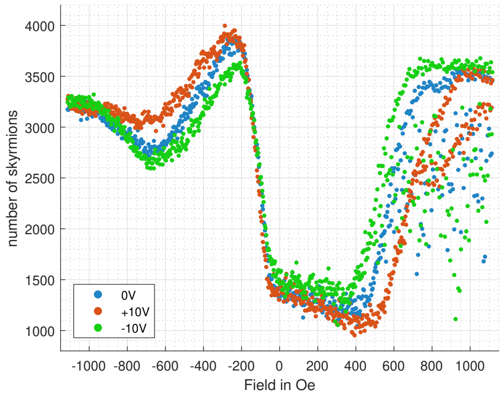

(a) Skyrmion count for ramping the magnetic field up at different biases.

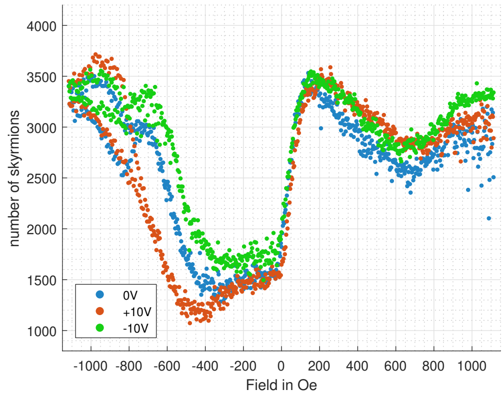

(b) Skyrmion count for ramping the magnetic field down at different biases.

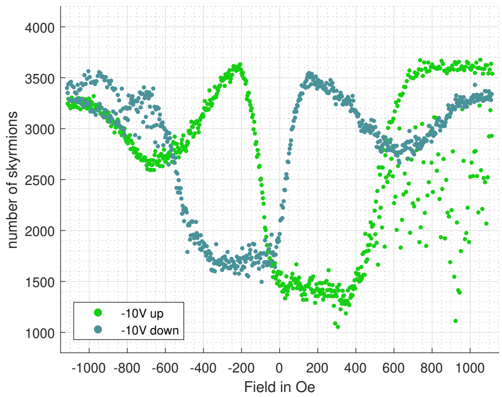

(c) Skyrmion count for ramping the magnetic field up and down at −10 V.

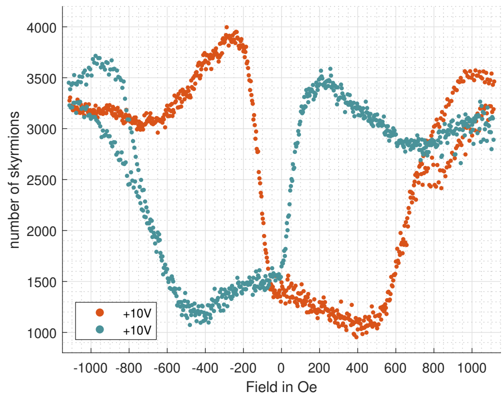

(d) Skyrmion count for ramping the magnetic field up and down at 10 V.

Figure 3.9: Number of skyrmions versus magnetic field while ramping magnetic field up at constant electric field for three different electric biases along the vertical line indicated in figure 3.11 B. (a) shows the case for ramping the magnetic field up at the three different electric biases, (b) shows the ramping down case. (c) and (d) show the ramp up and down curve for negative and positive bias, respectively.

for ramping up and down at negative and positive bias. Note that even in the purely helical phase (bottom of the well), the skyrmion count is non-zero. This is because of mishits in the automated skyrmion identification routine. More information can be found in the appendix. In figure 3.10 we show the corresponding real space images extracted all at the same magnetic field of 630 Oe but at different biases for the field ramping series acquired at 23 K and with their skyrmion counts displayed in figure 3.9 (a). At zero bias the state is between helical and skyrmion without either being clearly distinguishable. However, when applying a positive bias of +10 V, we are clearly in the helical phase while when applying −10 V we see individual pockets of skyrmions appearing. Finally, this is sufficient evidence that our device works and also gives us information about which conditions to choose for a controlled switching between helices and skyrmions.

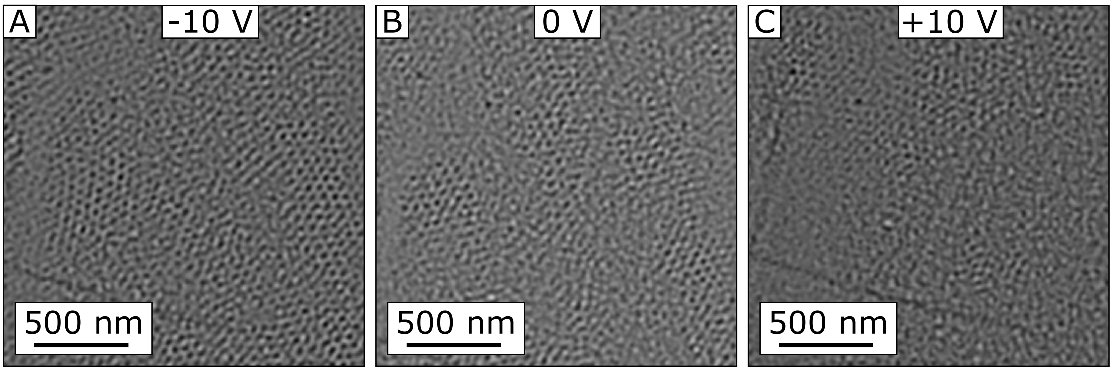

Figure 3.10: Real space images acquired at a temperature of 23 K and a magnetic field of 630 Oe but at different biases: −10 V (A), 0 V (B) and 10 V (C).

3.5 Reproducible Switching

In a next step we position ourselves at a point in the phase diagram between the sykrmion and helical phase to reproducibly switch between the skyrmionic and helical phase by applying a voltage of up to +20 V (−20 V). With the help of figure 3.11 we can see how at different biases the skyrmion configuration changes: compared to zero bias at the equilibrium size of the skyrmion pocket, a positive bias shrinks the skyrmion pocket while a negative bias makes the skyrmion pocket occupy a larger space in the phase diagram. This is equivalent to the

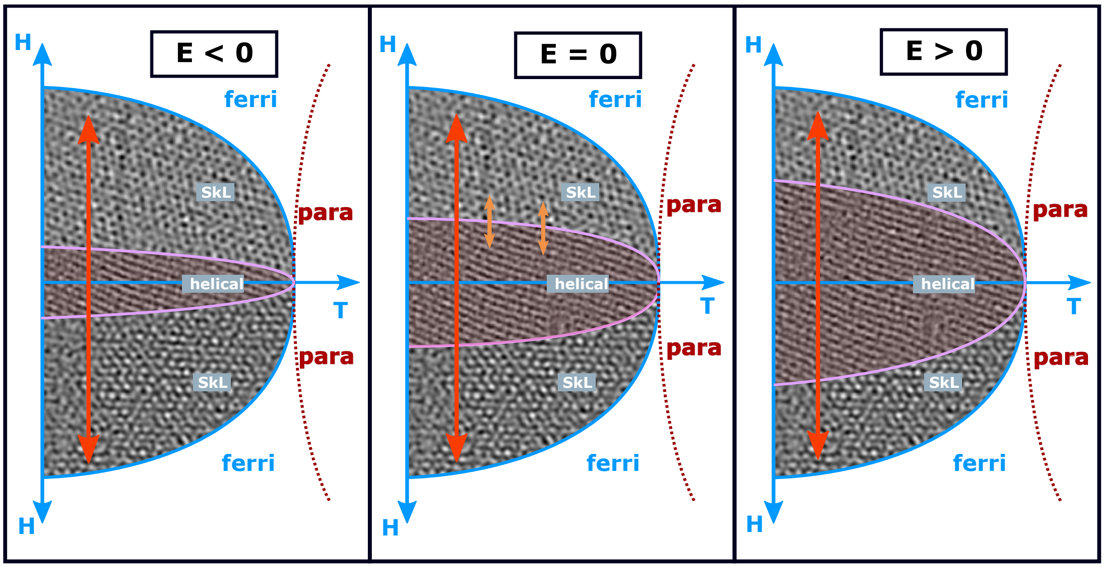

Figure 3.11: Schematic magnetic phase diagram under the influence of external electric bias. A negative electric bias $E < 0$ extends the size of the skyrmion phase compared to the equilibrium case $E = 0$, while a positive field $E > 0$ shrinks the skyrmion phase. The red arrows indicate the magnetic field ramp at constant electric bias. The orange arrows in the $E = 0$ case indicate the different magnetic fields and temperatures at which the electric bias is ramped or switched, see text.

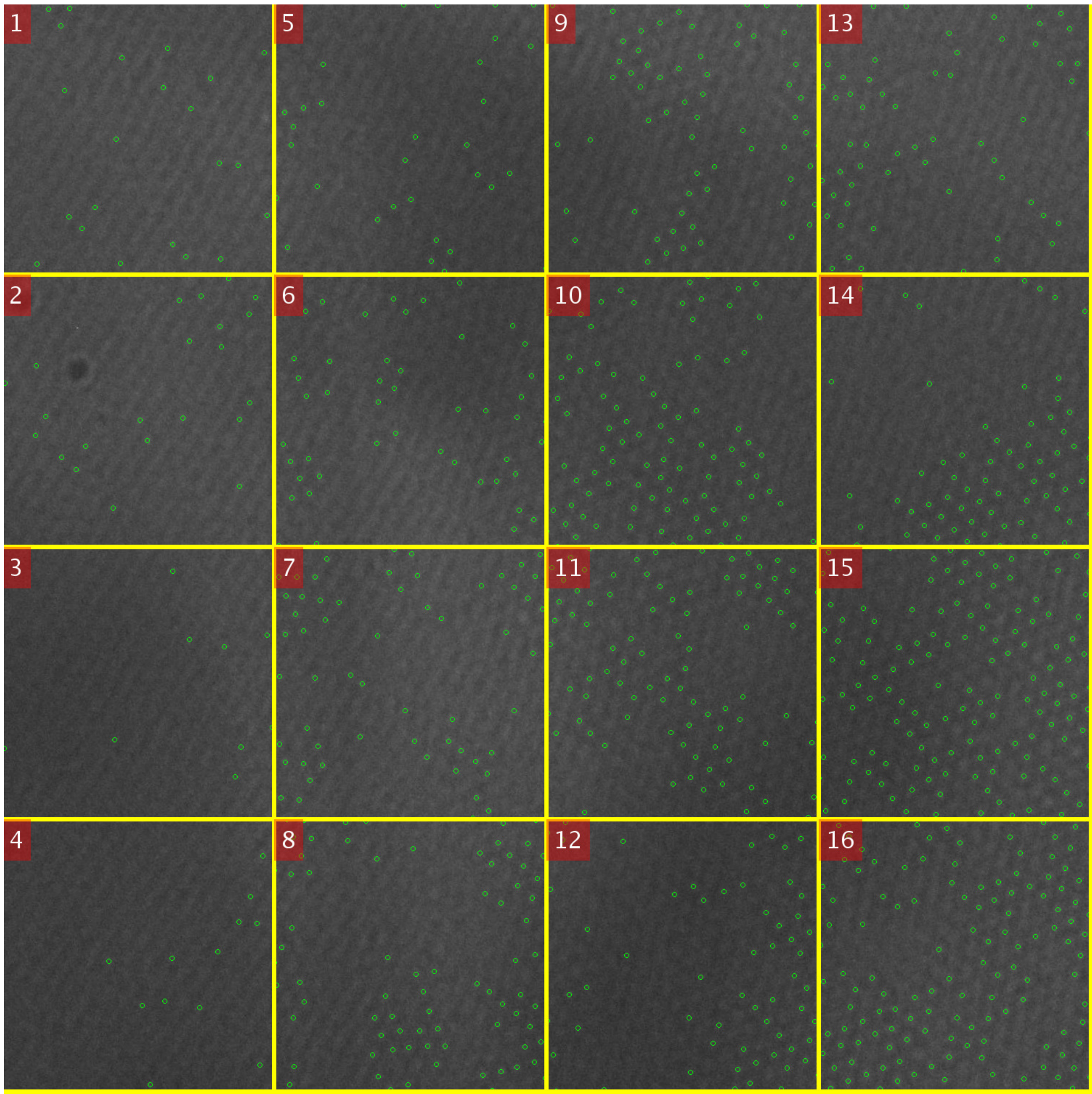

Figure 3.12: Exemplary frame of the series studies here, divided in 16 boxes in which skyrmions are counted.

case presented in figure 3.10 where the three images are taken at the same magnetic field but for a different electric bias. To switch between the helical and skyrmion phase we choose a magnetic field in the transition region between these two phases. The procedure of switching biases is repeated many times during the acquisition of a movie and we use the same algorithm as outlined before to identify skyrmions in each frame and thus the number of skyrmions at each given time and bias. During our experiments we notice how certain regions of the sample are more amenable to switch to the skyrmion phase, which is why we choose to divide the field of view in subregions as shown in figure 3.12. We count the number of skyrmions in each of those boxes individually, the result of which is depicted in figure 3.13. Each panel corresponds to a box shown in figure 3.12 and obviously only certain regions show a very clear switching behaviour (e.g. boxes 6,7,8,10 and 11), where a negative bias (green shaded area)

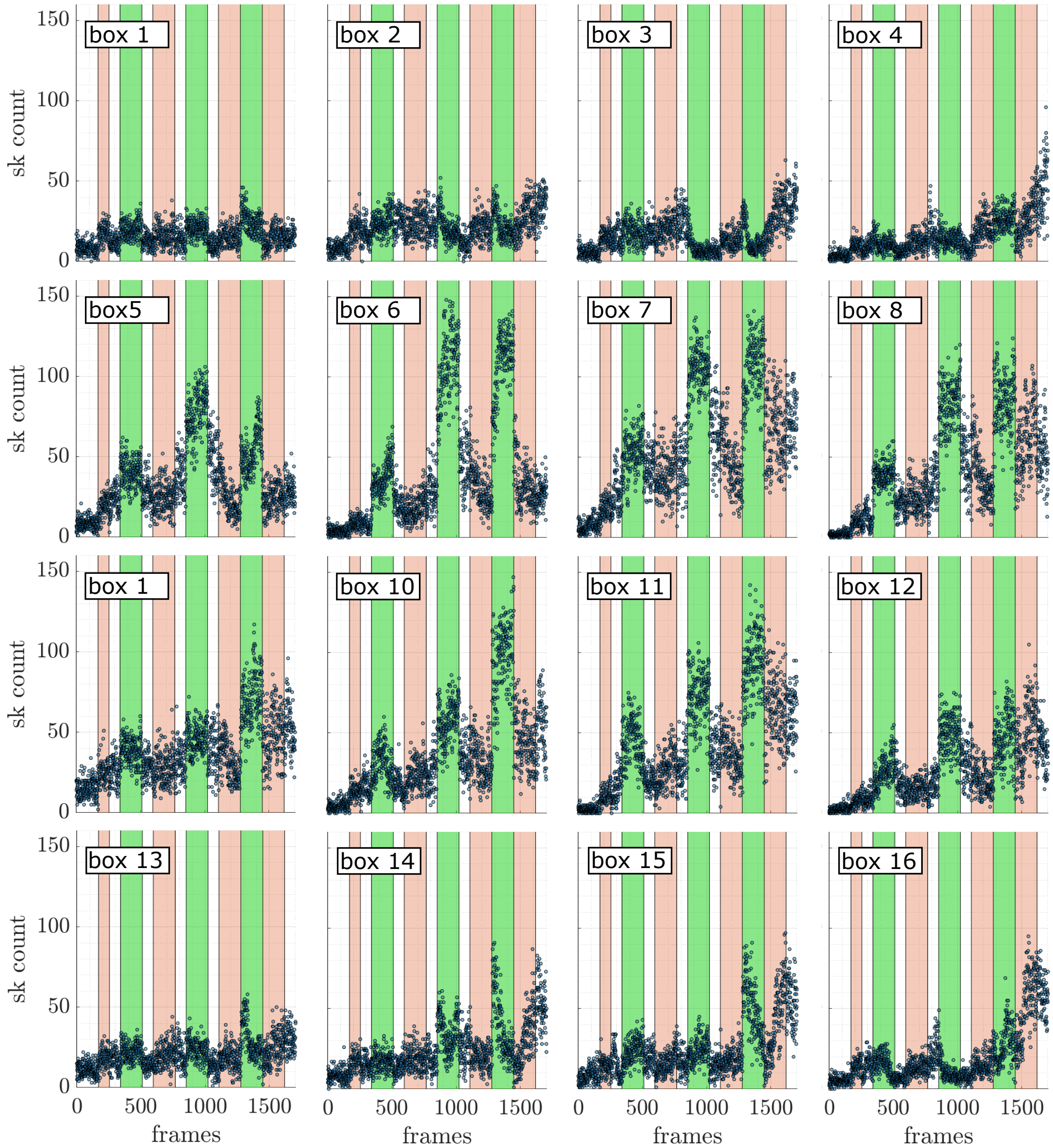

Figure 3.13: Number of skyrmions versus frames for a movie acquired at constant magnetic field while changing the electric bias. Green shaded areas indicate positive bias (20 V), red shaded areas negative bias (−20 V), and white areas no bias.

increases the number of skyrmions whereas a positive bias (red shaded areas) decreases their number. On the other hand, there are regions where in fact the opposite is true: e.g. in box 3 a negative bias actually decreases the number of skyrmions. We will discuss reasons for this in more detail below. We also see that switching from −20 V to 0 V generally barely changes the skyrmion number whereas doing so from +20 V to 0 V does so significantly. This imbalance is investigated in more detail when looking at the hysteresis loops below.

3.6 Write and Erase Times

Another important parameter is the relaxation time of the skyrmion number when switching the bias, i.e. the erase and write time. We extract these values from another series where switching between +20 V and −20 V is performed over multiple cycles. As in the examples above, the field of view is divided into 16 regions from which we extract the number of skyrmions in each frame. Examples of the number of skyrmions versus time from three different regions along with exponential fits are shown in figure 3.14. The constraints for the

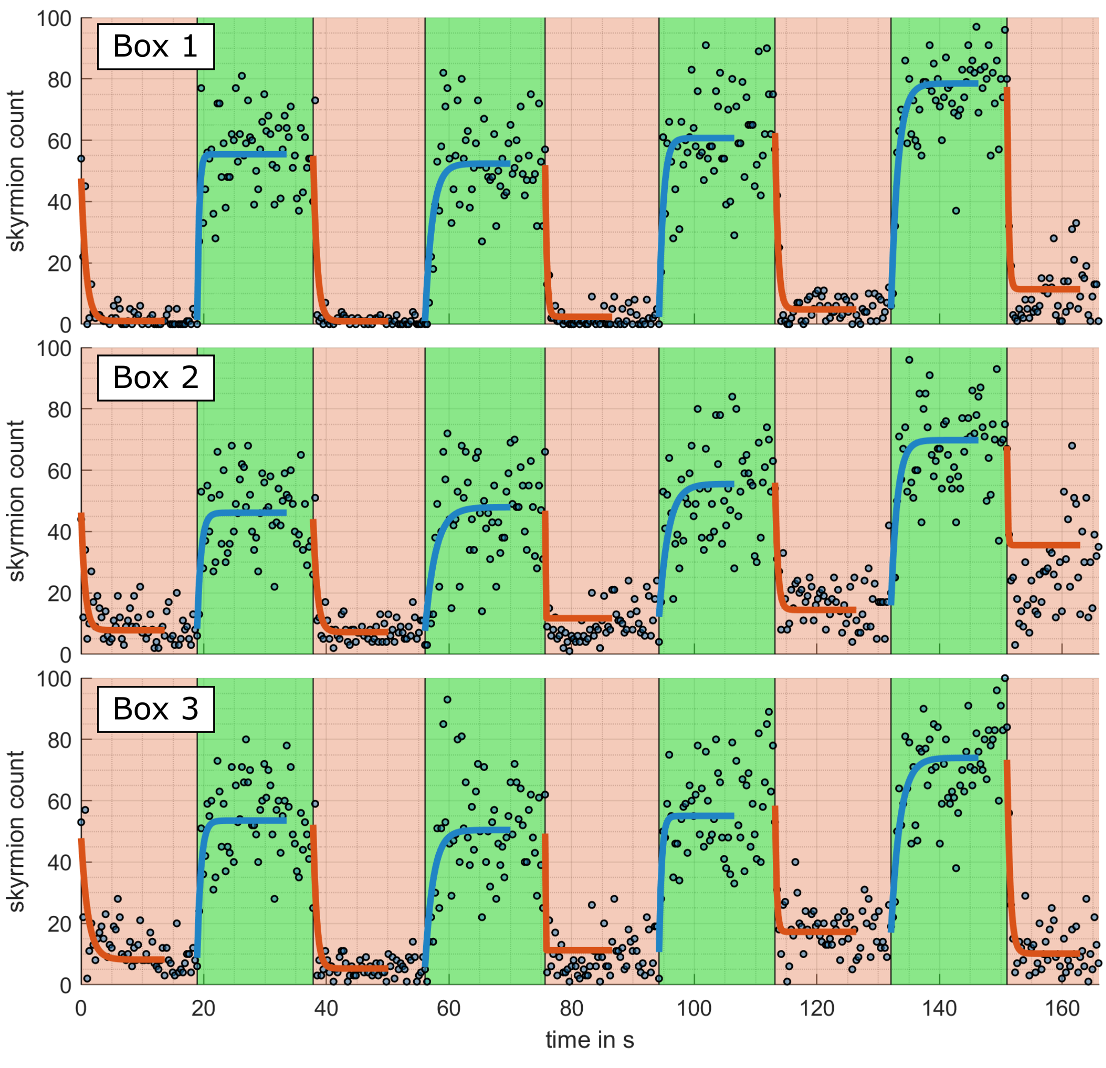

Figure 3.14: Erase and write cycles for a series with multiple switching cycles between +20 V (red shaded areas) and −20 V (green shaded areas). The plots are the skyrmion counts from one of 16 regions of the field of view as indicated by the box number, respectively. Exponential decays are fitted to the skyrmion count: blue for the write cycle, red for the erase cycle.

fits were chosen such that it relaxes into the mean of the numbers at the end of each cycle. The averaged time constants extracted from the fits both for the erase and write cycles are given in tables 3.1 and 3.2.

Table 3.1: Time constants (in seconds) for switching off

Box	1	2	3	4
1	0.16 ± 0.08	0.12 ± 0.1	0.17 ± 0.14	0.13 ± 0.1
2	0.15 ± 0.04	0.15 ± 0.06	0.07 ± 0.08	0.06 ± 0.11
3	0.17 ± 0.06	0.14 ± 0.04	0.09 ± 0.04	0.06 ± 0.08
4	0.07 ± 0.04	0.06 ± 0.1	0.06 ± 0.05	0.05 ± 0.05

Table 3.2: Time constants (in seconds) for switching on

Box	1	2	3	4
1	0.28 ± 0.14	0.40 ± 0.16	0.32 ± 0.17	0.43 ± 0.34
2	0.30 ± 0.14	0.29 ± 0.16	0.41 ± 0.18	0.64 ± 0.13
3	0.18 ± 0.11	0.35 ± 0.20	0.33 ± 0.12	0.61 ± 0.16
4	0.38 ± 0.13	0.38 ± 0.28	0.44 ± 0.07	0.44 ± 0.13

We see that the erase times are consistently smaller than the write times and differences between different regions do exist but errors are large at the same time. The overall mean write time for this specific series is $\tau_{\text{on}} = 0.39 \pm 0.12\,\text{s}$ and the the mean erase time is $\tau_{\text{off}} = 0.11 \pm 0.05\,\text{s}$. The time scales are governed by the energy landscape and in particular by the energy barrier between helical and skyrmion phase. Their energy can be tuned as a function of the applied electric field to make one or the other state energetically more favourable. While the height of the energy barrier also changes with the electric field (and the thickness of the device), it can only be overcome by thermal fluctuations, which is the physical limit for the speed of the write and erase process. Coming from a helical background, the skyrmion phase has a slightly higher energy than the helical phase [40], such that the energy barrier to be overcome for a negative applied electric field is still higher than for a positive one, thus explaining the different switching times we observe.

3.7 Hysteresis Loops

To explain the different switching behaviour depending on the starting bias, we examine the hysteresis of the system by ramping the electric field at a given magnetic field. The results are depicted in figure 3.15. The dots are data points and the solid lines are moving averages. The color coding is from blue at the start of the loop to red at the end. Similarly to before, we subdivide the field of view into 16 subregions to identify possible changes in behaviour across different sample areas. Note that while the sample that has been used to take the data is the same, these series have been performed during another experiment and the field of view may not exactly be the same as for the switching series shown above. The behaviour again strongly depends on the region of the sample. While box 10 exhibits a behaviour that matches most an expected hysteresis loop this is much less the case for the other regions. Nevertheless,

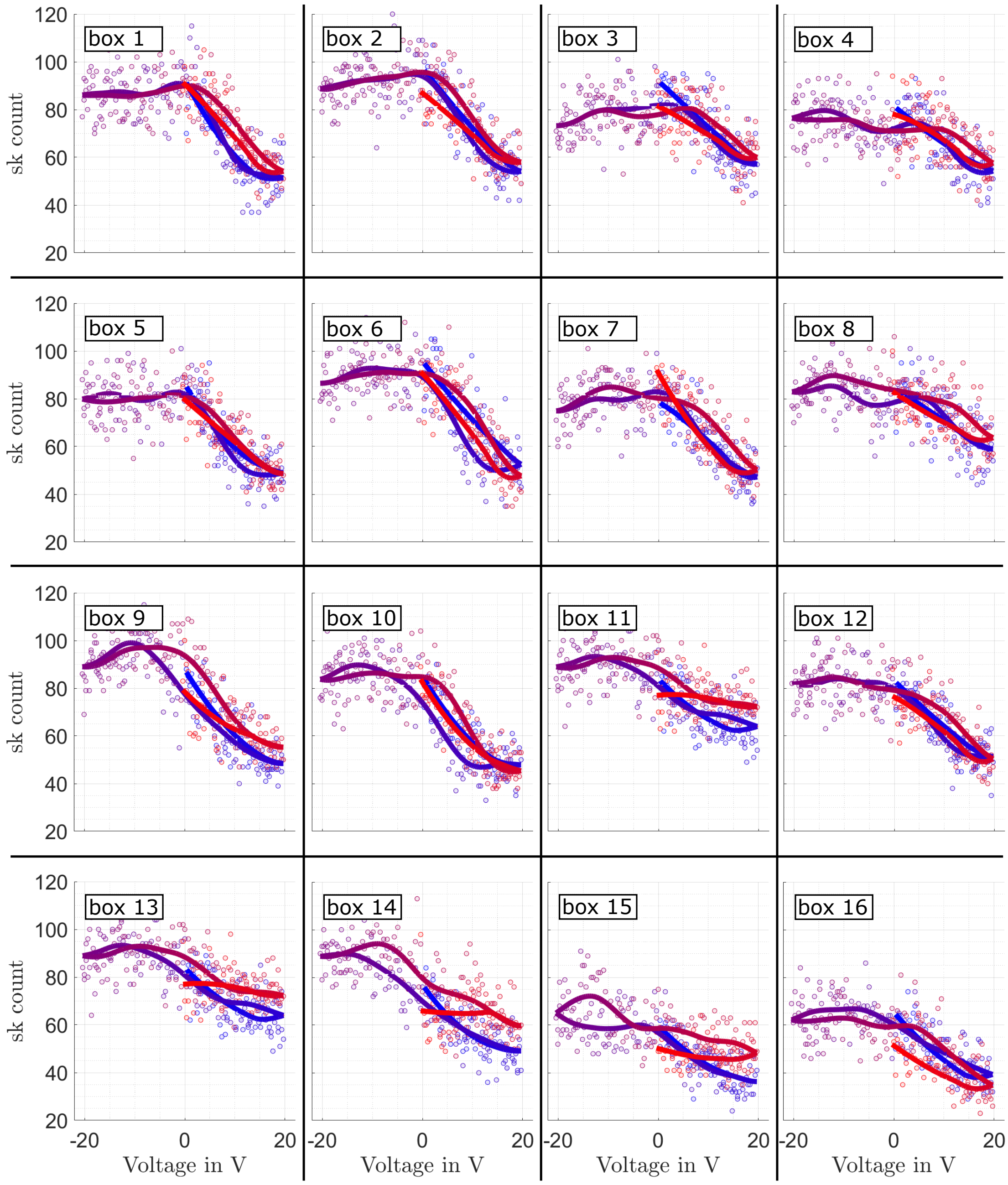

Figure 3.15: Hysteresis loops of the skyrmion count in each of the 16 subregions of the field of view while changing the electric bias at a constant magnetic field. Dots are extracted skyrmion numbers, solid lines are moving averages. The loops start from blue and go to red.

even there the behaviour is in accordance with the behaviour we see in the switching series: coming from −20 V and switching off the bias usually barely changes the number of skyrmions whereas when coming from the positive side the change is significant. In most of the loops we furthermore notice a tendency that the true center of the loop does not seem to be at zero bias but rather shifted to around 10 V. This is particularly obvious in the case of box 10. This may mean that we were not exactly at the magnetic field between both sykrmion and helical phase, although we also know that the hysteresis of the number of skyrmions is huge depending on the field direction as shown in 3.9 (c) and (d). Therefore, the reason why the electric ramp hysteresis is not centered around zero may depend on a number of factors and is hence not obvious. However, we do see that the loop opens up, and a remnant skyrmion number is crucial for potential skyrmion based memory devices.

3.8 Multiarray Geometry

In order to move closer towards an addressable skyrmion memory, we adapt the sample preparation in order to produce an array of electrodes instead of the single pair of electrodes sandwich geometry as outlined before. Such a multi-array configuration is schematically depicted in figure 3.16.

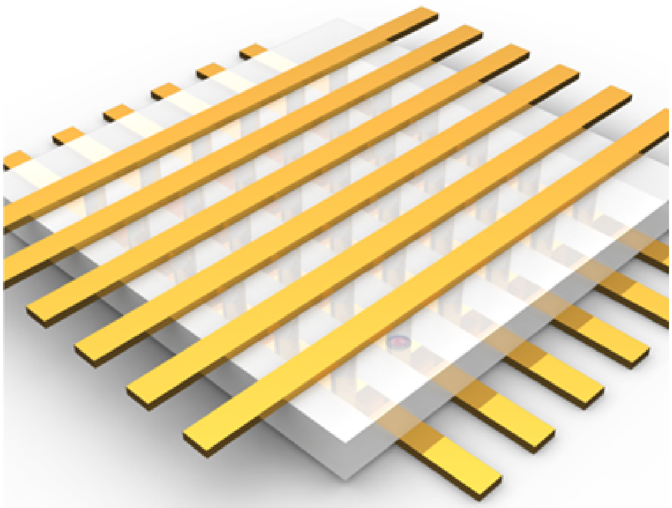

Figure 3.16: Schematic of the proposed multi-array geometry to allow local skyrmion control.

At each electrode crossing an electric field can be applied to locally switch between the helical and skyrmion phase. The most challenging part is to put the top electrodes onto the lamella. To this end, we use excess material of the pre-thinned lamella as a mask prior to the metal deposition in the electron beam evaporator. The idea is to have a bar stretching across the whole length of the lamella so that it prevents a certain area from being covered with the metal electrode and thus separating the area to create an array. Figure 3.17 shows how we turn the Omniprobe grid by 90° in the sample holder and bend prong A to the side in order to access the lamella from the other side. Figure 3.18 shows a close up of the pre-thinned lamella in this configuration.

The ions in the FIB come down from the top and mill along the long edge of the lamella. The result can be seen in figure 3.19. The bar protrudes about 2 μm from the lamella. In a next step the bar is physically disconnected from the lamella by milling a gap between it and the

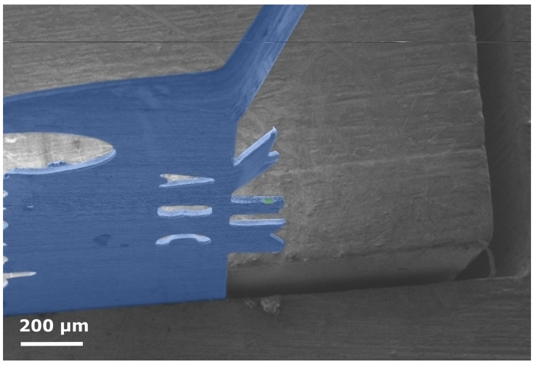

Figure 3.17: Bent prong A of Omniprobe grid to access lamella with FIB when turned by 90°.

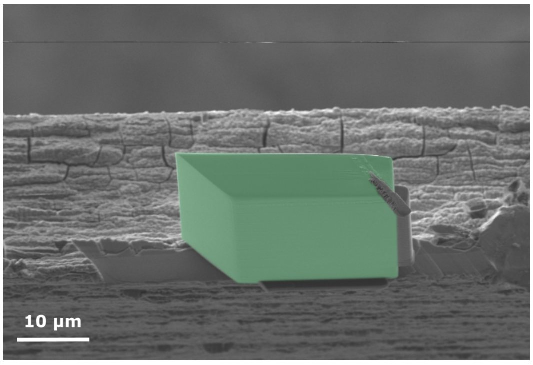

Figure 3.18: Close up of lamella turned by 90°. Thicker than usual, extra material used to create mask.

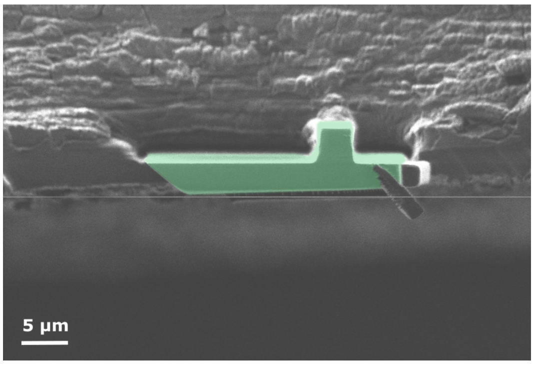

Figure 3.19: Profile of lamella, protruding bar is the mask.

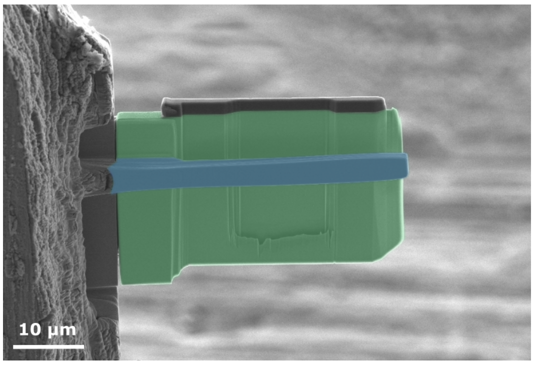

Figure 3.20: Final thinning of lamella as usual; bar (blue) acts as mask.

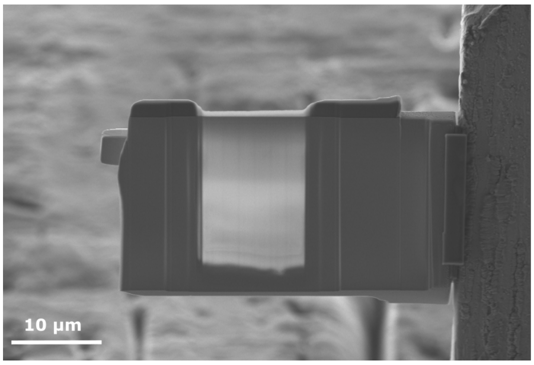

Figure 3.21: Lamella after final thinning.

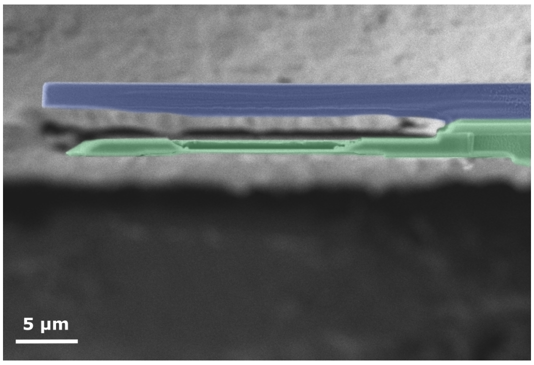

Figure 3.22: Top view on lamella (green) and mask/bar (blue).

lamella so that it stands free and the usual milling procedure is adopted to thin down the lamella to electron transparency. The final lamella along with its mask is depicted in figures 3.20, 3.21 and 3.22. Note the gap between the lamella (green) and the mask (blue). The mask stretches beyond the end of the lamella to ensure that upon evaporation the two electrodes will be fully separated. After evaporation (bilayer of 10 nm of Ti and 2 nm of Pd) the mask needs to be removed, which is shown in figure 3.23. Finally, the lamella is transferred onto the chip with four electrodes (two bottom electrodes and two electrodes to be contacted with the electrodes directly deposited on the lamella), as shown in figure 3.24. TEM images of the

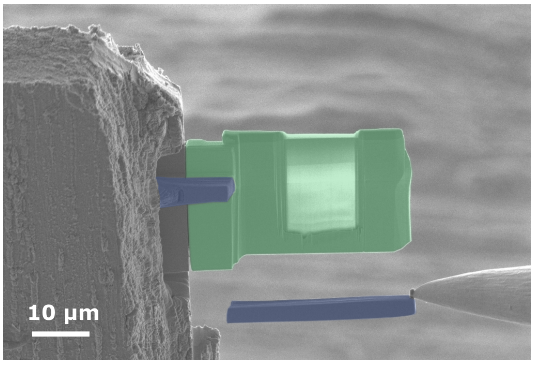

Figure 3.23: After metal evaporation remove mask with micromanipulator.

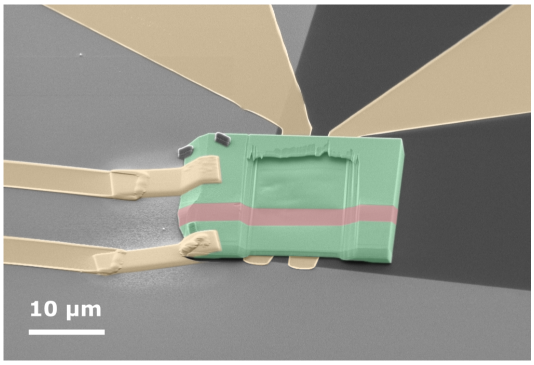

Figure 3.24: Transfer lamella on chip with two electrodes (gold shaded) and connect to contact pads by Pt deposition (gold shaded). Red shaded area shows gap in electrode (mask).

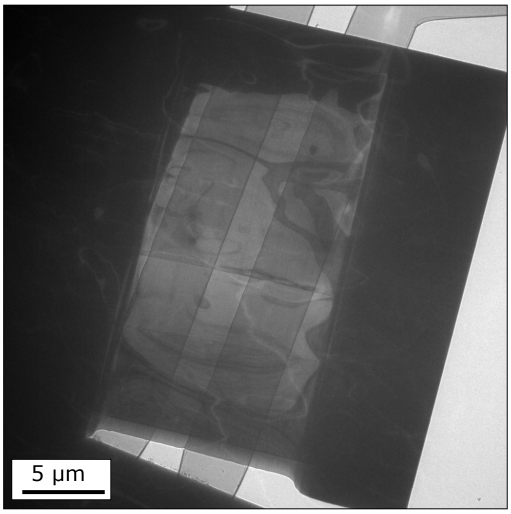

Figure 3.25: Device in the TEM. The bottom electrodes are vertical, the top ones horizontal across the sample.

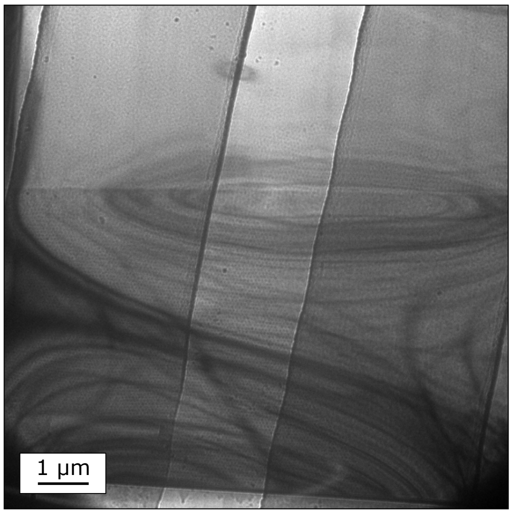

Figure 3.26: The four electrode crossings are the active areas of the device.

device are shown in figures 3.25 and 3.26. We applied a similar protocol as in the single pair of electrodes case described above by choosing a magnetic field at the helical to skyrmion phase boundary and performing the switching of the bias there. However, we were not able to produce a homogeneous condition across the sample, i.e. being at more or less the same mixed helical-sykrmion phase. Instead, we would rather be in a situation where e.g. the lower left part of the device would be filled with skyrmions while the rest of the field of view would be empty. This would be necessary, though, to show local switching. In fact, in the single pair of electrodes case above, we always picked a certain area of the sample to observe the switching and even within a restricted field of view of a few microns, it was not homogeneous. Since we cannot accommodate more than four electrodes on the lamella (at least not with this approach), we need to take the whole field of view of the lamella into account. Yet variations across such a distance e.g. in sample thickness can change the phase diagram significantly. More on this will be discussed below.

3.9 Discussion and Conclusion

In conclusion we successfully demonstrate the writing and erasing cycle by real space imaging using LTEM in the magnetoelectric skyrmion host Cu_2OSeO_3 in a geometry that is most suitable for technological application. Thanks to our skyrmion point identification algorithm we can directly access quantities of interest by counting the number of skyrmions in a given frame: we obtain the switching behaviour between two states (helical and skyrmions in helical background) and from this the reaction times upon bias change. By scanning through the electric field we further find some hysteresis in the system that could be exploited for magnetic storage.

We have collected a vast amount of data, from in total five samples, scanning systematically through magnetic and electric fields and temperature, yet there is no conclusive indication as to how these parameters play into the strength of the effect. Overall, the limits are set by both equipment and sample preparation. We cannot be entirely sure about the effect of the beam intensity, which had to be relatively high due to the thickness of the stack observed (lamella plus substrate plus electrodes). The electrode deposited directly on the lamella is another factor, perhaps changing the energy at the surface and/or the DMI. The lamella may not be entirely homogeneous in its composition with locally higher concentrations of defects due to gallium ion implantation during the fibbing process. More crucially, the thickness of the lamella is not exactly the same everywhere, which is known to significantly influence the phase diagram [37]. The same is true for lamellas under stress [56]. There are three main ingredients contributing to both internal and external stress: first, the sample preparation procedure that by ion implantation can increase local stress, secondly, the fact that the lamella was placed on a substrate and had to be fixed the edges, and lastly, the biasing of the device itself. The latter is actually clearly visible as the bent contours move considerably upon bias change, as illustrated in figure 3.27. In this particular sample and field of view the number of skyrmions increases upon application of a positive biases as opposed to what we expect and see normally. This is accompanied by a change in bent contours which is indicative of a change in stress of the sample.

These factors make it especially tricky to investigate skyrmion switching at a local level as we have tried with our prototype multi-array device. The centres of each electrode crossing are each a few microns apart from each other. This is enough that conditions are not necessarily the same across the sample despite e.g. constant magnetic field and temperature. Even with a

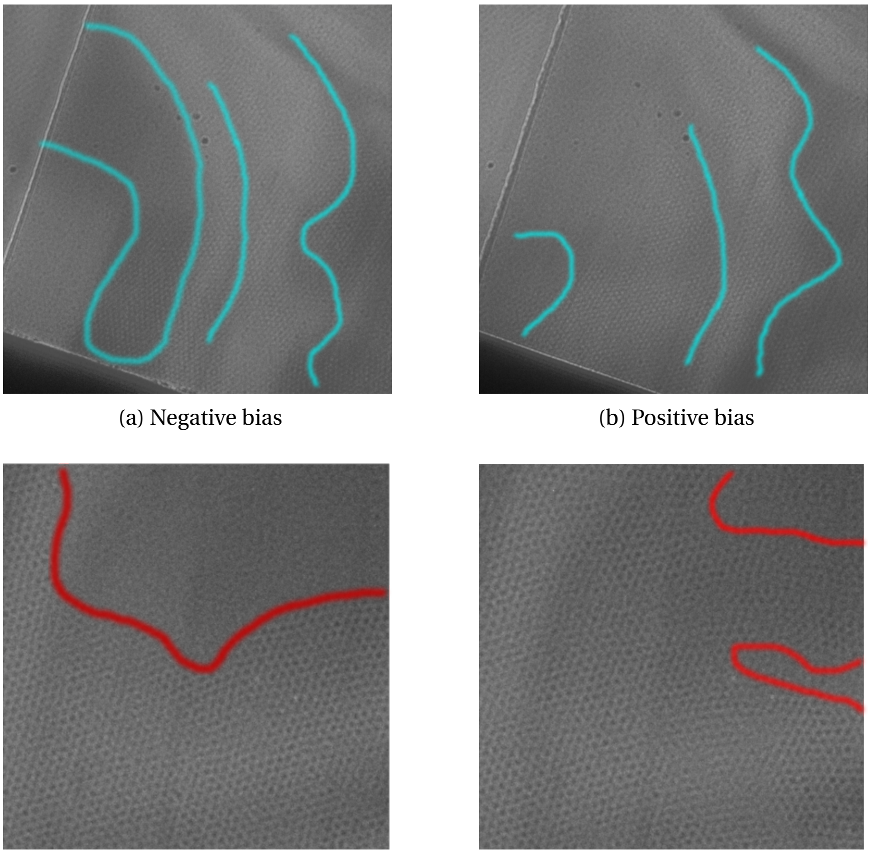

(a) Negative bias (b) Positive bias

(c) Negative bias (d) Positive bias

Figure 3.27: Example of bent contours of lamella at two different biases, negative (a) and positive (b), and the resulting local skyrmion configuration, (c) in the case of negative bias and (d) in the case of positive bias. In this special case, a positive bias actually increases the skyrmion number, presumably due to a stress induced change in the phase diagram.

single pair of electrodes layout we see considerable local changes in the ability to switch and we therefore do not expect this to be different for a multi-array layout.

While these experiments offer valuable insights into local electric field control of skyrmions despite the pitfalls discussed above, one main challenge remains the reproducibility of the samples. Each TEM lamella coming out of the FIB is unique and even more so the assembled device (chip plus lamella). Addressing these issues is beyond our control at this point. This will change once it is possible to grow thin films of Cu_2OSeO_3 (or a new type of magnetoelectric material that would host skyrmions even at room temperature), which would allow to eliminate many of the problems discussed above. One could potentially adopt a similar strategy as in [57] where strain-free thin films of the β-Mn type skyrmion host $Co_{10\text{-}x}Zn_{10\text{-}y}Mn_{x+y}$ have been grown using molecular beam epitaxy (MBE). Another approach would be pulsed laser deposition, a promising technique for thin film oxides [58]. This would be no less than a game changer for the entire project since device fabrication could be completely and seamlessly integrated into the current clean room microfabrication process, and the prototyping process could be sped up drastically. Then it would be also possible to explore the possibility to integrate this new type of skyrmion memory into existing transistor technology to read out the state all-electrically.

4 Defect Alignment at Grain Boundaries

In this chapter we introduce essential concepts that will recur throughout the remainder of this thesis. We discuss how defects arise in lattices in general and particularly what role they play in skyrmion lattices. We show how defects align along skyrmion grain boundaries and extract the relationship between grain boundary alignment and defect spacing to find an agreement with geometric expectations. To this end, we perform a statistical analysis of a dynamically evolving skyrmion configuration instead of having to create well-defined grain-misalignments. We develop an algorithm that can automatically and reliably extract and classify low angle grain boundaries and the strings of defects that they are composed of. We furthermore present a more general method to extract domains in skyrmion lattices and visualise domain boundaries [1].

4.1 Defects and Grain Boundaries

Most non-organic matter is crystalline. Apart from some obvious jewellery like diamonds and gemstones, all metals are crystalline and most of the rocks that surround us. However, we rarely notice this since most of those things are polycrystalline, i.e. they have small crystalline grains with different orientations. Grain boundaries are interfaces between adjacent misoriented grains in a polycrystalline material and are composed of crystalline defects called dislocations. One rarely encounters single crystals except for those made in the lab or for some very special applications such as single crystal jet engine blades [59]. Otherwise we are mostly dealing with polycrystalline matter and it contains a lot of defects. While this seems discouraging at first, in fact a major part of today's technology is based on the controlled engineering of crystal defects. Think about the doping of semiconductors to change their electric properties that allows to produce the transistors that are used in all modern devices. Another great example is the manufacturing of steel and other alloys. Their properties ranging from electrical and thermal conductivity, to ductility and hardness crucially depend on the size of crystalline grains and the amount of defects separating them [60]. For example the plastic deformation of metal

[1] The results presented in this chapter are published in [50]. Some parts are quoted verbatim.

results from the movement of crystal defects through crystalline metal grains thus deforming the grain itself when provided with enough stress or heat. However, the movement of defects stops at grain boundaries and therefore a well known recipe to increase metal hardness is to decrease the size of its crystalline grains. Metalsmiths had no idea about the atomic structure of the steel they forged hundreds of years ago, but had great empirical knowledge to use dislocations and grain boundaries to create some of the finest and strongest swords [60]. Modern metalsmiths, also known as material scientists, have fantastic tools like electron microscopes at their disposal to study defects in materials in great detail.

Defects can be categorized according to their dimensionality from zero-dimensional to three-dimensional defects. Zero-dimensional defects are point defects such as interstitial atoms that occupy the space between atoms or vacancies. Phase boundaries (two adjacent and different phases, e.g. quartz and feldspar in granite, clearly visible by the naked eye) and stacking faults (e.g. stacking sequence ABCABABC in a hexagonal crystal) are two-dimensional defects. Three dimensional defects are for example voids and precipitates, which is a different phase contained within a crystal. Dislocations are one-dimensional defects and of primary interest in this chapter, since they constitute the grain boundaries that we study here. A dislocation is generated by the insertion of a lattice half-line as illustrated in figure 4.1 in the case of a square lattice and two lattice half-lines in the case of a triangular lattice, see figure 4.2. There is no continuous transformation to make those dislocations disappear which is why they are called topological. The only way is to cut the lattice as indicated by the dashed line in figures 4.1 and 4.2 and to shift the lattice such that the points A and A', B and and B' and so on are brought next to each other, which is known as the Volterra cut [61]. The so called Burgers vector $\boldsymbol{b}$ characterizes the strength and orientation of a dislocation [61]. It can be constructed by following a fixed number of bonds along the path around the dislocation. The difference between the start and end point is the Burgers vector $\boldsymbol{b}$ as illustrated in figures 4.1 and 4.2.

4.2 Skyrmion Lattices

Skyrmions most commonly appear in the form of a triangular lattice. There are two distinct ways of how to describe these lattices: either in the wave picture by considering the superposition of three q-vectors or in the particle picture. Although individual skyrmions have been found in various systems [62, 63], much until recently the question of how much of a particle-like behaviour skyrmions adopt in a lattice configuration was less clear. However, recent studies provide strong evidence to support a quasiparticle description in the lattice phase [64]. The particle-like behaviour of skyrmions offers the possibility to study lattices, defects and phase transitions in 2D. While the framework for the analysis of reciprocal space data is well established in various neutron scattering studies [65, 66], this is much less the case for real space data. This therefore calls for the development and implementation of suitable image processing algorithms and real space data analysis routines. We follow along these lines by looking at imperfect lattices and mismatched lattices to study the behaviour of defects at grain boundaries within the particle picture using transmission electron microscopy (TEM).

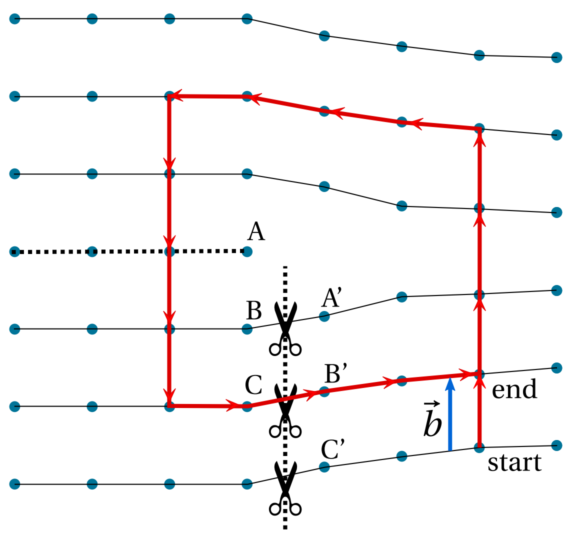

Figure 4.1: Dislocation in a square lattice by insertion of a half lattice line (dashed line going to A). The Burgers vector ***b*** is constructed by starting at any lattice point (start) and going around the defect a fixed number of bonds (four in our case, red line). The difference between the end and starting point is the Burgers vector. The dislocation can be removed by cutting the lattice as indicated and bringing points A next to A', B next to B', etc.

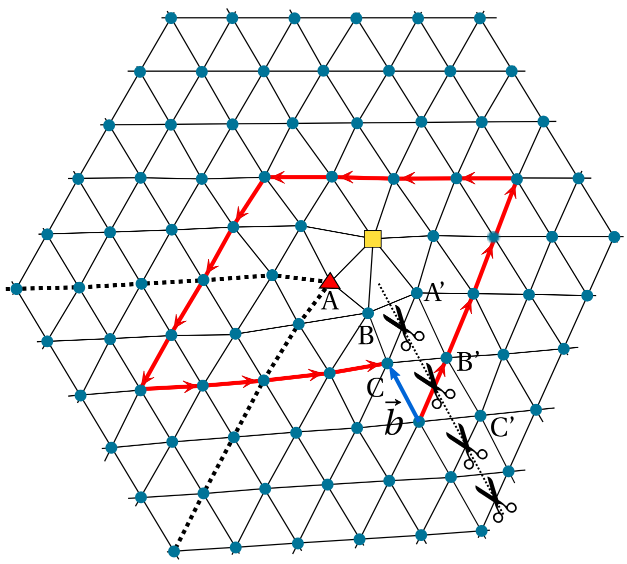

Figure 4.2: Dislocation in a triangular lattice are obtained by the insertion of two lattice half-lines (dashed lines leading to A). Construction of the Burgers vector ***b*** and cut to remove the dislocation as in figure 4.1. The red triangle indicates a 5-fold coordinated site ("5-defect") and the yellow square a seven-fold coordinated site ("7-defect").

Furthermore, we provide another example of how real space imaging of skyrmions can be used as a testbed to explore structural dynamics and order in condensed matter systems.

Defects, dislocations, twin and grain boundaries in skyrmion lattices have been found in prior studies [47, 29, 67, 68, 69]. There is only one study so far to look into dynamically rearranging grain boundaries [70]. However, their algorithm is not explained in more detail and relies on manual corrections for low angle grain boundaries. We develop an algorithm that reliably extracts low angle grain boundaries from hundreds of TEM frames in an unsupervised manner.

4.3 Sample Preparation and Methods

We follow the procedure as outlined in chapter two to produce a TEM lamella of Cu_2OSeO_3 for our observations. We use cryo-Lorentz transmission electron microscopy (LTEM) in Fresnel mode to acquire a movie of a dynamically evolving skyrmion lattice configuration in real space and real time. LTEM is an ideal technique to acquire movies of such a system since it allows for large fields of views and relatively short acquisition times. Stable skyrmion lattice configurations are observed at about 30 K after field cooling at 640 Oe. We acquire a movie for several minutes with an exposure time of 336 ms at a resolution of 4096×4096 pixels while maintaining a constant field and temperature. To analyse hundreds of frames each containing around 13000 skyrmions, we have written custom Matlab codes to analyse all TEM images.

4.4 Defect Identification

In order to carry out the analysis, the position of each skyrmion for all the frames in the movie must be determined. To this end, we have developed a dedicated identification routine, which includes multiple correction steps that allow for a reliable identification even in blurry microscope images. Steps include the application of a log-type filter to smoothen the image and enhance contrast and the identification of local minima in image intensity. These local minima can in principle be identified as skyrmion positions if the intensity is below a certain threshold (determined by inspecting the result visually). More details can be found in the appendix. An exemplary TEM image is shown in figure 4.3 and in its filtered version in figure 4.4 along with the identified skyrmion positions in figure 4.5. Based on these identified points we can construct the so called Delaunay triangulation shown in figure 4.6. It triangulates a given set of points such that it maximises the inner angles of any triangle. It therefore can provide information about the number of nearest neighbours of any given point. An equivalent construction is given by the Voronoi tessellation depicted in figure 4.7.

It is a construction of polygons that encompass points that are closer to a particular skyrmion position than any other position. This way the Voronoi construction is an area filling structure that tiles the the whole image ("tessellation"). The edge sharing polygons therefore also yield information about the number of nearest neighbours of each skyrmion. In fact, the Voronoi tessellation and Delaunay triangulation can mutually be transformed to each other. This can be seen from the inset in figure 4.7. The polygons are constructed by taking the midpoint of the edges in the Delaunay triangulation and drawing a line perpendicular to the edge. The number

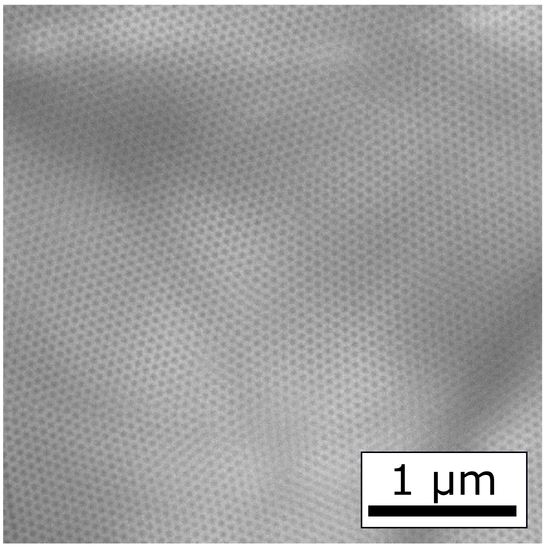

Figure 4.3: Raw TEM image (frame 150).

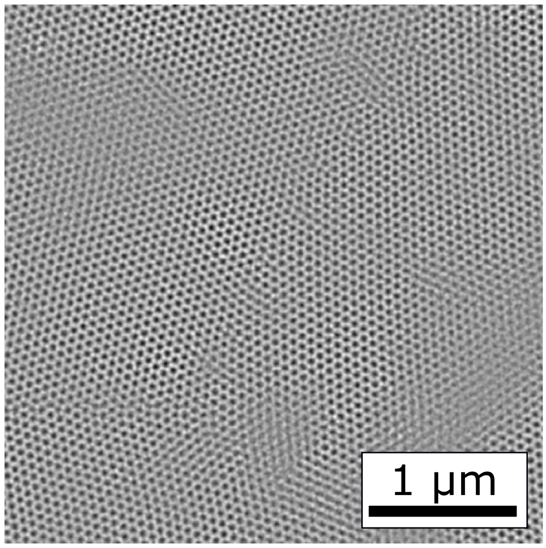

Figure 4.4: TEM image after application of a log-type filter.

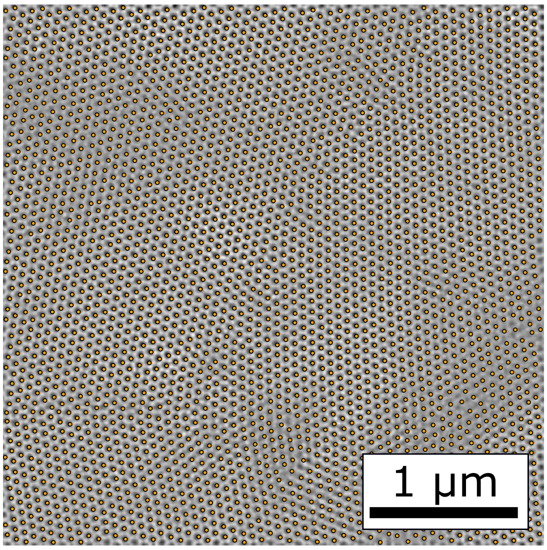

Figure 4.5: Filtered TEM image (frame 150) along with identified skyrmion positions (dots).

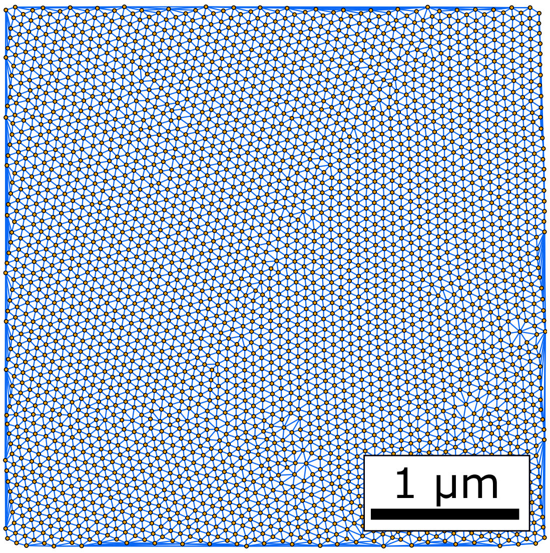

Figure 4.6: Delaunay triangulation (blue) based on identified skyrmion positions.

of corners of each polygon is equivalent to the coordination number of the corresponding point. Transparent polygons in figure 4.7 mark regular six-fold coordinated sites whereas red polygons represent all non-six-fold coordinated sites that hereafter are referred to as defects. The most common defects are 5- and 7-defects that in the solid phase often appear as 5-7-pairs. These are the dislocations that we introduced above. We can nicely see from figure 4.7 how the dislocations line up as strings, which is where two skyrmion domains of different orientation meet. Our goal is to extract those strings from all frames of the series in an automated fashion.

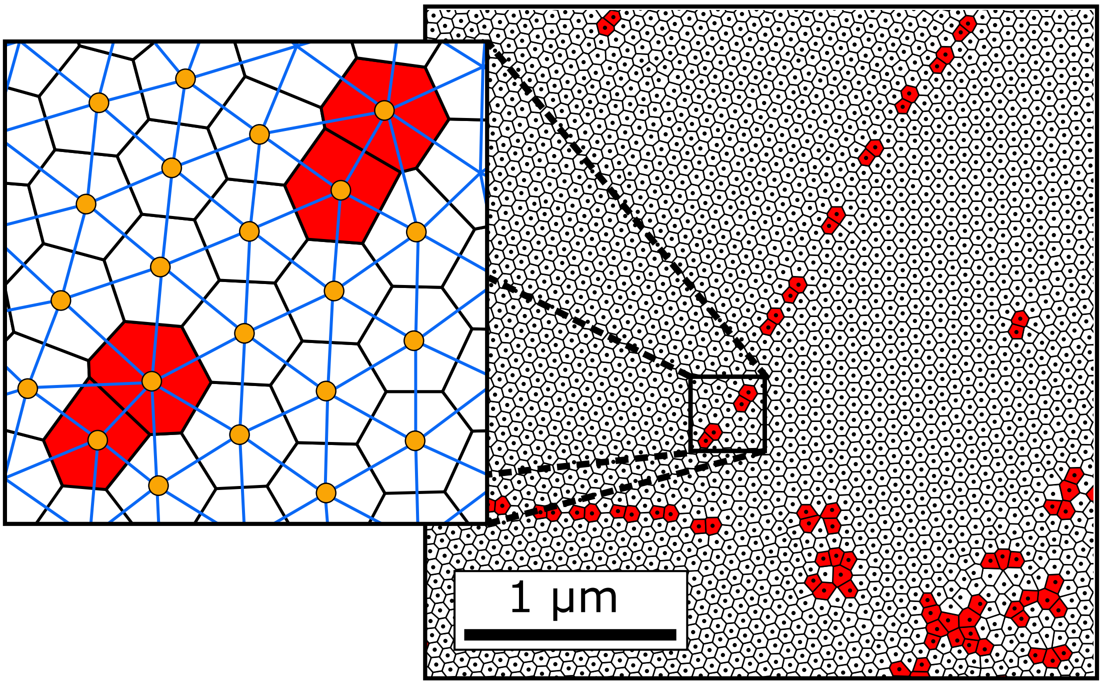

Figure 4.7: Voronoi diagram of the skyrmion positions as extracted from the TEM image. White polygons are 6-fold coordinated sites, red polygons are sites of any other coordination number, referred to as defects. The inset illustrates the relationship between the Voronoi tessellation and the Delaunay triangulation.

4.5 Extracting Dislocation Strings

The vertices of each polygon in the Voronoi diagram are used to calculate the local orientation for each skyrmion. Due to the hexagonal symmetry of the lattice these angles are between -30° and 30°, as shown in figure 4.8. This way, the different domains are clearly revealed and we see how they are separated by strings of dislocations (defect pairs). Our goal is to extract these defect lines in order to determine how the spacing of dislocations is related to the relative orientations of the adjacent regions. Since a controlled twisting of lattice orientations is hard to achieve, we study an entire movie and tackle the problem from a statistical point of view. Based on the angle map we use a box scanning algorithm to identify the regions where the largest changes in angle occur, from which we can extract the defect lines, see figure 4.9. Multiple regions may be detected and we retain the few largest clusters. Defects within those clusters can then be identified to belong to a string of defects separating two adjacent regions. Since the dislocations in one such cluster may not necessarily belong to one string (see the strings in figure 4.8 separating blue, red, and green domains) we further need to segment the extracted strings into substrings. This is first based on the distances to the nearest dislocation neighbours of a dislocation and then refined by splitting strings further into substrings when distances and angles between dislocations exceed a certain threshold. This way, we obtain in one frame individual strings on each side of which we can probe the orientation of the

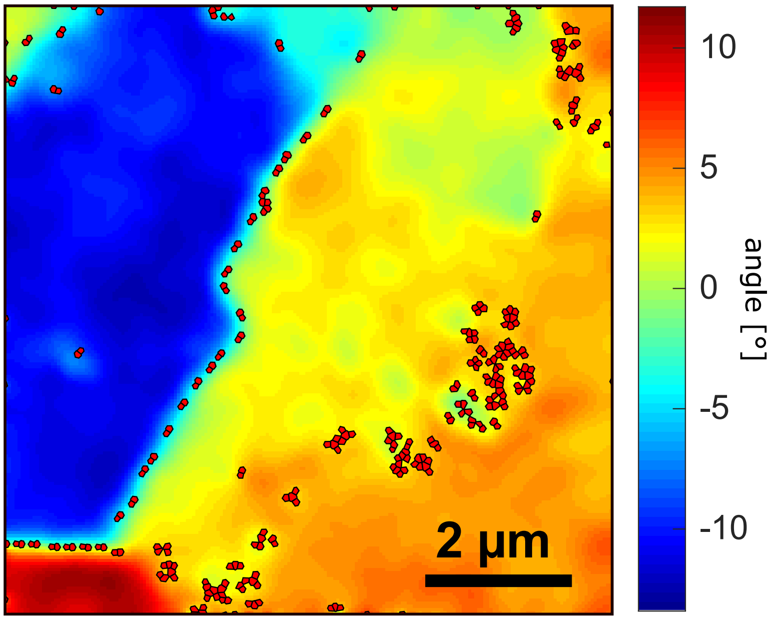

Figure 4.8: Angle map revealing the different lattice domains.

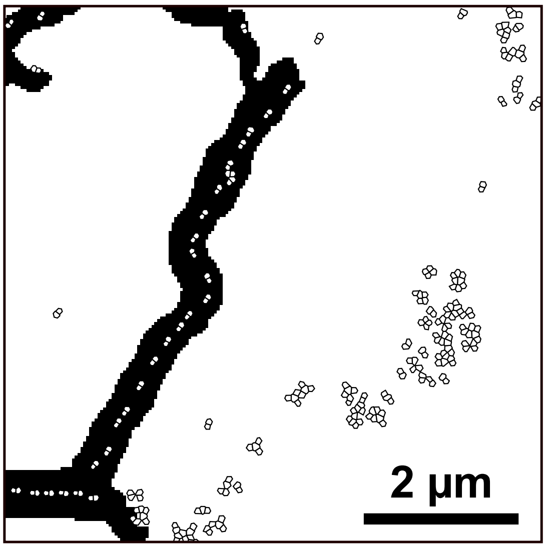

Figure 4.9: Based on the angle map, regions of large angular change are extracted.

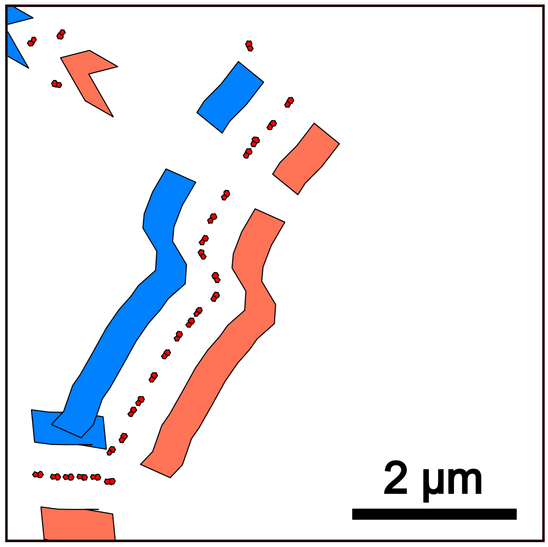

Figure 4.10: Probing the orientation to both sides to the extracted defect strings.

adjacent region, as illustrated in figure 4.10. Doing so for 151 frames in the sequence (from the 579 frames in the series studied here, clearly distinguishable grain boundaries only occur in frames 70 to 220) and taking strings with a length of at least three we obtain the plot in figure 4.11 for the relative angle of adjacent domains versus the median distance of dislocations in one string. For comparison, we do the same for pairs of dislocations only. Filtering for longer strings greatly helps to reduce the scattering of the data, although in both cases the

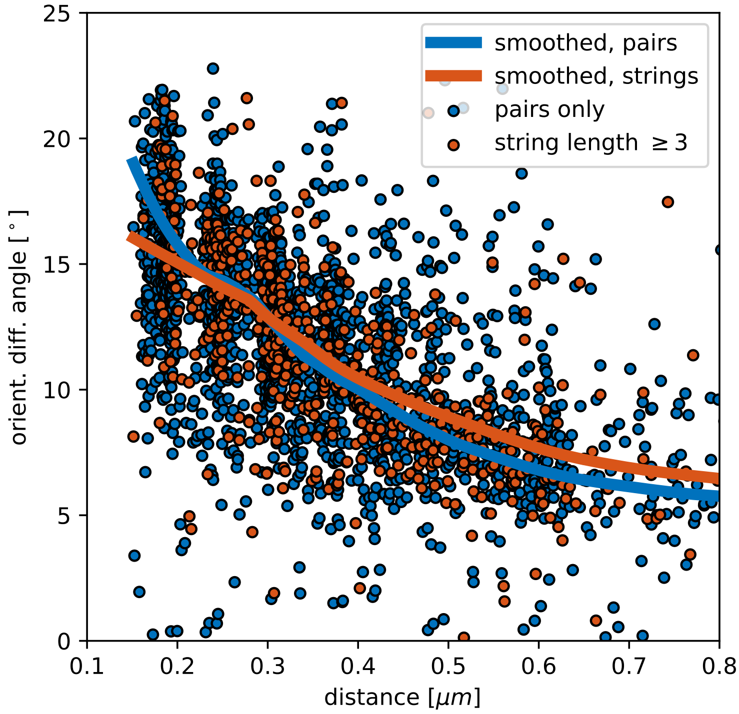

Figure 4.11: Comparing the difference in orientation versus median distance in the corresponding strings based on strings with a length of at least three (blue) and pairs of dislocations (red) along with smoothed curves.

trend (smoothed curve) is similar. One can also notice a certain accumulation of data points at discrete distance values, reflecting the discrete nature of the Voronoi tessellation. Note that the algorithm works autonomously and is not supervised after the initial threshold parameters are set (e.g. for detecting changes in angle).

We can further tweak our analysis by only looking at 'high quality' strings, i.e. we would like to discard strings that significantly comprise a large variation in distances and angles between dislocations and generally deviate from a straight line. Based on these quality criteria we attribute a 'quality factor' to each string - the lower this factor the better, as illustrated in fig 4.12. The choice of strings of different lengths and quality considerably affects the variation of data points around their mean, as seen in figure 4.13.

4.6 Lattice Twisting Geometry

To explain our observations, we inspect figure 4.14. Introducing a dislocation in a lattice means squeezing in an additional lattice line. A high density defect string results in many extra line spacings that can only be accommodated by a large twisting angle of the adjacent domains and vice versa for a low density defect string. We see in the illustration how this

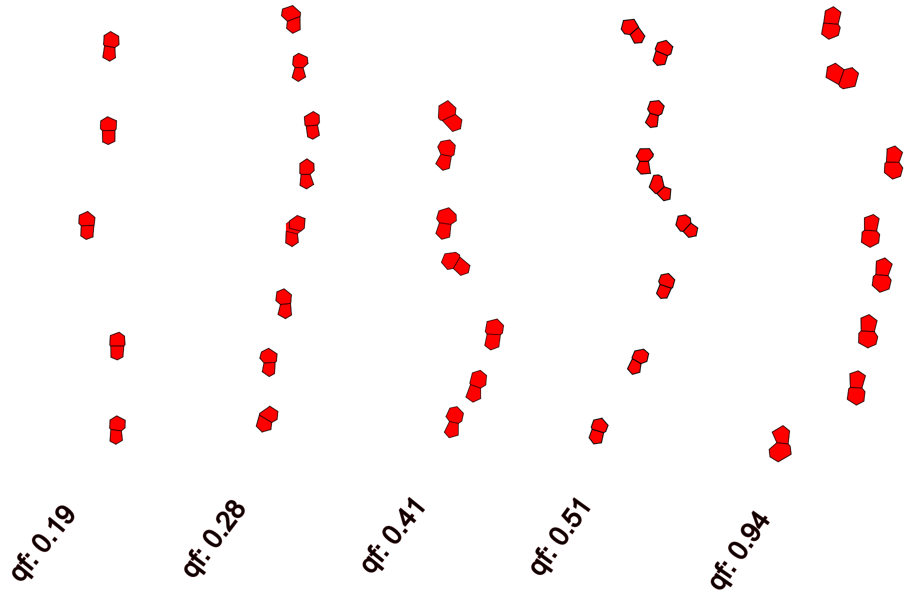

Figure 4.12: Attribution of a quality factor qf for the the extracted defect pair strings based on how straight the lines are and angles between pairs of defect pairs. The lower the better. Reproduced from the author's published work [50].

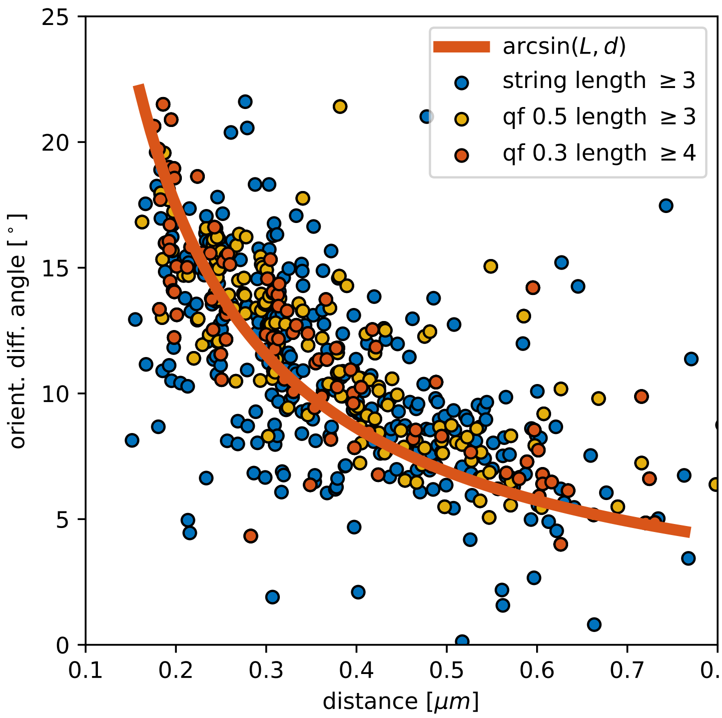

Figure 4.13: Comparing the difference in orientation versus median distance in the corresponding strings of different minimum lengths and quality factors.

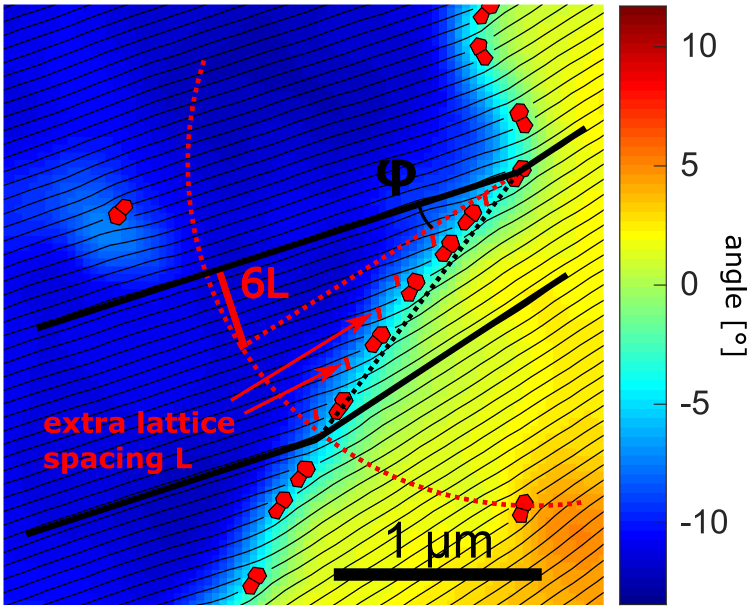

Figure 4.14: Illustration of the lattice splitting by a string of defects. The six defects in the string each add a lattice spacing L, causing a lattice splitting at an angle ϕ. Reproduced from the author's published work [50].

would follow an arcsin-relation between the relative angle of adjacent domains (ϕ) and the ratio of the lattice constant L and the median distance between dislocations D:

$$\phi = \arcsin\left(\frac{L}{D}\right),$$

where $6L/6D = L/D$ is used in the illustration. This relation is shown as the orange curve in figure 4.13 and we can see a very good agreement with our observations.

Recently, a study with a similar result has been published [70]. However, here we focus in more detail on the algorithm that we use to extract and quantify the dislocation lines. Furthermore, in contrast to [70] where the authors mention their algorithm fails to extract dislocation lines separating domains with a relative angle below 10 degrees, our algorithm does so just fine and lines can be extracted for the whole spectrum of observed twisting angles without the need for manual corrections. We used one minor simplification which is to discard all non-paired defects, i.e. clusters of higher order. Our analysis could therefore be further refined by calculating the Burgers vector for these defect clusters to determine to what extent they behave as dislocations or not. Essentially though, discarding such clusters means producing a gap in a string of dislocations so that in such an instance one would consider two strings of dislocations instead of one. In practice this means that the elimination of defect clusters has only a limited impact on our results.

4.7 Visualisation of Grains and Grain Boundaries

As we have established above, strings of dislocations separate crystalline grains with different orientations. We present in the following a robust method to extract and visualise these grains as well as their boundaries. This analysis will also be very useful in chapter six, where we study dynamically evolving skyrmion configurations out of equilibrium. Basically, we can see from the angle map displayed in figure 4.8 that there are around six distinguishable domains. We define points to be part of a single domain if they have the same angle and are locally well ordered. We therefore introduce an order parameter describing the local orientation of any given point that will also be used in the following chapters. It is based on the bond orientation between sites of nearest neighbours [71]

$$\psi_6(\boldsymbol{r}_i) = \frac{1}{N_{nn}} \sum_{j=1}^{N_{nn}} e^{i6\theta_{ij}}, \tag{4.1}$$

with N_{nn} the number of nearest neighbours of a given particle at site $\boldsymbol{r}_i$ as yielded by Delaunay triangulation and θ_{ij} the angle between the bond between the particles at $\boldsymbol{r}_i$ and $\boldsymbol{r}_j$ and a fixed axis. The absolute value of this complex parameter will be large when a point is sixfold-coordinated and the angles of the triangles connecting it to its nearest neighbours are close to $60°$. Conversely, a defect site will therefore take on a low value. This complex order parameter can furthermore be used to define an angle between $0°$ and $360°$. In real space this corresponds to a range of $0°$ to $60°$ since hexagons are congruent after turning $60°$. The corresponding map is displayed in figure 4.15. Individual skyrmions can be considered to be part of a certain domain if the following conditions are met:

1. The phase angle $\theta_6(\boldsymbol{r})$ between two neighbouring sites i and j is binned at a distance of $36°$ corresponding to $6°$ in real space; Due to the binning, points that should belong to the same domain are split into two bins. If after the binning the difference of the average angle of these points is below a certain threshold, they shall be put into the same bin
2. The magnitude $|\psi_6(\boldsymbol{r})|$ is larger than 0.6 for neighbouring sites [72]
3. The bond length deviation between neighbouring sites is less than 10% of the average particle distance [72]

This is a standard problem in graph theory. In mathematics, a graph can be both a function plot, but also an object that more commonly can be referred to as a network. It consists of nodes or vertices that may or may not be connected by edges and therefore serves as a representation of pairwise relations between different elements. A schematic example is depicted in figure 4.17. We can make use of graphs to provide us information on how each skyrmion position is related to a neighbouring position in terms of its orientation and local order parameter. A first graph can be constructed based on the Delaunay triangulation, meaning that each point is related to all other points since all points are connected. This

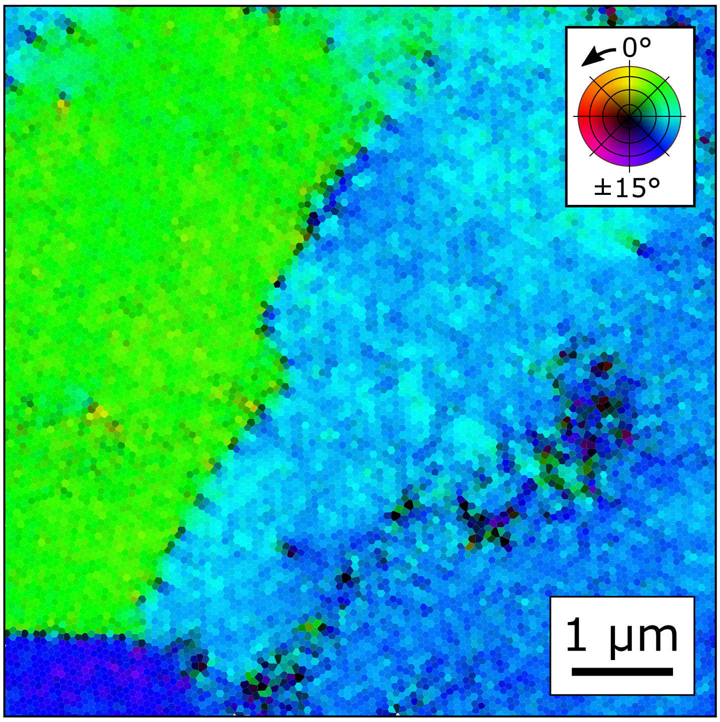

Figure 4.15: Map of the order parameter ψ_6 (equation 4.1) in hsv (hue, saturation, value) colour space. The complex values are used to calculate the angle map (hue), the absolute value $|\psi_6|$ provides information on the quality of local order (value).

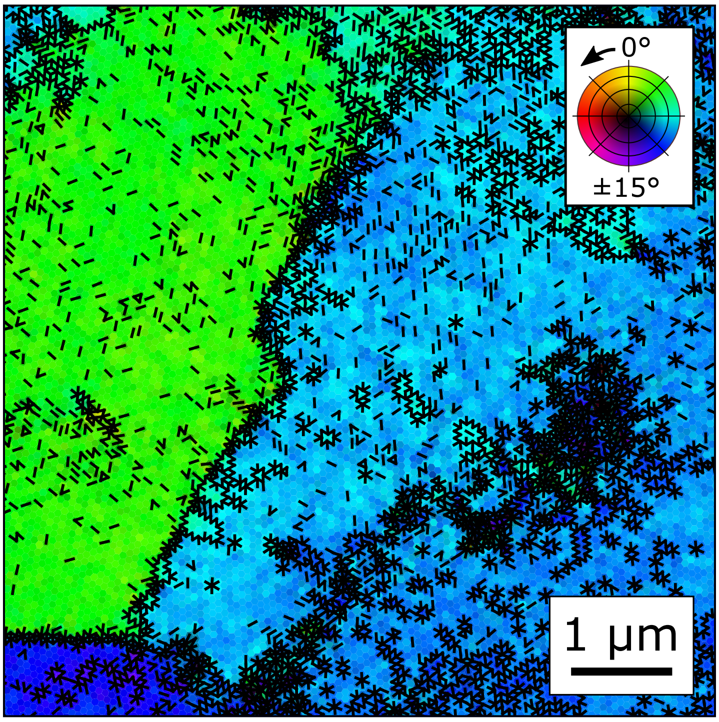

Figure 4.16: Black lines mark pairs of points between which the connections in the single adjacency graph are broken according to the criteria specified in the text.

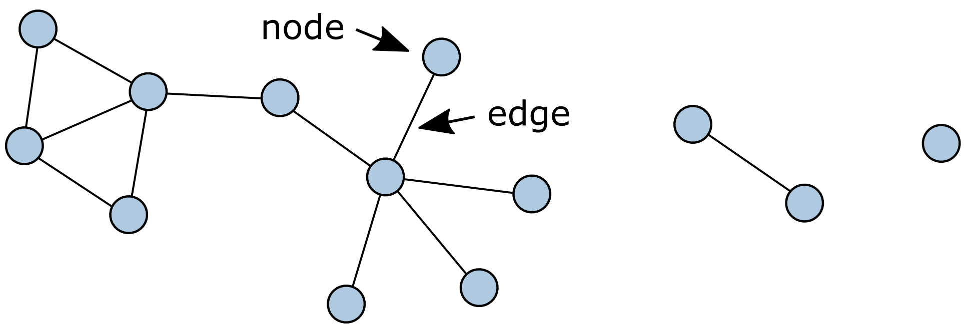

Figure 4.17: A graph as a network of nodes connected by edges, which describe the pairwise relations between points.

leads to the graph displayed in figure 4.18. There are different visual representations of such a graph (one would be simply the Delaunay triangulation). Here we choose a representation where the position of the graph nodes are calculated based on the structure of the graph, i.e. how close points are to each other and how many neighbours they have. The connections in this single adjacency region are then broken according to the three conditions above. This is illustrated in figure 4.16. The black lines indicate the rupture of a connection of a pair of points as specified by these criteria. Doing so for all sites breaks the single adjacency region into multiple adjacency regions that can be identified as a symmetry breaking domain. Figure 4.19 shows the multiple adjacency regions as a graph plot (subgraphs of the original graph) as a result of cutting the connections.

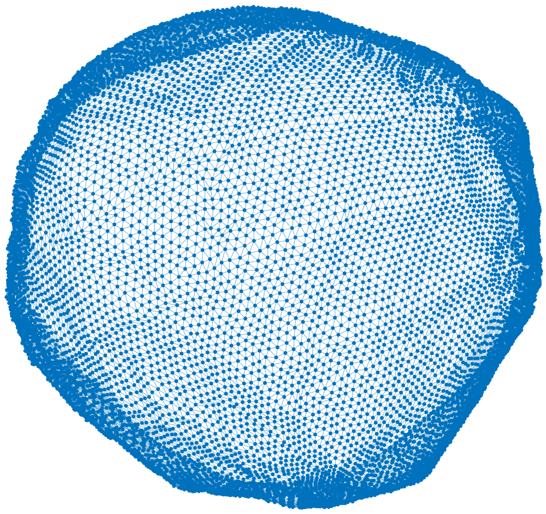

Figure 4.18: Graph representation of the single adjacency region based on the Delaunay triangulation.

Figure 4.19: Graph representation of the multiple adjacency regions as a result of cutting the connections of the first graph.

The indices in the subgraph can be used to color the points accordingly, as depicted in figure 4.20. Coloured points belong to a domain, empty circles are points that do not belong to any

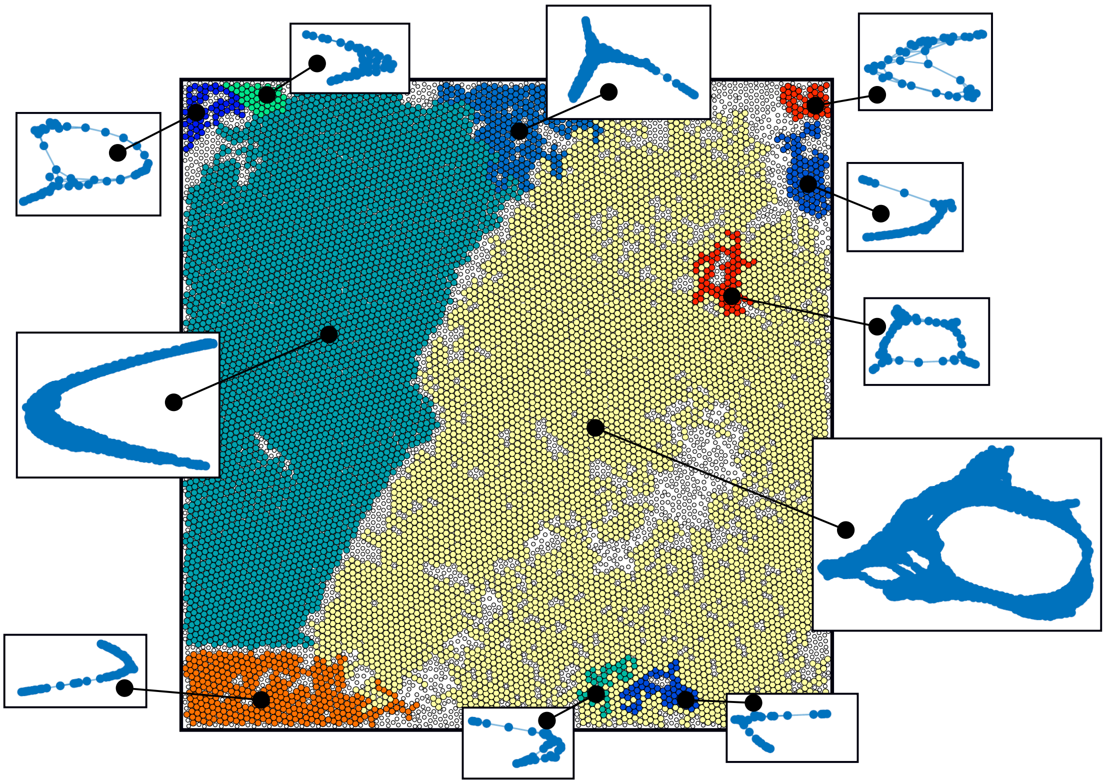

Figure 4.20: The resulting domain identification based on the obtained graphs. For illustration each domain is shown along with its corresponding graph.

domain or that belong to domains below the chosen threshold size. Here, the minimum size is chosen to be 19 points, which is the number of nearest and second nearest neighbours of and including any given point in a perfect hexagonal arrangement. This way we have successfully extracted the domains for this particular skyrmion configuration. We can use this to further investigate the nature of the grain boundaries separating these domains. For this purpose we construct another Delaunay triangulation, but this time using only the points that are part of a domain, following a procedure outlined in [73]. The result is depicted in figure 4.21.

The characteristic of this triangulation is that each point at the boundary of a domain is connected to two points of another domain or is itself one of those two points. This can be used to find connector lines (red lines in figure 4.21) and to construct the domain boundary by connecting their midpoints as illustrated in the inset of figure 4.21 yielding the blue lines. We can furthermore color these boundaries according to the angle that separates the corresponding domains, as shown in figure 4.23. Compare this to the defect structure displayed in figure 4.22. This method provides information about the type of grain boundary: small angle grain boundaries (SAGB) and large angle grain boundaries (LAGB). We can see that SAGBs do not necessarily need defects to be accommodated. Figure 4.24 illustrates the changes in the domain boundary configurations and their angles across the sequence of images of the TEM series studied here.

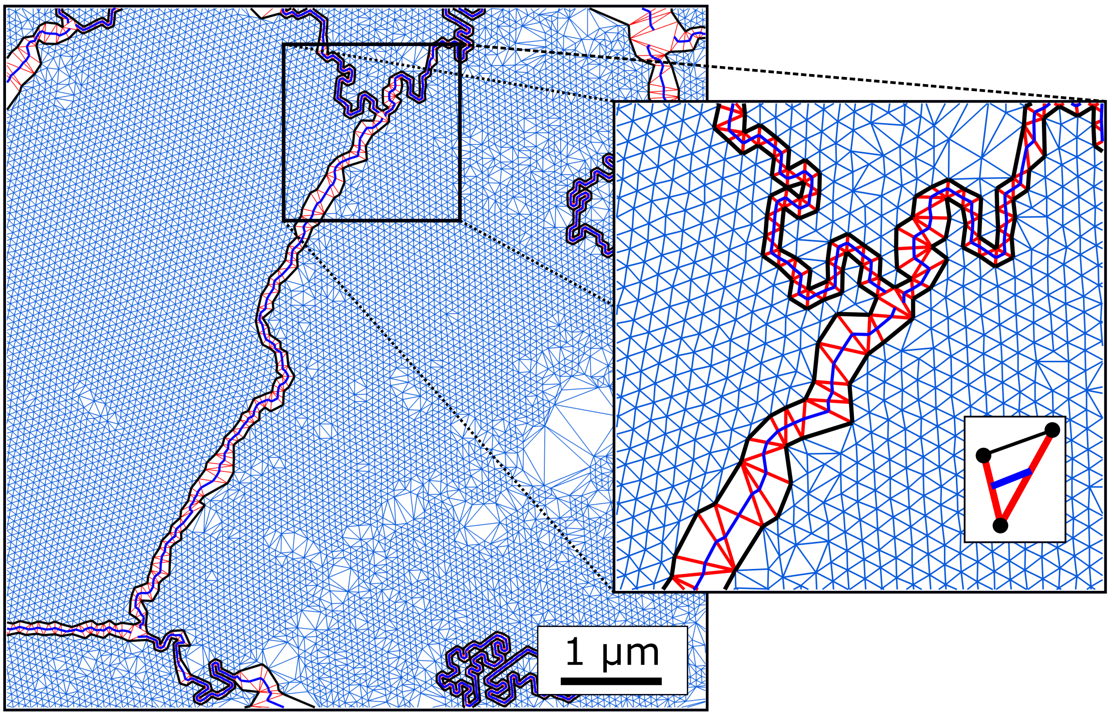

Figure 4.21: Delaunay triangulation based on the points that are part of a domain. The connectors between domains (red) are used to calculate the grain boundary, as illustrated in the inset.

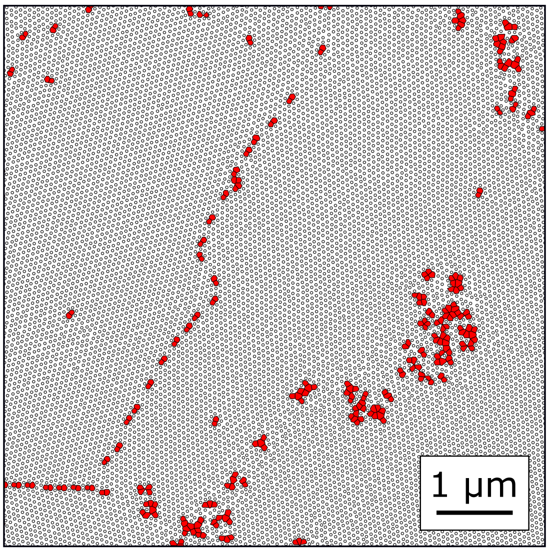

Figure 4.22: Defect structure of this particular skyrmion configuration (frame 150).

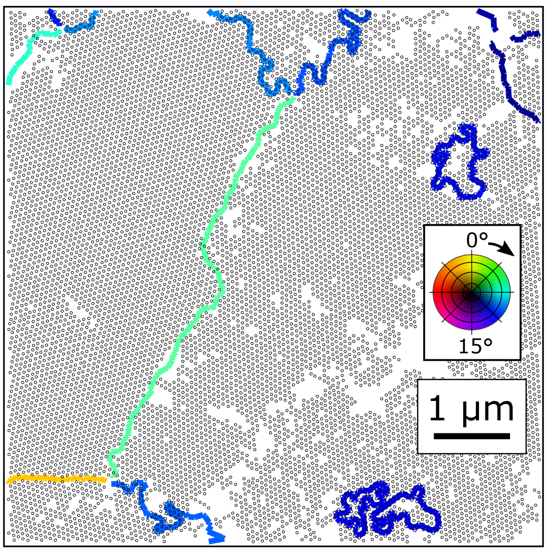

Figure 4.23: Extracted domain boundaries. The colour code corresponds to the separation angle between adjacent domains.

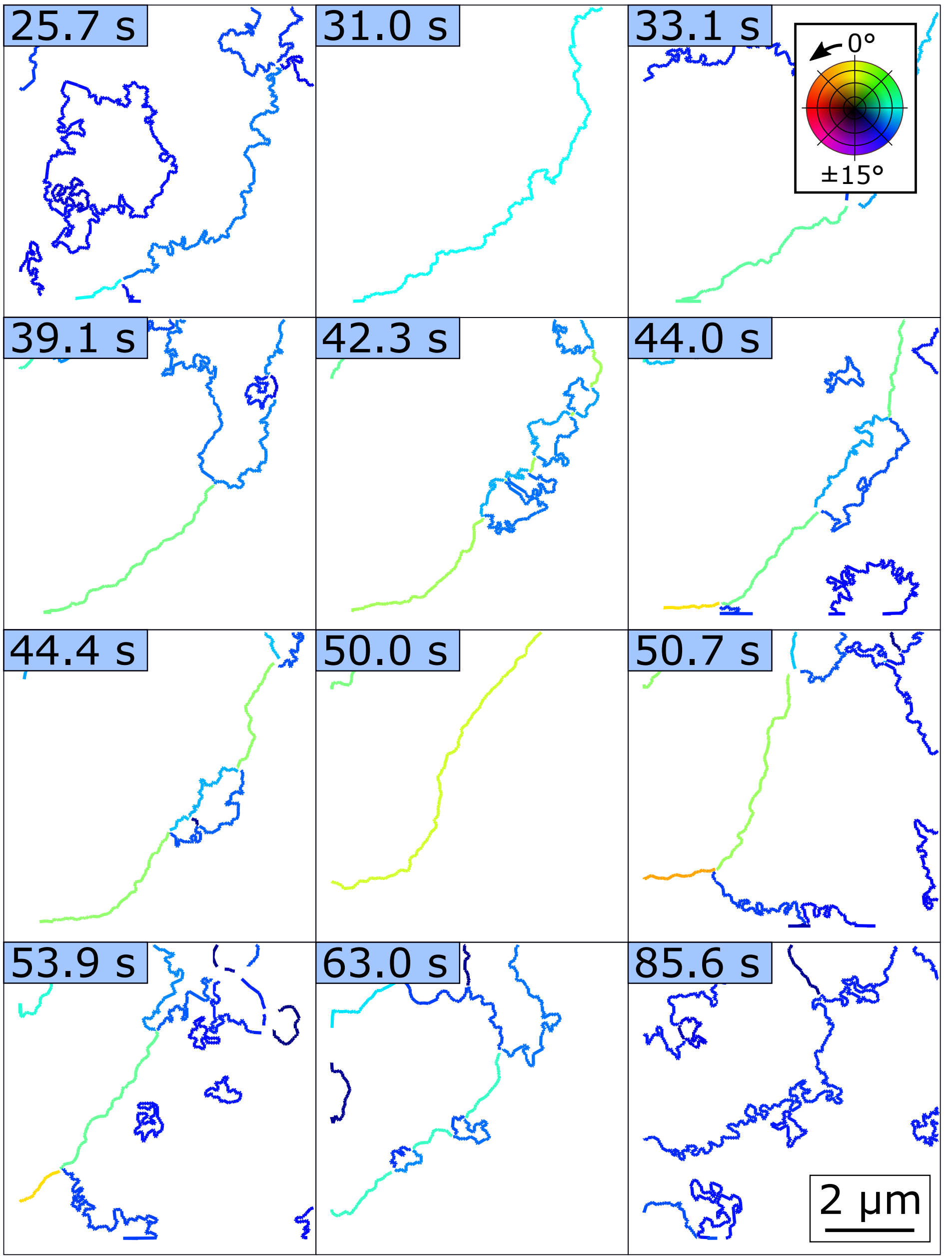

Figure 4.24: Overview of the evolution of the grain boundary structure for a few selected frames at a given time of the movie.

4.8 Conclusion

In summary, we have developed an algorithm, which can extract lines of dislocations that separate adjacent domains of different orientations and classify them into substrings of different quality. With this kind of statistical probing of grain boundaries, we achieve the equivalent of systematically generating grain boundaries separating domains with gradually decreasing dislocation density. The resulting relationship between the median distance between dislocations and the relative angle between domains is a geometrical one: for a given twisting angle the average distance from one dislocation to the next is determined by the lattice spacing a and therefore follows an arcsin relation. We present to our knowledge the first automated and reliable extraction of low-angle grain boundaries in skyrmion lattices (in the only other similar study manual corrections were necessary for low angles [70]). We furthermore present a method to reliably extract the different grains for a given skyrmion configuration based on graph theory. This can be further used to extract and visualise the grain boundary structure.

Research in grain boundaries is still a very active subject in material science and only recently for example, direct evidence for grain boundary migration has been found using atomic resolution scanning transmission electron microscopy (STEM) [74]. Another example are the recent results on grain boundary phase transformations in a metal using high resolution electron microscopy (HRTEM) [75]. These dynamic experiments are very tricky to perform on an atomic level. While STEM is great to image static atomic structures, the temporal resolution is poor. HRTEM offers much better temporal resolution but the interpretation of the images is challenging [74]. We show how the dynamical properties of skyrmion lattices and their observation in real space and real time by LTEM qualify skyrmion systems as testbeds for other condensed matter systems where real space observations are either not possible or similar statistics are not achievable. This paves the road for further investigations, in particular, the real time dynamics of grain boundary movement. Dr. Daniele Mari pointed out in discussions that in classical crystals the driving force for grain boundary movement which leads to recrystallisation is the amount of disorder and especially the amount of dislocations. This creates a huge elastic energy that will be relaxed by dislocation mobility which leads to grain boundary mobility. Hence one could investigate whether the grain boundary mobility depends on the dislocation density or grain boundary angle. Magnons are known to be created in thermal gradients (such as by electron beam irradiation in the TEM) and induce skyrmion movement such as the ratchet motion described in [70]. Gradients of magnetic fields have also been found to induce magnon currents that can efficiently drive skyrmions [76]. Therefore, one could think to replicate the shear force in real crystals that drive dislocations and grain boundary movement by magnon currents in skyrmion lattices.

5 Melting of Skyrmion Lattices

After studying defects at grain boundaries in the previous chapter, we take a deep dive into their role in mediating the melting process in skyrmion lattices. Although melting is one of the most common phase transitions observed in nature we still lack a microscopic melting theory in three dimensions. It is fact much better understood in two dimensions and microscopic theories actually do exist, most prominently the theory developed by Kosterlitz, Thouless, Halperin, Nelson and Young (KTHNY) in the 1970s. It describes melting in two dimensions as a two stage process mediated by the formation and unbinding of topological defects. The skyrmion lattices we study here can be treated as essentially two dimensional and we will show that they melt in a two step process as described by the KTHNY theory. In this study, we demonstrate by cryo-Lorentz transmission electron microscopy that by a controlled magnetic field ramp we can induce the phase transition in skyrmion lattices in the skyrmion host Cu_2OSeO_3 from the skyrmion solid to the skyrmion liquid phase and reveal the existence of an intermediate oriented liquid phase, the so called hexatic skyrmion phase. Our experiments show that skyrmion lattices as lattices of quasiparticles behave like lattices of ordinary particles, which further advances our understanding of the nature of skyrmions - between their description within the wave and particle picture [1].

5.1 Melting in 2D

Phase transitions are most often linked to a break of symmetry or order, for instance the transition from the paramagnetic to the ferromagnetic state, when the the rotational symmetry in the paramagnetic phase is broken in favour of a parallel alignment of spins. Or when a fluid crystallises into a solid and the translational and orientational symmetries are replaced by discrete symmetries. Generally, the high symmetry phase is a high temperature phase (e.g. liquid) and the low symmetry phase a low temperature phase (e.g. crystalline). However, the general concept of symmetries does not explain the mechanisms on a microscopic scale that are responsible for the breaking of these symmetries. Especially the 3D case is still poorly

[1] The results of this chapter are published in [64]

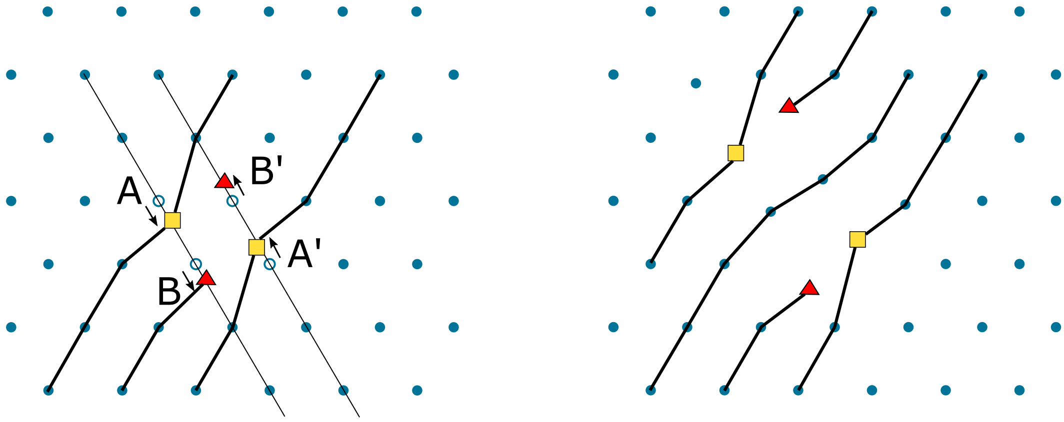

(a) Emergence of a dislocation pair

(b) Separate dislocations

Figure 5.1: A dislocation pair is created by a coordinated shift in positions (a). This pair can be separated upon thermal excitation into two dislocations (b).

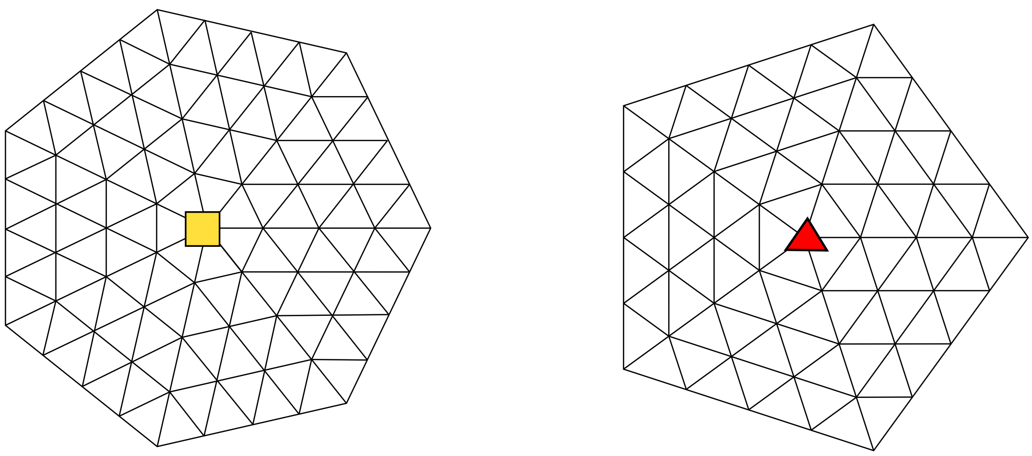

(a) 7-defect

(b) 5-defect

Figure 5.2: Separation of dislocations into unbound defects: dislocations. 7-defect (a), 5-defect (b).

understood to date due to the enormous amount of particles (10^{25} in one litre of water) involved in the computation of the properties of matter [61]. The situation in 2D is different in that no true long range order exists due to long wavelength fluctuations, as argued by Peierls in 1935 an later generalised by Mermin and Wagner [61, 77, 78]. Nevertheless, quasi-long range order does exist as do transitions from topologically unordered to topologically ordered phases. They differ with respect to their density of topological defects (high in the unordered phase, low in the ordered one) and can be distinguished by determining elastic moduli which disappear in the ordered phase [61, 79, 80]. Thermal excitations dissociate bound topological defect pairs and lead to the Berezinskii-Kosterlitz-Thouless transitions in the 2D XY model [79, 81, 82, 83]. Similarly for melting of crystals in 2D, the KTHNY theory [79, 84, 71, 85] is among the most successful ones to explain melting to be driven by the emergence of topological defects: thermally activated dislocation pairs that in a first step dissociate into free dislocations and then in a second step dissociate into unbound defects called disclinations. A dislocation in a two dimensional crystal originates from the insertion of a half lattice line. As a result, there is no way to get rid off a single dislocation by any continuous transformation and such a defect is hence called topological (see also chapter four). The way dislocations emerge is schematically illustrated in figure 5.1 (a). They do not emerge individually but rather in pairs [61]. The particles at position A and B are moved by a small distance along a lattice direction. At the same time, positions A' and B' are moved by the same distance in the other direction. By means of a Voronoi construction (see chapter four) one can show that by this coordinated shift of positions A and A' have become seven-fold coordinated sites ('7-defect') and B and B' five-fold coordinated site ('5 defect'). A 5-defect and an adjacent 7-defect form a dislocation. In this case, we have two adjacent dislocations, a dislocation pair. When agitated by thermal fluctuations, such a pair can split into two separate dislocations as shown in figure 5.1 (b). We can see how this leads to the insertion of two lattice half-lines (ending at the 5-defect). If more energy is provided, the pair can fully dissociate into individual unbound defects or disclinations, as depicted in figure 5.2. One can see how much a lattice needs to be distorted to accommodate this type of defect.

Specifically for the process of melting this means that at first the quasi-long range translational order is broken (dissociation of dislocation pairs) while a quasi-long range orientational order - the so called hexatic phase - is maintained. The correlation functions in this phase decay algebraically. In a second step, the orientational order is broken in favour of a high symmetry phase (dissociation of some of the free dislocations) and the correlation functions decay exponentially. This state is characterised by short range translational and orientational order like an isotropic liquid [61].

All real-space experiments on the 2D melting have thus far been carried out on real-matter particles like electrons [86], molecules and colloids [87, 88, 89, 90, 91]. But quasi-particles such as skyrmions can also form 2D crystal structures [46, 37]. We will show in the following that as matter of fact, the concept of 2D melting as described by the KTHNY theory also holds for skyrmion lattices.

5.2 Experimental Details

TEM lamellas of Cu_2OSeO_3 along the [111] direction were fabricated using the FIB as described in chapter two. We aimed for a large lateral size of the thinned down area of $15\,\mu\mathrm{m} - 20\,\mu\mathrm{m}$, as shown in figure 5.3 to allow to host a large number of skyrmions. The thickness was chosen to be around 150 nm. This is much smaller than the ≈ 700 nm longitudinal correlation length of skyrmion lattices in Cu_2OSeO_3 as obtained by small-angle-neutron-scattering (SANS)

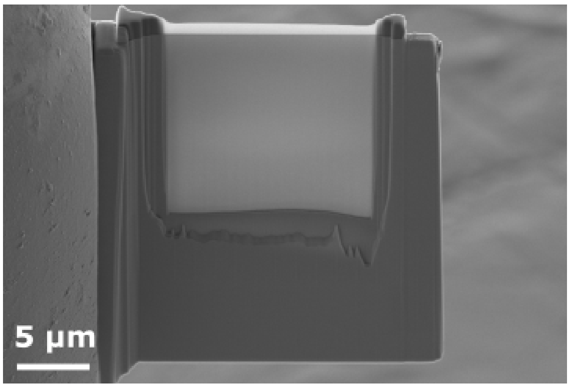

Figure 5.3: SEM image of the TEM lamella used for the experiments.

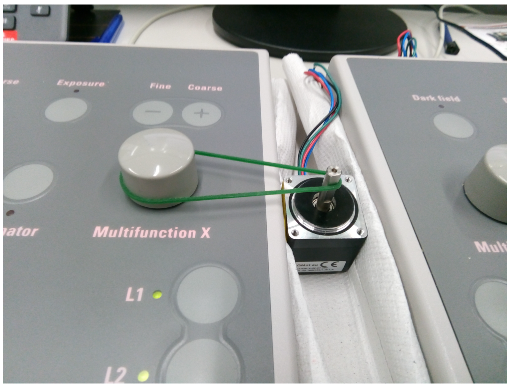

Figure 5.4: Stepper motor with rubber band turns the magnetic field control knob.

[7, 92, 30, 93]. Therefore, we can expect the system to be essentially two dimensional. Our experiments were carried out on an FEI Titan Themis transmission electron microscope (TEM) in Lorentz mode. A Gatan liquid helium TEM sample holder was used to cool the sample down to below the magnetic ordering temperature of Cu_2OSeO_3 (60 K). During the whole melting process, the sample temperature was maintained constant. Magnetic field was applied via the main objective lens of the TEM, and the direction of the magnetic field was perpendicular to the sample plane. LTEM movies were acquired simultaneously while slowly ramping the magnetic field so that the whole melting processes was recorded in real space and real time. LTEM movies were acquired at frame intervals of 200 ms to 300 ms, at constant temperatures varying from 12 K to 42 K, and usually contain hundreds to more than one thousand frames. Additional movies were recorded at different beam intensities to rule out potential heating effects and at selected constant fields to verify equilibrium conditions and extract the time dependence of correlation functions. Since the microscope user interface does not allow to perform a controlled magnetic field ramp, a stepper motor with rubber band transmission was connected to the knob on the microscope control panel controlling the objective lens excitation, as shown in figure 5.4. The field increase is linear and various ramp rates can be achieved. After acquisition, each frame can then be assigned to a field value.

For clarity we will focus on a series acquired at a magnetic field ramping rate of 2 Oe/s, an electron beam intensity of 0.23 kA/m^2, and containing more than 1400 frames with an acquisition time of 200 ms. Note that over 30,000 skyrmions can be recorded in a single LTEM image/movie frame, see figure 5.5.

5.3 Two-Step Melting Process

We will show in the following how skyrmion lattices melt in a defect-mediated two-step melting process. We can get a first qualitative insight by a visual inspection of TEM images, their Fourier transforms and the corresponding Voronoi tessellation. The latter is a geometric

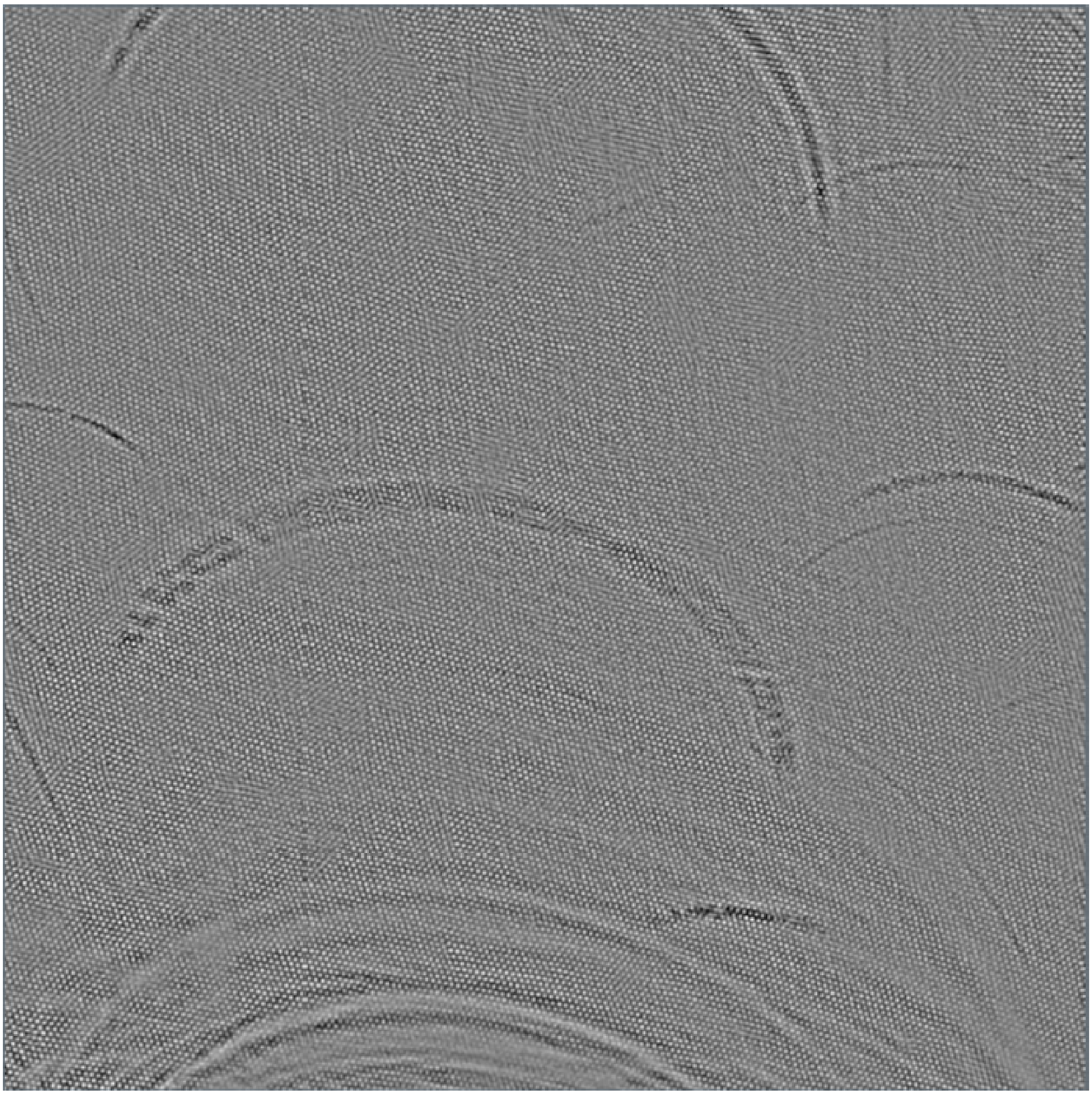

Figure 5.5: Real space image (after filtering) of an area containing more than 30,000 skyrmions. Figure reproduced from the author's published work [64].

construction based on the extracted skyrmion positions such that each point within the resulting polygons is closer to the respective skyrmion position than any other position, see chapter four for more details. The number of edges of such a polygon is therefore equivalent to the number of nearest neighbours of a skyrmion. Figure 5.6 shows LTEM images acquired at different magnetic field strengths, from low to high along with their FFT. They represent three distinct types of skyrmion configurations. At low magnetic fields (H = 667 Oe, panel a), skyrmions arrange in the well known hexagonal lattice [7] that is also clearly identifiable by the six sharp Bragg peaks from its FFT similar to the small angle neutron scattering (SANS) patterns reported in literature [7, 93]. We can see this as well in the corresponding Voronoi diagram, with almost all sites

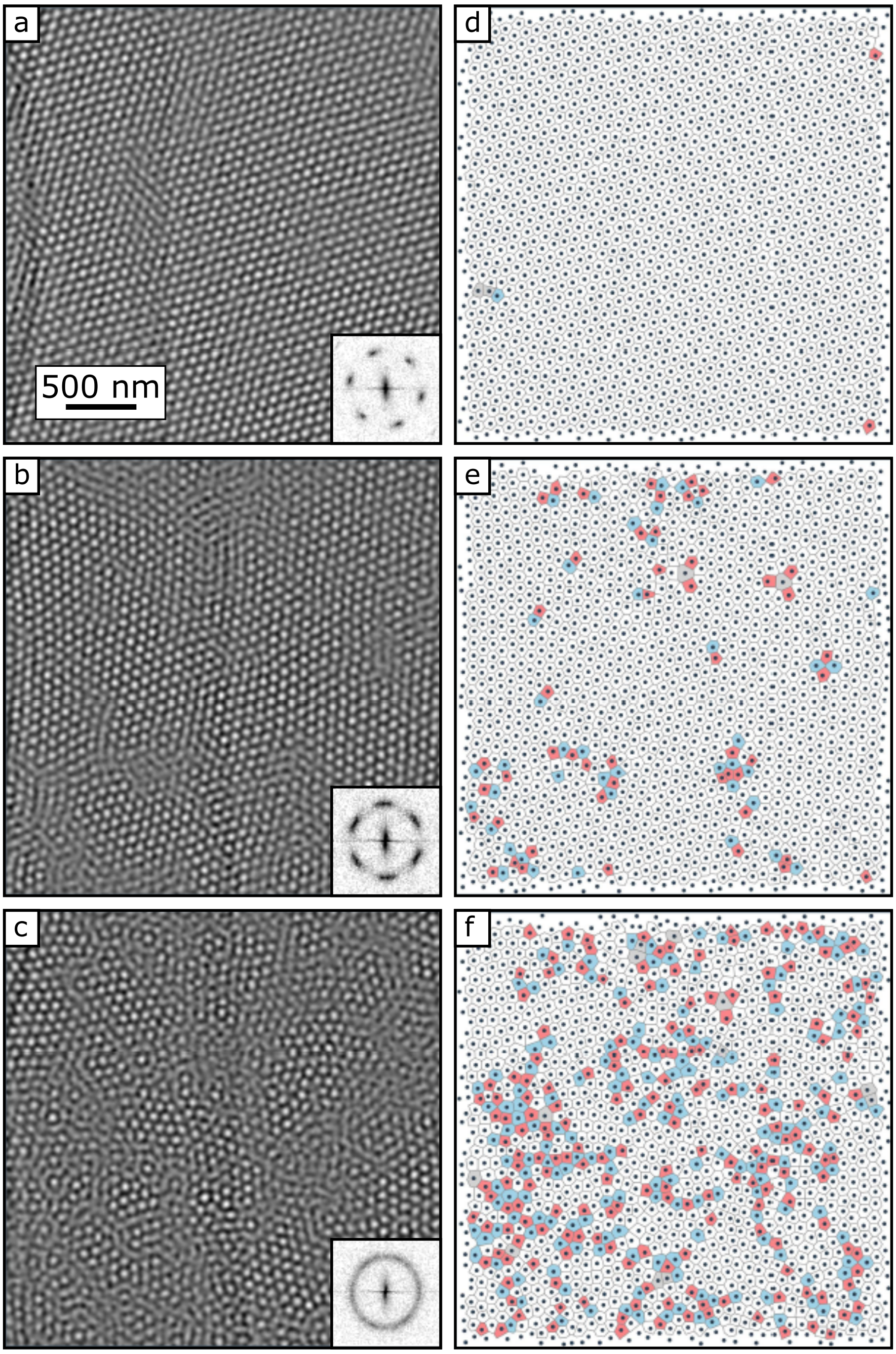

Figure 5.6: Real space images and topology analysis for the SkL melting process. Real space LTEM images at T = 22 K and magnetic field H = 667 Oe (a), H = 1108 Oe (b) and H = 1203 Oe (c). Inserts show FFT. Black dots are skyrmion positions (d-f) identified in real space images (a-c). Voronoi tessellation provides information about nearest neighbours. White polygons are 6-fold coordinated sites, blue polygons are 7-fold coordinated sites, red polygons 5-fold coordinated sites and gray polygons all other sites. Figure reproduced from the author's published work [64].

being sixfold coordinated (white polygons). The sharp Fourier peaks start to broaden at higher magnetic fields and form arcs before they transform into a full ring at high magnetic fields when the skyrmions reach the isotropic state. In the corresponding Voronoi diagram this behaviour manifests first in the appearance and increasing number of dislocations. These are pairs of adjacent defects, usually a pair of 5-fold and 7-fold coordinated sites (red and blue polygons). In the isotropic phase the number of dislocations further increases along with the appearance of disclinations, individual 5- or 7-defects that result from the dissociation of dislocations.

5.4 Translational Correlation Order

In the KTHNY melting scenario the quasi long range translational order and long range orientational order evolve separately as a result of the dissociation of dislocation and disclination pairs, which allows to distinguish three distinct phases: the solid phase, the hexatic phase (dissociation of dislocation pairs) and the liquid phase (dissociation of disclination pairs). We study these transitions quantitatively by analysing the evolution of the translational and orientational order. A common local translational order parameter $\psi_{ql}(\boldsymbol{r})$ is defined by [94]

$$\psi_{ql}(\boldsymbol{r}) = e^{-i\boldsymbol{q}_l\boldsymbol{r}}, \tag{5.1}$$

with $\boldsymbol{r}$ being the skyrmion positions and $\boldsymbol{q}_l$ with $l = 1,2,3,4,5,6$ the reciprocal lattice vectors extracted from the positions of the first-order Bragg peak of the structure factor $S_q(\boldsymbol{q})$. The structure factor can be derived from the pair distribution function $G_r(\boldsymbol{r})$:

$$G_r(\boldsymbol{r}) = \frac{1}{N}\sum_{\langle i,j\rangle}\delta(\boldsymbol{r}-\boldsymbol{r}_{ij}), \tag{5.2}$$

with the sum over all pairs i, j, $\boldsymbol{r}$ being a real space vector, $\boldsymbol{r}_{i,j}$ the displacement vector between skyrmions i and j and N the number of skyrmions. The structure factor is defined using $G_r(\boldsymbol{r})$ as

$$S_q(\boldsymbol{q}) = \sum_{\boldsymbol{r}} e^{-i\boldsymbol{q}\boldsymbol{r}} G_r(\boldsymbol{r}), \tag{5.3}$$

with $\boldsymbol{q}$ being a reciprocal space vector. The peak positions of $\boldsymbol{q}_l$ are determined by fitting 2D Gaussians. The translational correlation function $G_k(r)$ is then defined as

$$G_k(r) = \frac{1}{6}\sum_{l=1}^{6}\frac{1}{N_r}\sum_{\langle i,j\rangle}^{N_r}\psi_{q_l}(\boldsymbol{r}_i)\psi^*_{q_l}(\boldsymbol{r}_i), \tag{5.4}$$

with the average over $l = 6$ reciprocal lattice vectors and N_r skyrmions separated by a distance r. The correlation functions $G_k(r)$ shown in figure 5.7 are calculated for various magnetic fields along with their fits using either a power law or exponential decay.

Power law decays $G_k(r) \propto r^{\eta_k}$ can be fitted to the upper envelopes of $G_k(r)$ at low fields

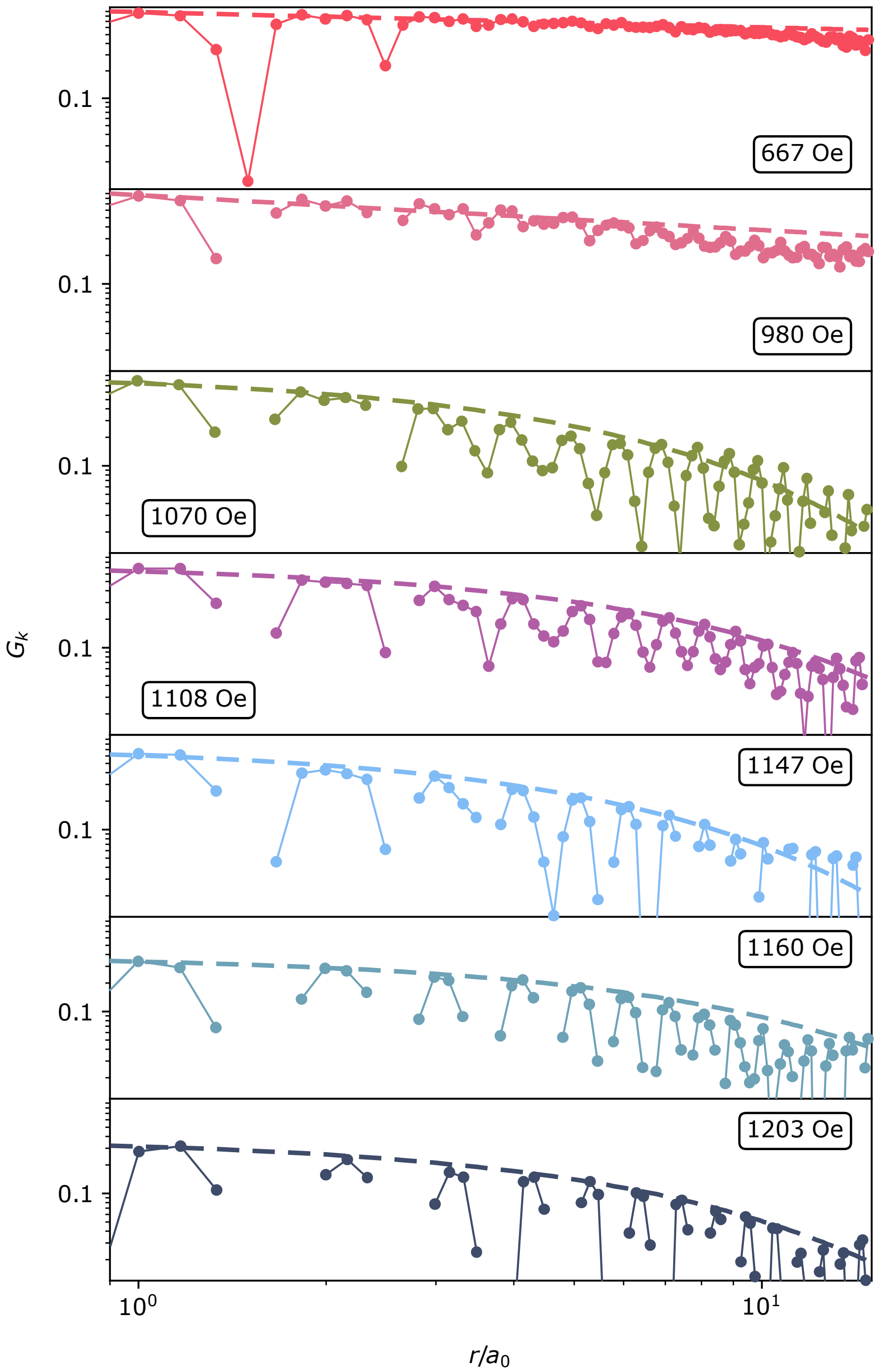

Figure 5.7: Translational correlation function of skyrmion lattices at different magnetic fields. Power law decays (straight lines in log-log plot) and expontential decays are fitted to the upper envelope of the correlation function. Figure reproduced from the author's published work [64].

$H = 667$ Oe and $H = 980$ Oe with the critical exponent η_k being below the critical value of 1/3 predicted for the solid to hexatic transition [95, 96] whereas the $G_k(r)$ at higher fields need to be fitted to exponential decays, see figure 5.7. The latter indicate a much faster decay and loss of translational order whereas the power law decays are slow and do not have a characteristic decay time.

5.5 Orientational Correlation Order

The second step in the melting scenario results from the dissociation of dislocations into disclinations, which break the long range orientational order of the hexatic phase. A suitable local orientational order parameter can be defined by the bond orientation between sites of nearest neighbours [71]

$$\psi_6(\boldsymbol{r}_i) = \frac{1}{N_{nn}} \sum_{j=1}^{N_{nn}} e^{i6\theta_{ij}}, \tag{5.5}$$

with N_{nn} the number of nearest neighbours of a given particle at site $\boldsymbol{r}_i$ as yielded by Delaunay triangulation and θ_{ij} the angle between the bond between the particles at $\boldsymbol{r}_i$ and $\boldsymbol{r}_j$ and a fixed axis (see figure 5.8 C). The orientational correlation function is then given by

$$G_6(r) = \frac{1}{N_r} \sum_{\langle i,j \rangle}^{N_r} \psi_6(\boldsymbol{r}_i)\psi_6^*(\boldsymbol{r}_j), \tag{5.6}$$

with N_r being the number of particles at distance r from each other. Figure 5.8 A shows $G_6(r)$ for a range of magnetic fields along with fits to their upper envelope following either a power law or exponential decay. For the two lowest magnetic fields represented here ($H = 667$ Oe and $H = 980$ Oe) $G_6(r)$ remains almost 1 and constant in agreement with the KTHNY prediction for the solid phase. For higher fields (until $H = 1147$ Oe) $G_6(r)$ decreases algebraically (linear decrease in the log-log plot). As a reference, the critical KTHNY decay exponent of $\eta_6 = 1/4$ is added as a solid green line in the plot. For higher magnetic fields ($H = 1160$ Oe and $H = 1203$ Oe) the decay is exponential thus fully breaking the orientational order. This characterises the liquid phase where both translational and orientational order give way to the high symmetry liquid phase.

Moreover, temporal correlations of the local order parameter $\psi_6(\boldsymbol{r}, t)$ can further confirm the trends that we obtain using spatial correlation functions. The temporal correlation function is defined as:

$$G_6(t) = \langle \psi_6(\boldsymbol{r}, \tau)\psi_6^*(\boldsymbol{r}, t+\tau)\rangle_{\tau,\boldsymbol{r}}, \tag{5.7}$$

with the averages taken over times τ and skyrmion positions $\boldsymbol{r}$. $G_6(t)$ calculated for three movies acquired at 28 K at constant magnetic fields is shown in figure 5.8 B. We notice three distinct behaviours, corresponding each to the solid, hexatic and liquid phase, respectively. For low magnetic fields ($H = 571$ Oe) $G_6(t)$ remains constant and close to 1, for the intermediate field ($H = 982$ Oe) the decay follows a power law, $G_6(t) \propto t^{-\eta_6/2}$ indicative of the hexatic phase

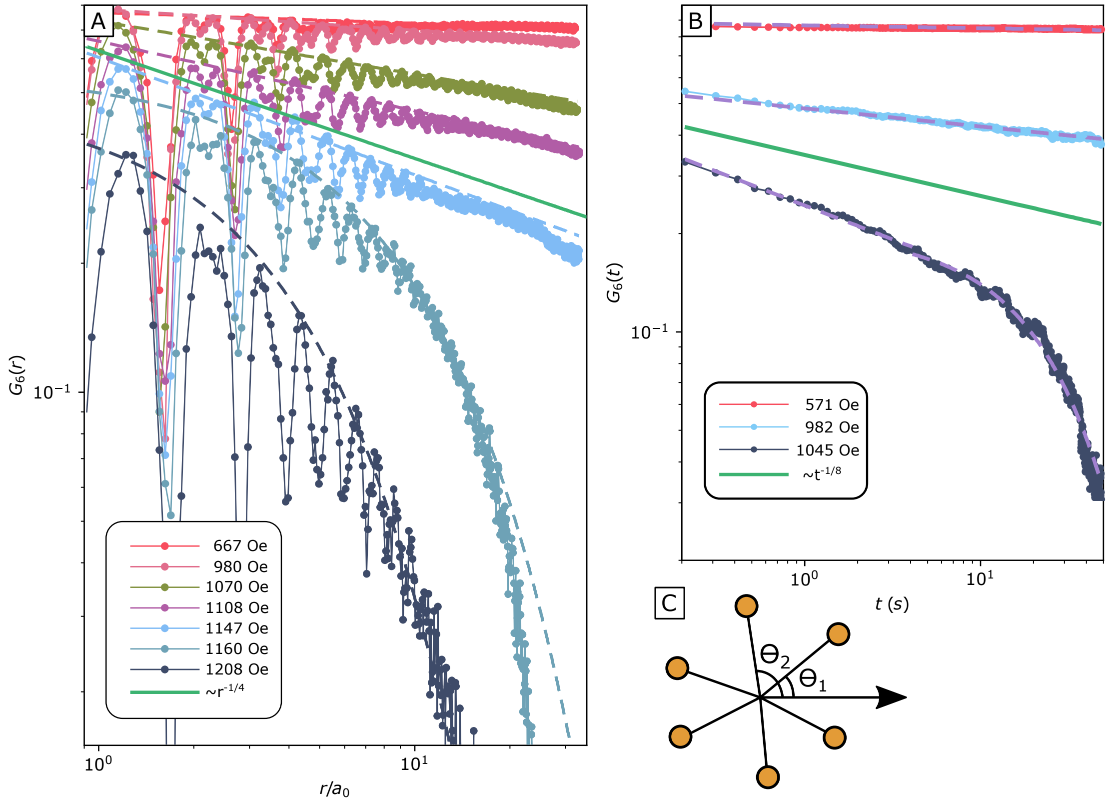

Figure 5.8: Orientational order of the skyrmion lattice at different magnetic fields for the series acquired at $T = 22\,\text{K}$. The spatial orientational correlation function $G_6(r)$ along with either algebraic or exponential decays (dashed lines) fitted to the upper envelope (A). The critical KTHNY decay exponent $\eta_6 \to 1/4$ is represented by the green line. The inset (C) illustrates the definition of the orientational order parameters ψ_6. Temporal correlation functions $G_6(t)$ at static fields for a series acquired at $T = 28\,\text{K}$ (B), along with algebraic (solid and hexatic phase) and exponential fits (liquid phase). The critical KTHNY exponent $\eta_6 \to 1/4$ is drawn as a green line. Figure reproduced from the author's published work [64].

[97] and for the highest field ($H = 1045\,\text{Oe}$) the decay is exponential, characteristic for the liquid phase. At the same time, this decay shows that we indeed have a liquid and not a glassy state with frozen disorder, which would not change over time.

5.6 Multiple Observables

We can determine more precisely the actual regions where the transition happens by extracting the decay exponents of the correlation functions for each frame. Figure 5.9 (A) shows the extracted power law decay exponents η_k and η_6 of the translational and orientational correlation function depending on the magnetic field. η_k shows a slow increase till about $H = 1000\,\text{Oe}$ when it jumps to considerably higher values and crosses the critical KTHNY exponent of $\eta_k \to 1/3$. This jump indicates that a power law is no longer a good fit and the

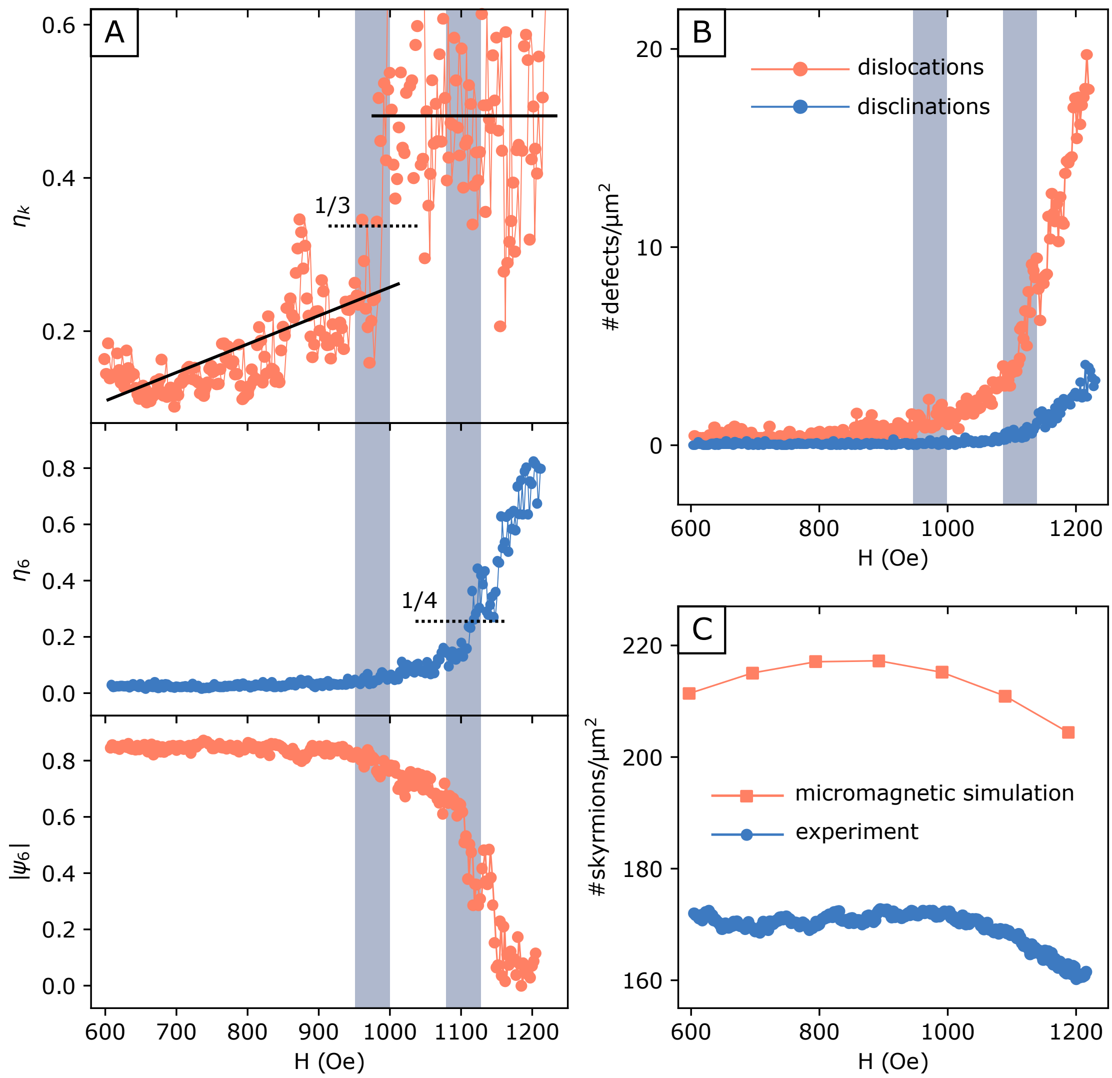

Figure 5.9: Multiple observables as a function of magnetic field. The power law decay exponents η_k for the translational correlation function, η_6 for the orientational correlation function and the average local orientational order parameter $|\psi_6|$ are shown in (A). The lines are guides for the eye. Panel (B) shows the density of disclinations and dislocations as a function of the magnetic field. The shaded areas in (A) and (B) indicate the field range in which the phase transitions happen. In panel (C) the field dependence of the skyrmion density is compared for the experimental and simulated case. Figure reproduced from the author's published work [64].

decay turns in fact exponential. Around the same field η_6 starts to increase well. A constant and almost zero η_6 characterises the solid phase, while the onset of the increase, just as the crossing of η_k of the critical value of 1/3, mark the transition from the solid to the hexatic phase. After η_6 exceeds the critical value of 1/4 at the transition to the liquid, it increases much faster. This is the regime where actually exponential fits are required but the behaviours of η_6 extracted from a power law fit nicely illustrate the onset of the liquid phase. Qualitatively, we find the same two-step behaviour from the averaged local orientational order parameter $|\psi_6| = 1/N \sum_{i=1}^{N} |\psi_6(\boldsymbol{r}_i)|$, which is constant and close to 1 in the solid phase, before it starts to decrease at the onset of the hexatic phase and rapidly shoots down when entering the liquid phase. Both times the transition fields correspond to those where the decay exponents in one of the correlation functions change as well.

We come back to the nature of the KTHNY two step melting scenario that we touched upon at the beginning of this chapter and illustrated in figure 5.6 with the increasing number of defects. The KTHNY theory describes melting in 2D solids as the unbinding of dislocation pairs into free disclocations at the transition from the solid to the hexatic phase (loss of quasi long range translational order) and the unbinding of these dislocations into disclinations when entering the liquid phase (loss of long range orientational order). By counting the number of these two types of defects we can show directly the mechanism of unbinding defects as shown in figure 5.9 (B). The densities of both dislocations and disclinations is vanishingly small before the solid to hexatic transition, which is when the density of dislocations starts to increase while the density of disclinations remains low. The latter starts to increase at the onset of the hexatic to liquid transition. To rule out the possibility that the phase transition is a result of a changing skyrmion density, which is not a conserved quantity, figure 5.9 (C) shows that the skyrmion density remains constant in the solid and hexatic phase before a small drop can be noticed at the transition to the liquid phase. A similar result is obtained from numerical simulations, which can be interpreted as an increasing skyrmion-skyrmion repulsion at higher magnetic fields.

To rule out that any of our observations are the result of non-equilibrium behaviours induced by electron beam irradiation, we acquire multiple melting series at different beam intensities, both higher and lower than that of the series studied in detail above. We extract for each frame the algebraic decay parameter η_6 at the corresponding magnetic field. The results are presented in figure 5.10. We see that the onset of the increase of η_6 and the field value at which the critical value of $\eta_6 = 1/4$ is crossed do not significantly change as a function of beam irradiation on the sample.

Finally, we can use the observables described above, especially the translational and orientational correlation functions to establish the phase diagram of the different skyrmion phases we observe in our experiments. For this purpose we acquire melting series at various temperatures as shown in figure 5.11.

We summarize our findings in figure 5.12 where we show the characteristic features of the solid, hexatic and liquid phase.

5.7 Discussion and Conclusion

Real space investigations give direct access to the calculation of spatial and temporal correlation functions as well as the defect count that allow to test the KTHNY melting scenario.

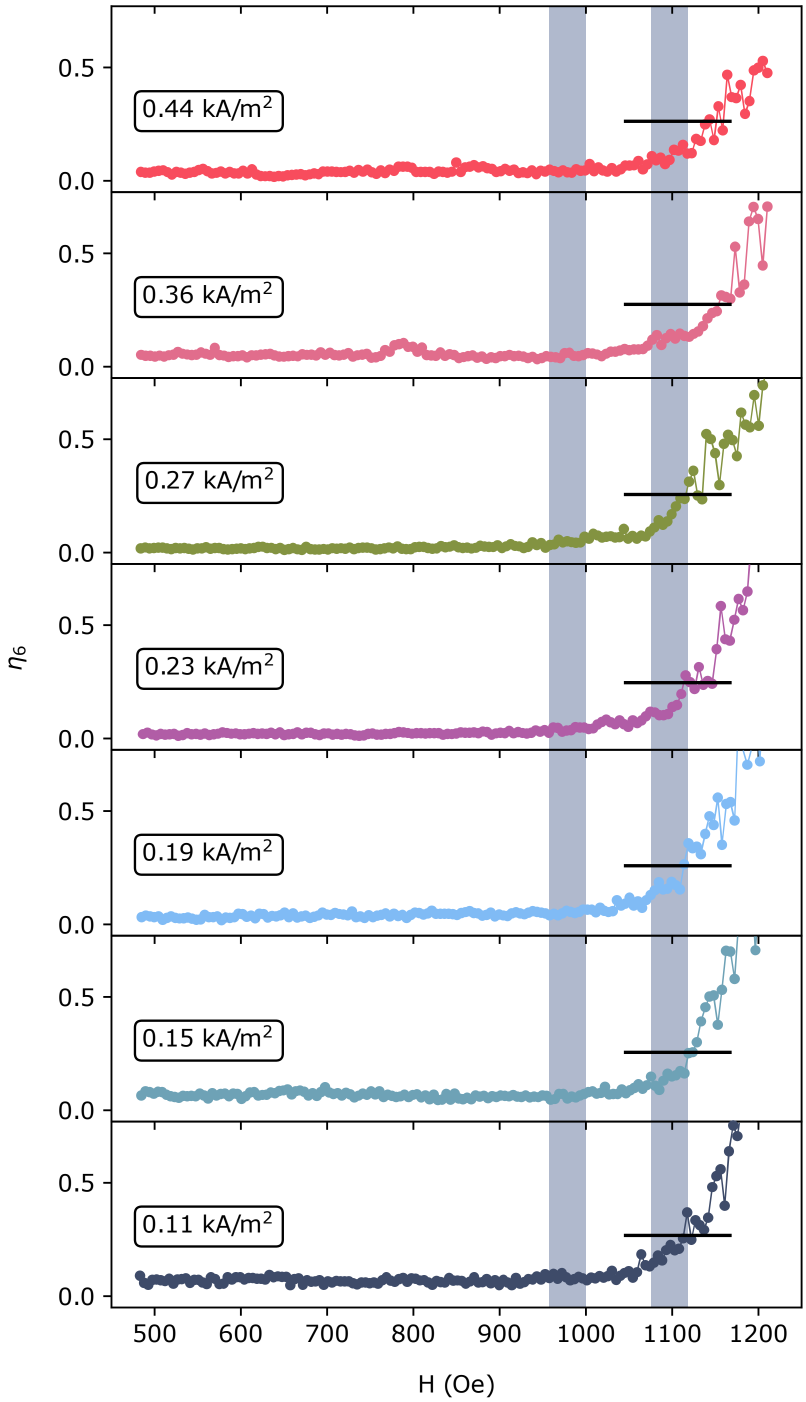

Figure 5.10: Algebraic decay exponent η_6 as a function of magnetic field for various beam intensities. The critical value of 1/4 is marked as horizontal line. Shaded areas highlight the region where the two phase transitions happen. Figure reproduced from the author's published work [64].

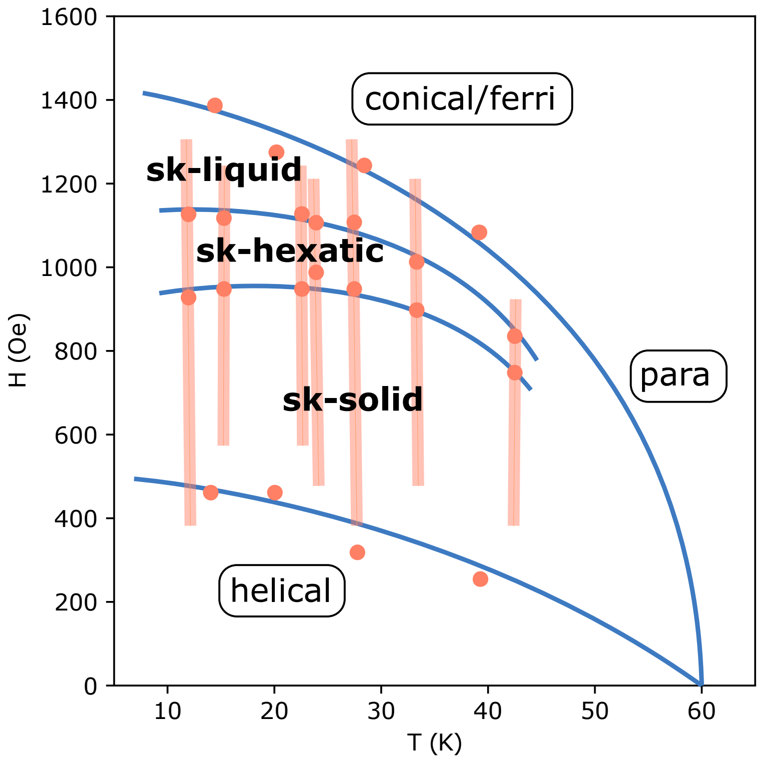

Figure 5.11: Phase diagram for the lamella of Cu_2OSeO_3 studied. The red vertical lines indicate the range of magnetic field ramp, red dots mark the data points based on changes of the decay exponent extracted from the translational and orientational correlation function. The blue lines mark the phase boundaries. Figure reproduced from the author's published work [64].

Until now, all these tests have been carried out on real matter particles. This is the first time that this theory has been tested for quasi-particles such as skyrmions. While they do form lattices just as real matter particles, their properties can differ significantly from their real matter counterparts. For instance the skyrmion number is not a conserved quantity and varies with thermal fluctuations. Moreover, the particle-wave duality in the description of skyrmions imposes two distinct melting scenarios. Sometimes the description of skyrmions is most practical within the particle picture, e.g. to describe their motion via the Thiele equation [98, 99]. On the other hand, a skyrmion lattice phase is often considered as a coherent superposition of spin helices akin to a standing wave configuration. Within this picture, though, we would expect merely a single first order phase transition from the skyrmion lattice phase to a phase without skyrmions as opposed to our observations. Indeed the particle scenario is in line with our findings, since the skyrmions persist throughout the melting process while exhibiting non-trivial phase behaviour, before the skyrmions individually undergo a magnetic phase transition at the atomic level to a paramagnetic or spin-polarized state. Recent Monte Carlo simulations [100] only find a single step melting transition from the solid to the liquid phase, whereas we have found ample experimental evidence for a two step transition consistent with ensembles of real matter particles [61] along with the discovery of the new skyrmion hexatic

	SOLID	HEXATIC	LIQUID
real space LTEM images	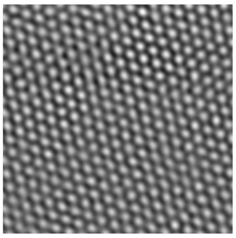	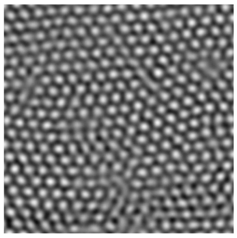	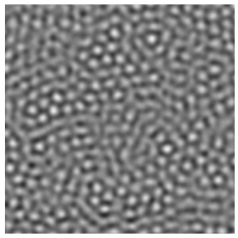
topology	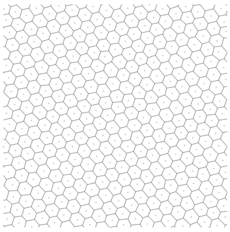	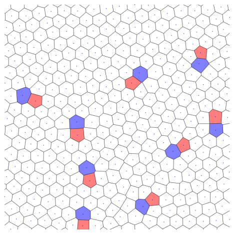	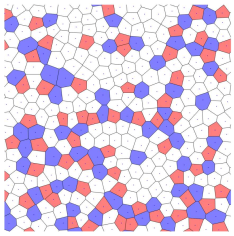
Fourier transform	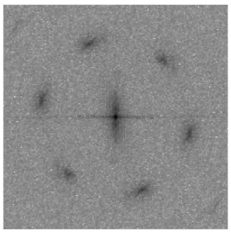	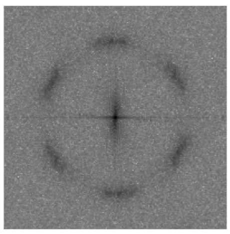	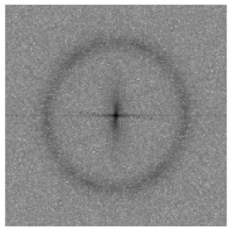
trans-lational order G_k	quasi-long-range order power-law decay $\eta_k < 1/3$	short-range correlation exponential decay	short-range correlation exponential decay
orien-tational G_6	long-range order constant $G_6 \to 1$	quasi-long-range order power law decay $\eta_6 < 1/4$	short-range correlation exponential decay

Figure 5.12: Summary of the properties of the different topological phases: the skyrmion solid, skyrmion hexatic and skyrmion liquid phase. Figure reproduced from the author's published work [64].

phase. However, the coupling of the system to its substrate generally determines whether one can observe two or just one topological transition. Skyrmions in Cu_2OSeO_3 are not strongly pinned to the underlying atomic lattice and therefore a two step transition can be observed. The situation can therefore be quite different in other skyrmion hosting systems, where a two-step continuous phase transition can give way to a single first order phase transition. For example, preliminary analysis of Lorentz imaging data on $Co_8Zn_3Mn_3$ by collaborators at DTU suggests a transition from a skyrmion solid to a skyrmion gas phase. While our results support the KTHNY picture of a melting process across two continuous transitions, the homogeneity of the sample itself is also a factor to be considered. In chapter three we have discussed reasons how strain and thickness variations of the TEM lamella can affect the appearance of skyrmions. This in conjunction with local pinning sites e.g. introduced by Ga-ion implantation or other defects in the crystal, may be responsible for some phase coexistence, which would somewhat smear out the otherwise continuous phase transition that we observe, since the correlation functions are calculated for the entire field of view. Stress should be less of an issue here since the lamella is free-standing and no electric field is applied which can induce additional stress.

We further show that skyrmion systems are an ideal condensed matter system testbed to study collective behaviours, ordering and correlations in two dimensions in real time and real space using Lorentz transmission electron microscopy. The controlled creation of disordered configurations could also be of interest for the magnonics community where skyrmion lattices start to be used as magnonic crystals [101, 102]. The band structure could temporarily be changed by going through e.g. the solid to the hexatic or liquid phase and hence changing or stopping the transmission of signals. Finally, we can go beyond the quasi-equilibrium melting scenario described here and explore dynamic aspects of the system by driving it out of equilibrium in a controlled manner. We cover some of the emerging phenomena in the following chapter.

6 Kibble-Zurek Mechanism

In the previous chapter we studied the behaviour of melting skyrmion lattices. One key feature of the KTHNY melting theory is that it describes a quasi-equilibrium process, meaning that we choose very low magnetic field ramping rates. During this melting process we go through three phases: the skyrmion solid, skyrmion hexatic and skyrmion liquid phase. In principle, the same theory should also apply in a cooling scenario since an equilibrium phase does not depend on its history. Melting and cooling cycles should yield the same results. While melting restores symmetry (the liquid phase has a higher symmetry than the solid phase), the symmetry is broken upon cooling the system down form its high symmetry liquid phase. Since the KTHNY theory describes a two-step continuous phase transition, in the cooling scenario the symmetry must be broken globally unlike in first order phase transitions where a coexistence of phases is observed. This means that the cooling rate must be chosen slow enough such that critical fluctuations can switch the symmetry globally [103]. We verify this by looking at the hysteresis curves of different parameters, most importantly the averaged local order parameter $< \psi_6 >$ and the number of defects, as shown in figure 6.1.

We acquire movies of skyrmion configurations starting from the solid phase at low magnetic fields, ramping into the liquid phase at high magnetic fields and ramp back down to the solid phase. For the lowest ramp rate of 3.2 Oe/s we observe a negligible hysteresis both for the order parameter and the defect count. However, it opens up considerably when increasing the ramp rate. While for low field ramping rates when the system is in quasi-equilibrium, we can expect KTHNY theory to also describe the freezing scenario, this is not the case for faster quenching rates. Instead, similar studies on colloidal systems show that rapidly freezing the system from its liquid state results in a polycrystalline state without any signature of a hexatic phase [103].

In the following we explore in more detail the behaviour of the system when it is driven out of equilibrium and explore the dynamics at different quench rates. We try to understand what could be the underlying mechanism to describe these non-equilibrium processes. This means to understand how the high symmetry in the liquid phase is broken in favour of a low symmetry polycrystalline domain structure that we observe. It touches upon fascinating

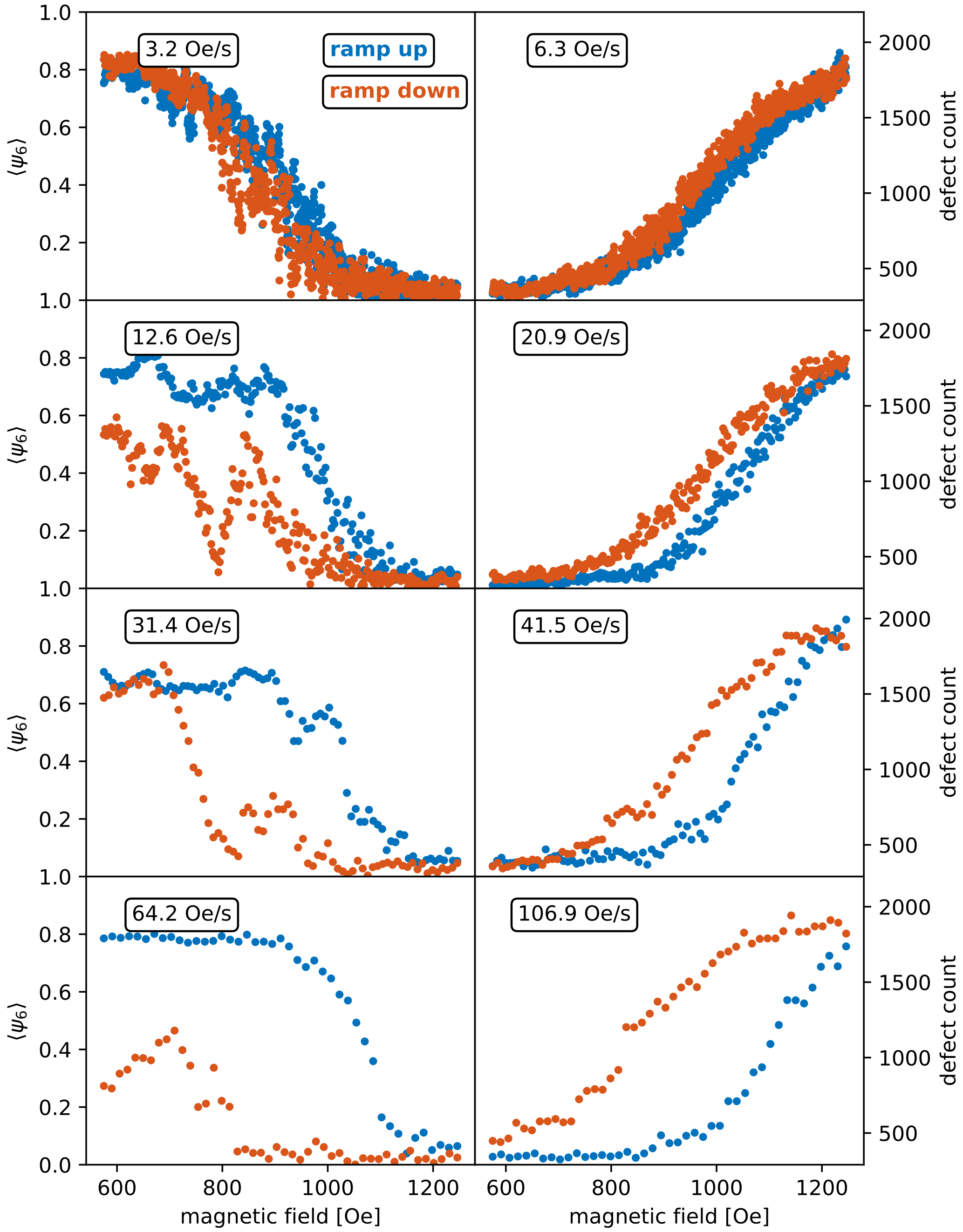

Figure 6.1: Evolution of characteristic parameters while ramping the magnetic field up (blue data points) and down (red data points): average local order parameter $< \psi_6 >$ (left panels) and defect count (right panels).

questions of how physical systems can behave similarly across a orders of magnitude in size and time.

6.1 Basic Idea of the Kibble-Zurek-Mechanism

Kibble laid the theoretical ground work of how domain structures developed shortly after the Big Bang during the expansion and cooling phase of the early universe [104, 105]. Regions that are too far away to communicate with each other even at the speed of light, are causally disconnected, which implies that the order parameter takes on different values in these domains. The symmetry is therefore not broken globally but locally. Various types of topological defects may arise during this process (such as magnetic monopoles [106]) albeit none have been observed to date. The topic regained relevance when Zurek pointed out that these dynamics could also be studied in condensed matter systems, e.g. superfluid helium. He further improved the estimate for the average domain size and predicted a universal power law for the density of topological defects as a function of the rate at which the phase transition is crossed [107].

Within the Landau theory of continuous phase transitions the equilibrium correlation length ξ and equilibrium correlation time τ diverge as a universal power law when approaching the critical point [72]:

$$\xi = \xi_0 |\epsilon|^{-\nu} \tag{6.1}$$

$$\tau = \tau_0 |\epsilon|^{-z\nu}, \tag{6.2}$$

where ν and z are the critical exponents and ϵ the reduced control parameter of the control parameter λ:

$$\epsilon = (\lambda_c - \lambda)/\lambda_c, \tag{6.3}$$

with λ_c being the control parameter at the critical point. At a constant quenching rate $\dot{\epsilon}$ the time t before reaching the critical point is given by

$$t = \frac{\epsilon}{\dot{\epsilon}}, \tag{6.4}$$

and the critical point is reached at $t = 0$. The dynamics can be divided into two distinct regimes: a quasi-adiabatic regime when the control parameter is far away from the critical point $|\lambda| \gg \lambda_c$, the relaxation time τ is small and the dynamics is fast enough (adiabatic). And a frozen regime close to the critical point when the relaxation time is larger than the time it takes to reach the critical point at a given quench rate [108], see figure 6.2 for a visual explanation. In this frozen regime the domain structure at the freeze out time $\hat{t}$ is essentially locked in.

From equation 6.2 and equation 6.4 we can estimate the transition to the frozen stage to happen when

$$\tau \approx t. \tag{6.5}$$

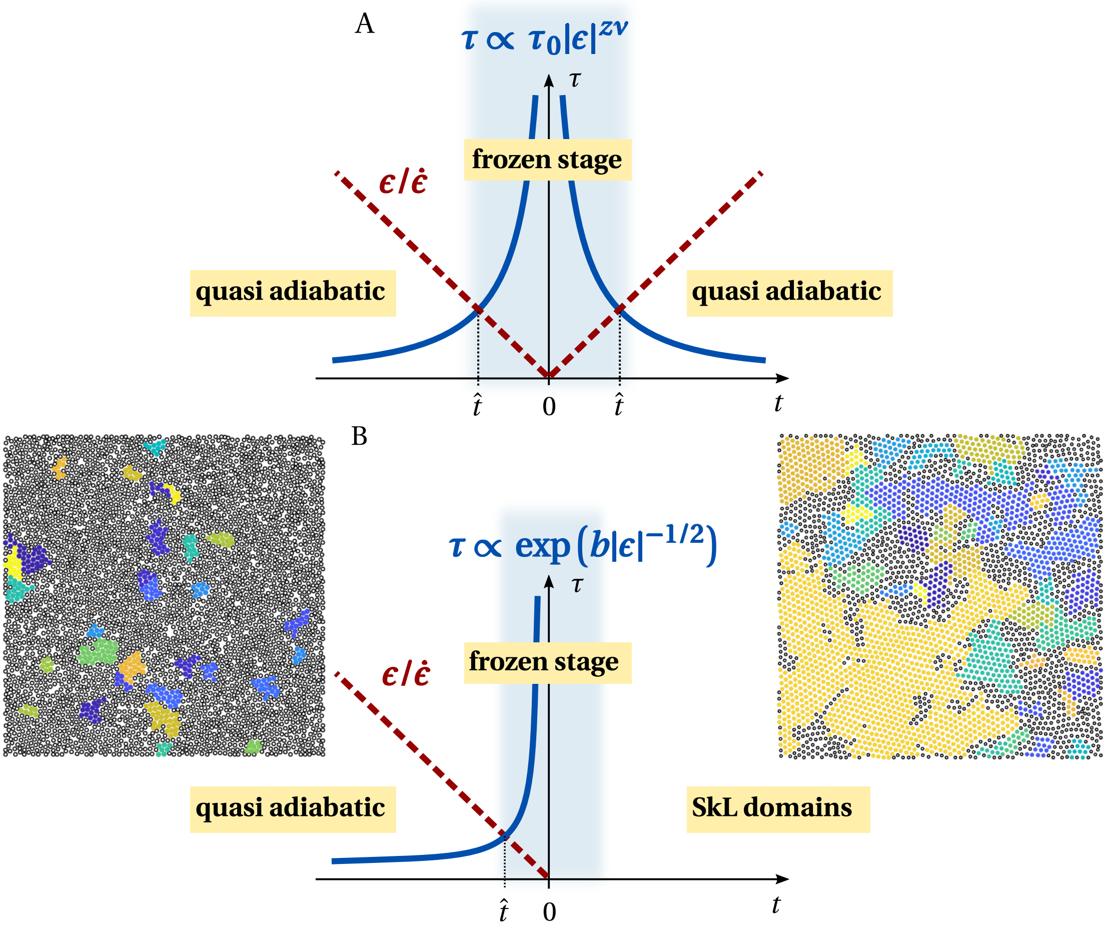

Figure 6.2: Illustration of the basic idea of the Kibble-Zurek mechanism. For a given control parameter ϵ (in our case the reduced magnetic field as given by eq. 6.3), the system has a characteristic relaxation time τ. For a given quench rate $\dot{\epsilon}$ it takes a certain time $\epsilon/\dot{\epsilon}$ to reach the critical point (in our case the liquid to hexatic transition). The intersection of the straight lines given by $\epsilon/\dot{\epsilon}$ and τ define the frozen time at which the quench rate is faster than the time the system has to follow. The classic case for a continuous phase transition with algebraically decaying correlation function is shown in A, the modified scenario with exponentially decaying correlation functions within the KTHNY theory is shown in B. The two skyrmion configurations are snapshots before (left, quasi-adiabatic regime) and after (right, frozen regime) crossing the freezing point.

The frozen time $\hat{t}$ is then given by

$$\hat{t} = \left(\tau_0 \dot{\epsilon}^{-z\nu}\right)^{\frac{1}{1+z\nu}}, \tag{6.6}$$

and the reduced order parameter at the frozen time $\hat{\epsilon} = \epsilon(\hat{t})$ is given by

$$\hat{\epsilon} = (\tau_0 \dot{\epsilon})^{\frac{1}{1+z\nu}}, \tag{6.7}$$

such that the frozen correlation length $\hat{\xi}$ at this point is given by

$$\hat{\xi} = \xi(\hat{\epsilon}) = \xi_0 \, (\tau_0 \dot{\epsilon})^{\frac{1}{1+z\nu}}. \tag{6.8}$$

This relates the average equilibrium domain size to the domain size at the frozen point. The key prediction of the KZ-mechanism is that this relationship follows a power-law.

6.2 KZM Within the KTHNY Universality Class

In this study, we would like to investigate whether the Kibble-Zurek mechanism can be applied to the KTHNY universality class that skyrmion lattices in Cu_2OSeO_3 fall under as we have established in the previous chapter. Within the KTHNY theory, the correlation functions diverge exponentially and not algebraically as in second-order phase transitions [72]. The orientational correlation length ξ_6 and correlation time τ_6 are given by [72]

$$\xi_6 = \xi_0 \exp\left(a|\epsilon|^{-1/2}\right), \tag{6.9}$$

and

$$\tau_6 = \tau_0 \exp\left(b|\epsilon|^{-1/2}\right). \tag{6.10}$$

We use this to modify the KZM accordingly and illustrate this schematically in figure 6.2. Zurek himself discusses some details of applying the KZM to the KTHNY universality class [109]. Using equation 6.10, the frozen time $\hat{t}$ is given by

$$\hat{t} = \tau_0 \exp\left(b|\hat{t}\dot{\epsilon}|^{-1/2}\right), \tag{6.11}$$

which can be solved numerically. In order to get the frozen times one needs to extract the relaxation times τ_6 at different magnetic fields in the liquid phase (see previous chapter) so as to be able to fit the data according to equation 6.10, which in turn feeds back in to equation 6.11 from which the frozen times for different quenching rates $\dot{\epsilon}$ can be extracted numerically. The time correlation functions for τ_6 are shown in figure 6.6 along with their exponential fits to extract the time constant. Strangely, we obtain relatively long correlation times in the range of one minute. Moreover, the times seem to depend randomly on the field. One would expect the shortest correlation time at the highest field deep in the liquid phase at 1341 Oe. However, here it is the longest, and the times do not become longer when approaching the liquid to hexatic transition but shorter. Pinning of skyrmions in Cu_2OSeO_3 is low, but perhaps extended electron beam irradiation deteriorated the sample with the introduction of crystal defects that act as pinning sites and slow down the dynamics. For the time being, we choose a different

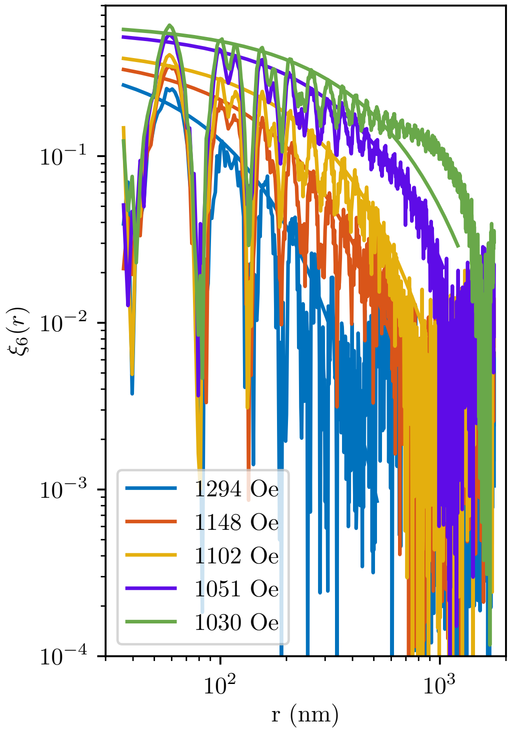

Figure 6.3: Orientational correlation functions $\xi_6(r)$ for a few representative fields along with exponential fits to extract the correlation lengths.

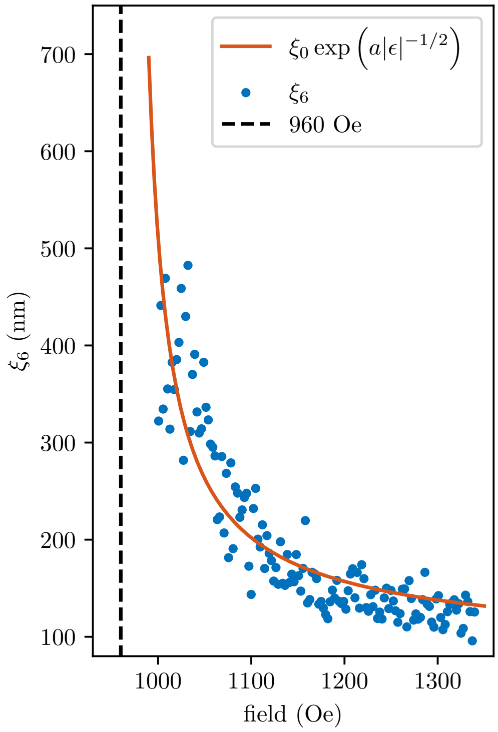

Figure 6.4: Exponential fit of the correlation lengths as extracted from figure 6.2.

way to extract the frozen times. It is to be used with caution, though, since it involves basically guessing two parameters. We base it on the field dependence of the correlation length that we extract from a series at the slowest quenching rate. The correlation length is extracted form each frame of the series within the liquid phase (fields roughly above 960 Oe at 25 K, see figure for a few representative correlation functions. The extracted correlation lengths ξ_6 along with a fit according to equation 6.9 are shown in figure 6.4. The correlation length and relaxation time are related by the dynamical scaling hypothesis [110] via

$$\tau = c\xi^z \tag{6.12}$$

where c is a constant. We use this relation along with equation 6.9 to estimate the relaxation times:

$$\tau_6 = c\left(\xi_0 \exp\left(a|\epsilon|^{-1/2}\right)\right)^z \tag{6.13}$$

The frozen times $\hat{t}$ are then given by

$$\hat{t} = c\left(\xi_0 \exp\left(a|\hat{t}\dot{\epsilon}|^{-1/2}\right)\right)^z \tag{6.14}$$

The solution to this equation is shown graphically in figure 6.5. The frozen time is when the straight lines given by equation 6.4 intersect with τ_6. At the same time we obtain the corresponding frozen magnetic fields. We choose the parameters c and z such that the intersection for the slowest ramp rate and τ_6 is not far off the transition field at 960 Oe since we established before that this should correspond to a quasi-equilibrium situation. On the other hand we assume that the fastest quench should fall out of equilibrium very early and therefore the corresponding intersection shall be at a high field. We therefore choose $c = 0.023$ and $z = 0.51$.

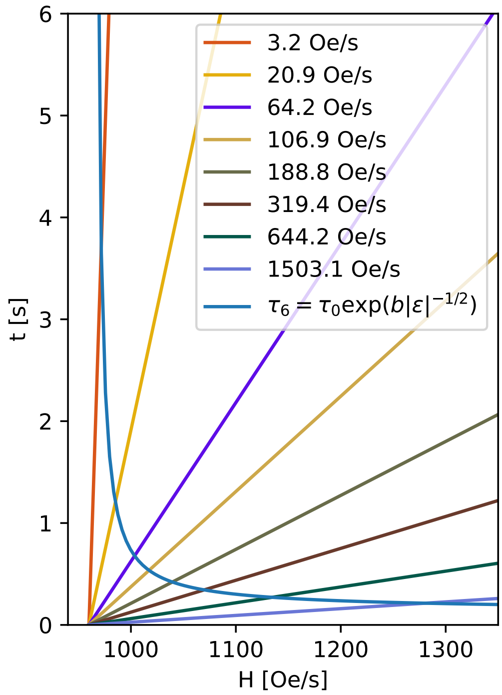

Figure 6.5: Time left to the hexatic transition coming from the liquid phase as a function of the magnetic field and quench rate given by straight lines. Estimate of the relaxation time based on fit of the correlation length, see text.

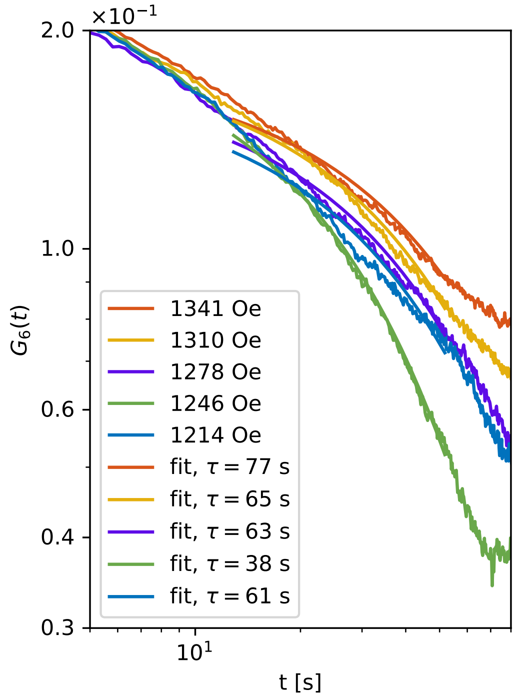

Figure 6.6: Time correlation functions $G_6(t)$ for a few magnetic fields along with their exponential fits to extract the relaxation time τ.

We use relation 6.12 for the modified prediction of the KZM scaling law based on the KTHNY universality class, feeding in the frozen times found via equation 6.14:

$$\xi = \left(\frac{\hat{t}}{c}\right)^{1/z} \tag{6.15}$$

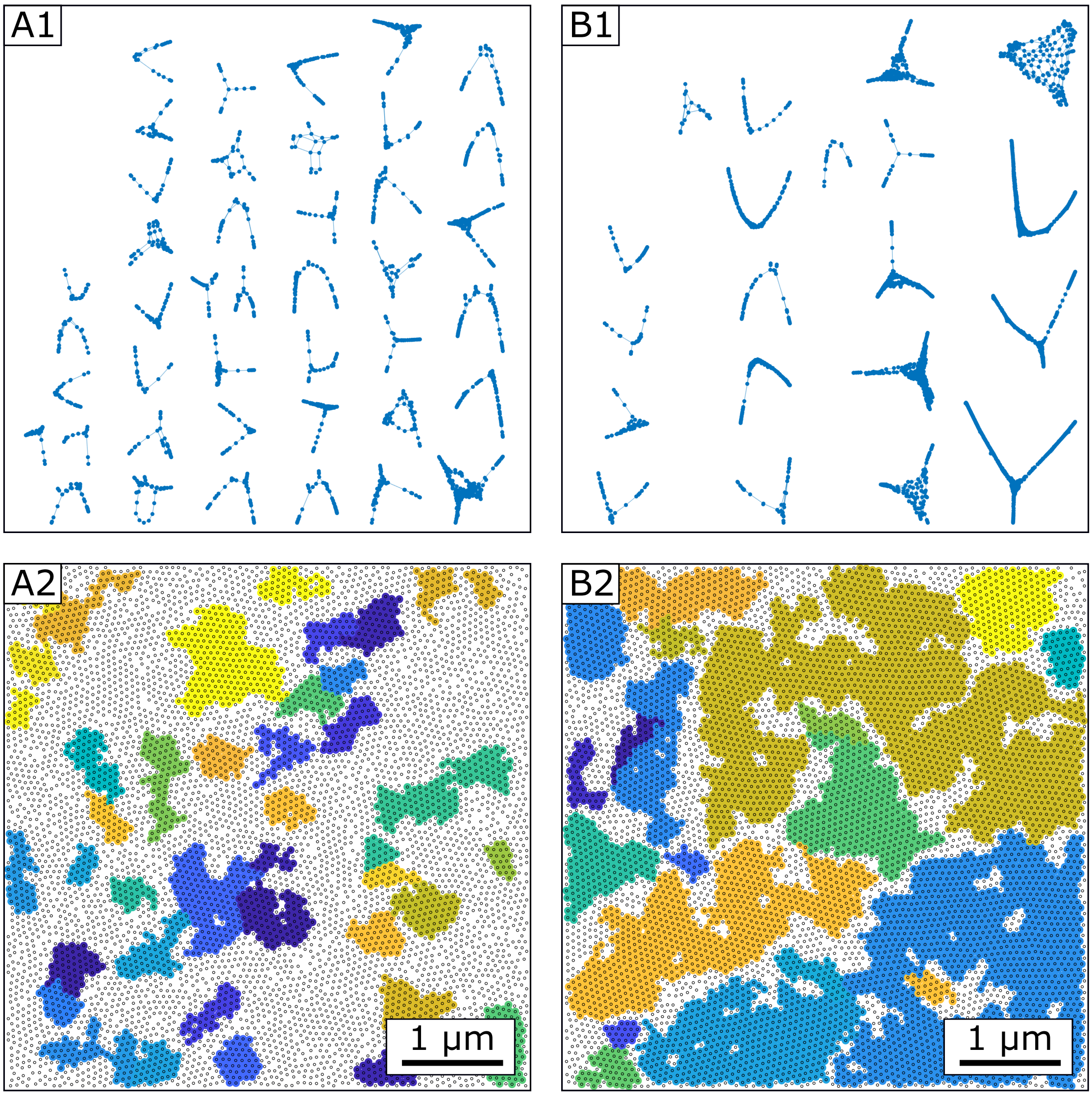

Figure 6.7: Graphs of multiple adjacency regions in the liquid phase (during field quench) illustrating point connectivity as obtained by cutting connections in the single adjacency region (A1). These graphs are used to colour the corresponding domains (A2). B1 and B2 depict the corresponding situation at the end of the field quench.

6.3 Estimation of Domain Sizes

The key prediction of the KZM is the power law dependence of the frozen-in domain size as a function of the quenching rate. We therefore follow the procedure outlined in chapter four to extract the domains in the skyrmion configurations we observe. Based on the local orientational order parameter

$$\psi_6(\boldsymbol{r}) = |\psi_6(\boldsymbol{r})| \exp(i\theta_6(\boldsymbol{r})). \tag{6.16}$$

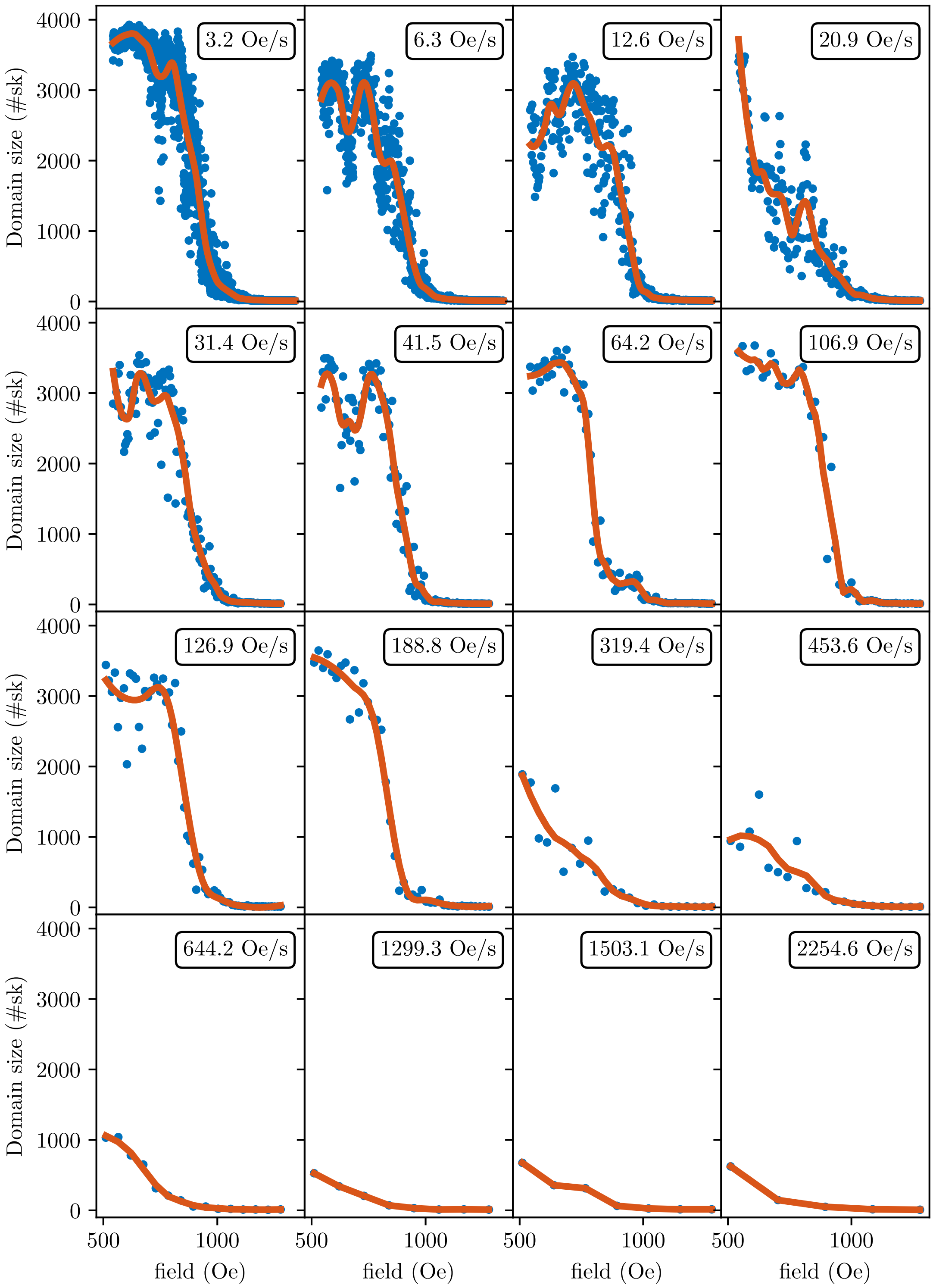

Figure 6.8: Average domain sizes as a function of the magnetic field and for different quench rates.

Individual skyrmions can be considered to be part of a certain domain if the following conditions are met [72]

1. the phase angle $\theta_6(\boldsymbol{r})$ between two neighbouring sites i and j is less than 14°
2. the magnitude $|\psi_6(\boldsymbol{r})|$ is larger than 0.6 for neighbouring sites
3. the bond length deviation between neighbouring sites is less than 10% of the average particle distance

The first condition concerning the angles is different from the one that we specified in chapter four, where we put angles into bins. In fact, the domains in the series studied in chapter four were so regularly arranged without any bending that determining clusters based on the absolute and not relative angles was the best choice. Here this criterion is less suitable. Domains of different orientations arise during the cooling process when they are not connected by causality. They may very well be bent, however, such that the local change in angle of neighbouring points is actually small. Therefore, we cut connections based on the relative angles between points. As described in chapter four, connections in a single adjacency region based on Delaunay triangulation are broken according to the three conditions above. This yields multiple adjacency regions as illustrated in figure 6.7 by the graph plots. These can be used to find the indices of points that belong to one domain, shown in figure 6.7. See chapter four for more details. We use this to plot the domain sizes (# of skyrmions) as a function of the magnetic field for the range of quench rates we apply, see figure 6.8. We clearly see how the quench rate influences the evolution of domain sizes. While for slow quench rates large domains are recovered at low magnetic fields, they remain small for high quench rates and the onset of the increase in size shifts to lower magnetic field values. We observe a similar behaviour in figure 6.1, where the onset of the increase of the order parameter and the onset of the decrease in the defect count change to lower field values for higher quench rates. This is again in accordance with the KZM picture, which describes how defects from the high symmetry phase are frozen in when crossing the critical point [72].

We extract the domain size at the frozen fields that we obtained above, convert it into a reduced length (correlation length divided by skyrmion lattice constant) and plot them in figure 6.9 as a function of the quench rate. We also plot the KZM predictions based on equation 6.15 and a power-law fit for comparison. As a matter of fact, the algebraic fit based on the standard KZM corresponds better to the data than the modified KZM prediction. However, we need to take this result with a grain of salt. One major issue is the determination of the frozen times, as discussed above. Nevertheless, key elements of the KZM hold.

Zurek himself goes into some detail explaining the intricacies of applying the KZM to systems of the KTHNY universality class. In general, one can only expect a power law dependence of the frozen domain size on the quench rate in the limit of very slow quenches that are experimentally inaccessible. But locally, within a few orders of magnitude, the behaviour can indeed be algebraic.

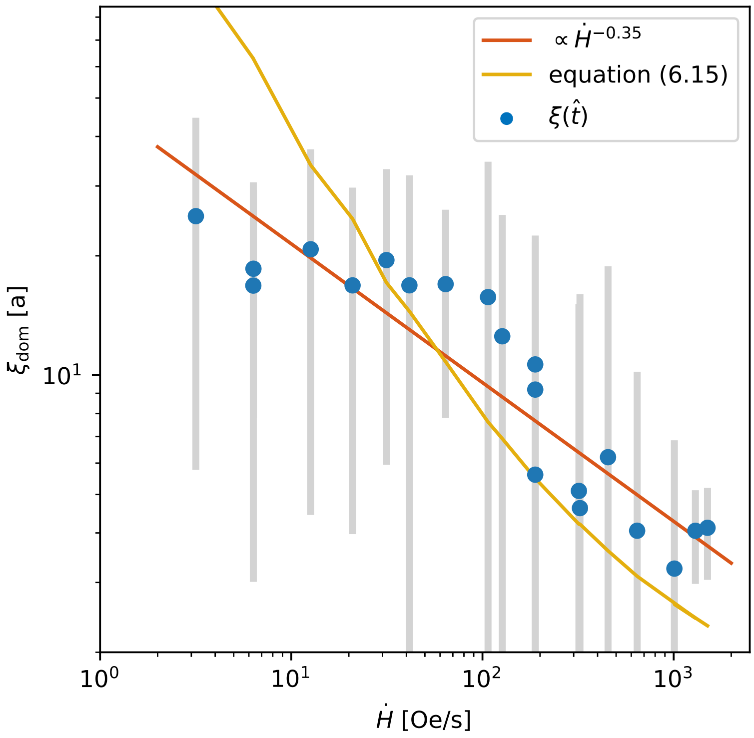

Figure 6.9: Dependence of the frozen domain size of the quench rate (blue dots, with standard deviation (grey)). Power law fit (red) according to standard KZM and modified prediction (yellow) based on the KTHNY universality class.

6.4 Conclusion

We have analysed the non-equilibrium behaviour of freezing of skyrmion liquids into their solid phase as a function of the magnetic field quench rate within the Kibble-Zurek picture. One main issue remains the correct determination of the frozen times for our system. We resorted to an educated guess for the moment. Nevertheless, key elements of the KZM hold for skyrmions as well. The average domain sizes clearly depend on the quench rate and based on the frozen times we determined, the frozen domain size obeys an algebraic decay as a function of the quench rate across more than three orders of magnitude as predicted by the KZM.

There are many more interesting phenomena to be studied in this system. While above we explored the behaviour until the critical point is reached and the system freezes, one can go beyond that and study the system after the critical point has been passed. This may include e.g. relaxation dynamics, domain coarsening and domain growth. Such an analysis could follow the procedure outlined in chapter four to highlight grain boundaries.

7 Conclusions and Outlook

In this thesis, we have investigated skyrmions both from a highly applied perspective and a very fundamental one. Using the unique magnetoelectric properties of skyrmions in Cu_2OSeO_3, we achieved reproducible switching in a geometry that is most viable with respect to a technological application in data storage. That is the [111]-geometry, in which a lamella of Cu_2OSeO_3 is sandwiched between two electrodes. We tuned the material parameters (electrodes, silicon-nitride window, thickness of the lamella) such as to perform real time and real space observations using Lorentz transmission electron microscopy. We developed new image analysis algorithms to extract skyrmions from even noisy environments and in a statistical average obtain meaningful results. We characterised the device in terms of numbers of skyrmions generated depending on the bias, skyrmion creation and annihilation times and hysteresis loops. Furthermore, we made first prototypes of multiarray devices that allow skyrmion control on a more local level. At the same time we developed new sample preparation techniques for in-situ TEM biasing that involve both top-down and bottom-up fabrication using the FIB and clean room processes.

Another main focus of this thesis was the investigation of how ensembles of skyrmions in Cu_2OSeO_3 evolve under the influence of external stimuli. This work consists of three main parts: the analysis of the defect structure in dynamically evolving skyrmion configurations, the study of the melting behaviour of skyrmion lattices under a controlled magnetic field ramp in quasi-equilibrium and finally the reverse case of studying non-equilibrium phenomena by quenching skyrmions from their high symmetry into their low symmetry phase. The experiments were all carried out on thin lamellas of Cu_2OSeO_3 and using Lorentz transmission electron microscopy. We developed an algorithm that can reliably extract strings of dislocations at low angle skyrmion lattice grain boundaries both for visualization and further analysis. We show how the density of dislocations is related to the difference in angle of adjacent skyrmion domains. We further developed algorithms to extract the domain structure of any given skyrmion configuration and algorithms to visualise the grain boundaries themselves and the angle by which domains are separated. These dislocations are also at the core of another phenomenon that we studied: the magnetic field induced melting of skyrmion lattices. We show that it is a two-step defect-mediated process that is based on the emergence of disclocations and their subsequent dissociation into free disclinations. The appearance of dislocations first breaks the quasi long range translational symmetry of the skyrmion solid phase while a long range orientational order remains preserved. This characterises the thus far unknown skyrmion hexatic phase for which there has been no experimental proof to this date. The following dissociation of dislocations in turn breaks the orientational symmetry and leads to the skyrmion liquid phase with short range translational and orientational order. We provide robust evidence for our findings by considering multiple observables: from the count of disclocations and disclinations to the calculation of various spatial and temporal correlation functions and show that our system belongs to the KTHNY universality class, which provides the theoretical framework to describe melting in two dimensions. While primarily of fundamental interest, the understanding of different skyrmion phases is also critical for future spintronic applications that are based on the band structure of magnonic crystals [111]. Finally, we investigated non-equilibrium phenomena when quenching skyrmions from their liquid phase into the solid phase at magnetic field quench rates spanning three orders of magnitude. The faster the quench rate the earlier the system falls out-of equilibrium and emerging domains during the cooling are not causally connected anymore. The corresponding length scale depends on the cooling rate and we find evidence that this particular skyrmion system belongs to the Kibble-Zurek universality class. The Kibble-Zurek mechanism predicts a power-law scaling of the characteristic frozen correlation length as a function of the cooling rate.

Overall, we acquired hundreds of movies with a total of more than 100.000 frames. A major part of this work was the analysis of these large data sets and the development of efficient image analysis and feature extraction algorithms. This is a trove in its own right. Future analysis could include investigations of phonons in skyrmion lattices, new types of hidden order and other non-equilibrium phenomena besides the KZM such as the evolution of the domain structure after crossing the critical point. Often, parallels can be drawn to other condensed matter systems, where direct observations may not be feasible unlike for ensembles of skyrmions using e.g. Lorentz microscopy.

In terms of electric field control of skyrmions, major progress could be achieved as soon as thin film deposition of Cu_2OSeO_3 is possible. While we fabricated multiarray devices using FIB and clean room processes, certain parameters are beyond our control. These include a perfectly homogeneous thickness of the TEM lamella and the precise distance between the electrodes and local ion implantation or impurities. On the one hand this makes interpretation of results more difficult and on the other hand leads to reduced reproducibility across devices. A controlled thin film deposition would eliminate all these issues and facilitate the integration into existing clean room microfabrication processes. This would bring us closer to another goal as well: an all-electric read out of a skyrmion memory device. Two routes are conceivable: either using a field effect transistor (FET) with the skyrmion host replacing the gate dielectric like in ferroelectric FETs and thus changing the threshold voltage. Two states could then be detected: one without skyrmions and one with skyrmions. On the other hand, Cu_2OSeO_3 is a compound that receives much attention in the magnonics community as well due to its low damping constant [112]. This means that spin excitations or magnons can propagate particularly easily and far. A coherent spin wave could be injected into a thin film of Cu_2OSeO_3 and would scatter off the skyrmions to produce a characteristic interference pattern on the other side. One could then compare this to an arrangement of skyrmions that would cause such a pattern and thus read out the entire memory in a single flush. Magnonic devices are highly coveted since no charge transport is involved, which makes them basically dissipation free.

A Appendix

A.1 Skyrmion Identification in Skyrmion-Only Phases

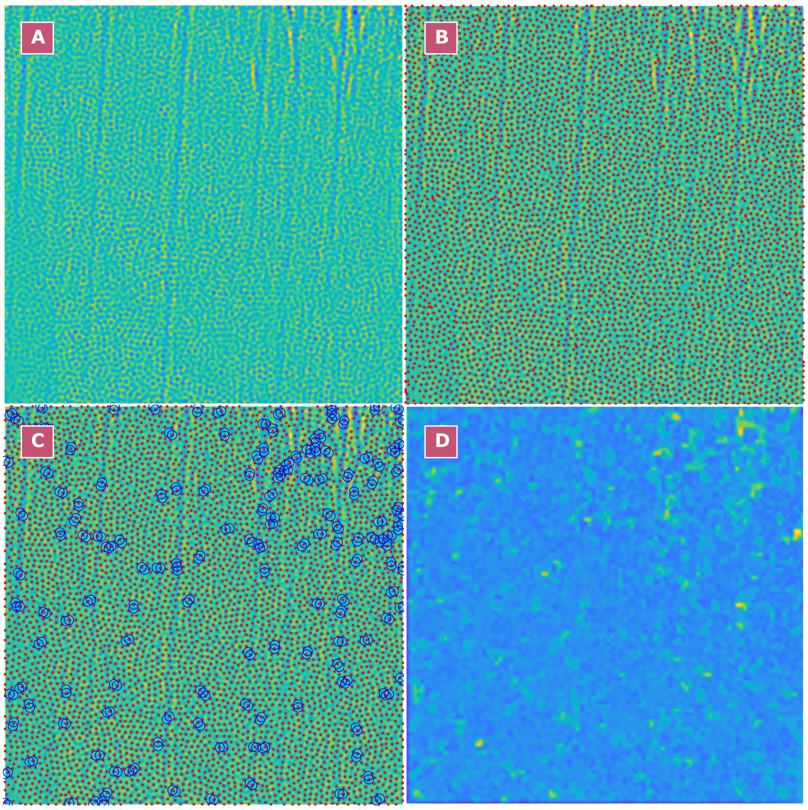

Figure A.1: Steps in the identification of skyrmions in skyrmion-only phases. A: application of a Gaussian of Lagrangian filter on a raw TEM image to enhance contrast and smoothen the image. B: regional minima in intensity are identified as possible skyrmion positions. C: points closer to each other than the average skyrmion distance are considered as misidentified positions and the mean position is taken instead. D: skyrmion density helps to locally loosen or tighten conditions if necessary.

The identification of skyrmions in a field of view that only contains skyrmions is relatively easy. Upon application of a standard Laplacian-of-Gaussian-filter that smooths out the image and enhances contrast (see figure A.1 panel A) each regional minimum can in principle be identified to be a skyrmion (figure A.1 panel B). We can introduce an intensity threshold to discard positions that are most likely artefacts. A minimum intensity threshold further improves the accuracy. Positions that are too close too each other are replaced by their mean position (A.1 panel C). A skyrmion density map can be calculated as shown in figure A.1 D. Since we assume the density to be ideally constant across the field of view for this particular skyrmion host (Cu_2OSeO_3), we can locally relax conditions where the density is lower than expected or the other way around and apply tighter conditions where the density is too high. An example of the final result of this identification routine is shown in figure A.2.

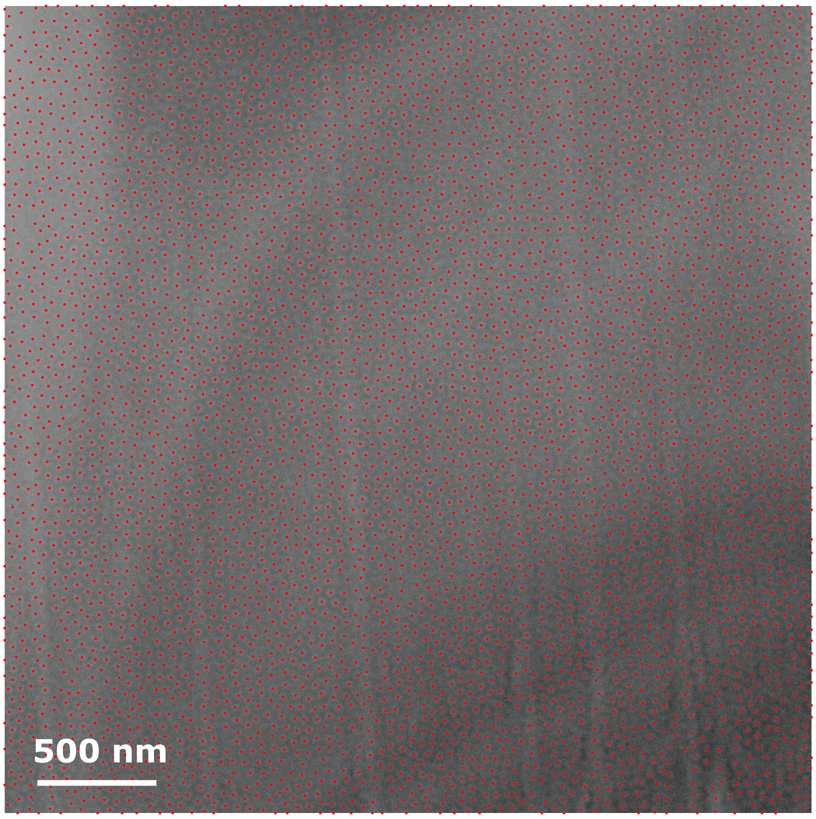

Figure A.2: Final identification result of skyrmions in a skyrmion-only phase.

A.2 Skyrmion Identification Algorithm in Mixed Helical-Skyrmion Phases

When doing the biasing experiments one usually sits right between the helical and skyrmion phase. A former PhD student in LQM, Ping Huang, used an algorithm to identify skyrmions in a helical background that is based on fingerprint recognition. While this worked very nicely, the problem in my case is with the the additional layers making up the device. The electrons not only have to pass through the lamella, but also through the membrane of SiN and two electrodes made of a metal bilayer (10 nm of Ti and 2 nm of Pd as a capping layer). Unfortunately at the defocus for ideal magnetic contrast in Cu_2OSeO_3 it just so happens that the grains in the metal are blown up to approximately the same size as skyrmions, making the point identification all the more challenging. However, we notice that most grains are not necessarily perfectly round as skyrmions in this material ideally are.

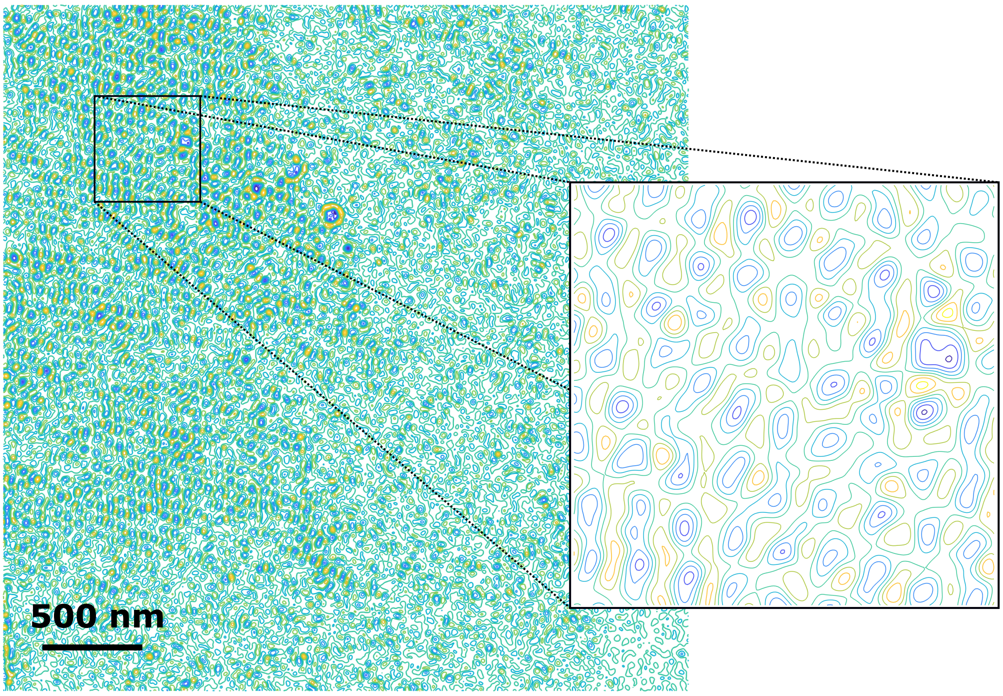

Figure A.3: Skyrmion identification based on counting rings of constant intensity.

To be identified as a skyrmion a blob should have a certain intensity and be round. In figure A.3 we show a contour plot of a TEM images containing skyrmions. The contours are lines of constant intensity. Visually this means that a potential skyrmion will be surrounded by a number of rings whereas an impurity may have one or two round rings at a certain intensity but then those rings become more oddly shaped. In practice we create binary images at different threshold intensities. E.g. if the image intensity is renormalised to be within 0 and 1, we create binary images at 0.1, 0.2,0.3,... etc. intensity, as shown in the figure A.4.

The connected regions (bright pixels) and their various characteristic parameters such as area

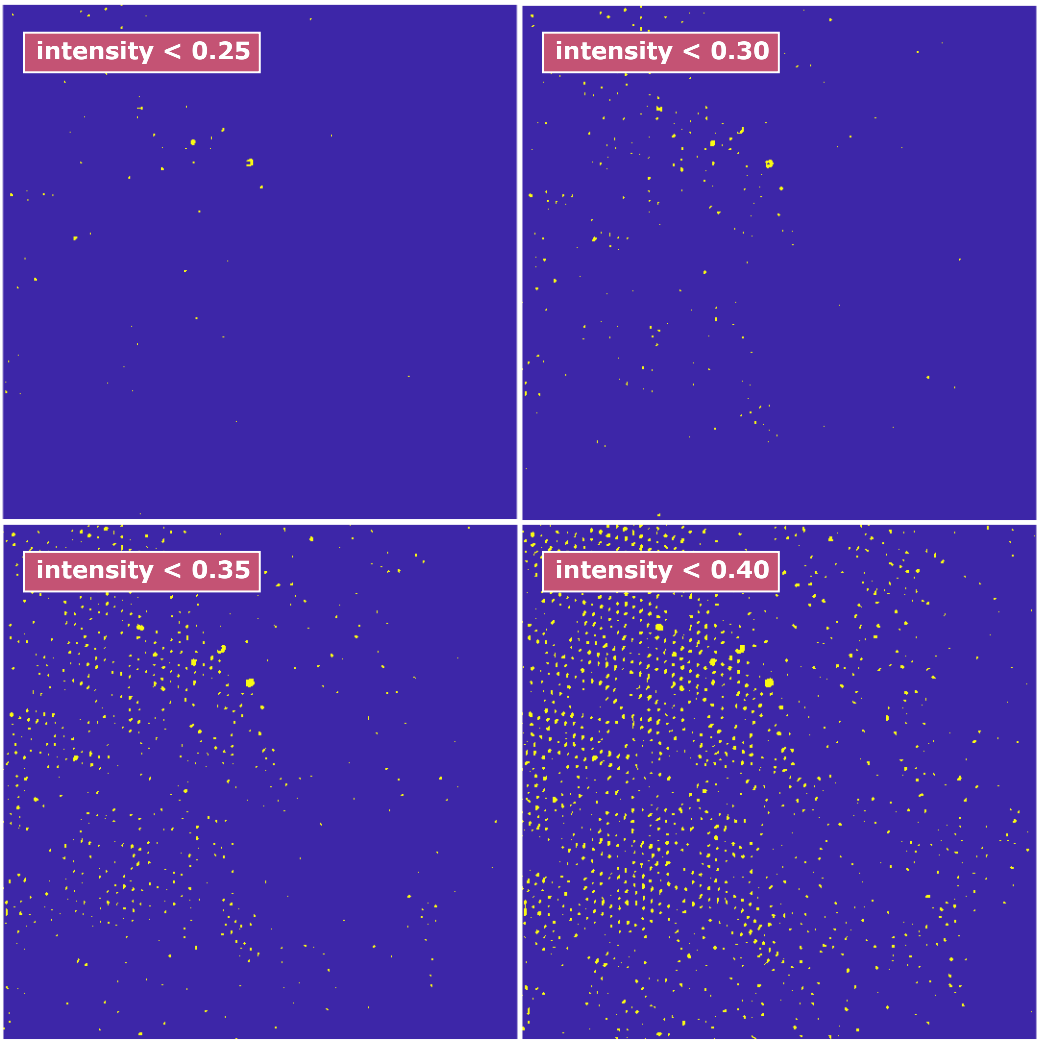

Figure A.4: Creating binary images at indicated threshold intensities.

and perimeter can be extracted. For these regions in each of those binary images we use the following cut off criteria:

- Take only areas above a certain threshold A_{low} and below A_{high}
- Take only areas with a circularity below 1.5

This way many of the connected regions in the binary images will be filtered. All those regions that remain in the filtered image could potentially be skyrmion positions. Now we add all those filtered binary images up, in our case we choose 7 binary images, as shown in figure A.5 A. If the same regions occur in multiple binary images the count will be higher.

We introduce a last filter, which only accepts those regions with a count higher than e.g. 3, which will be used once more to create a binary image, as shown in A.5 B. These are the regions

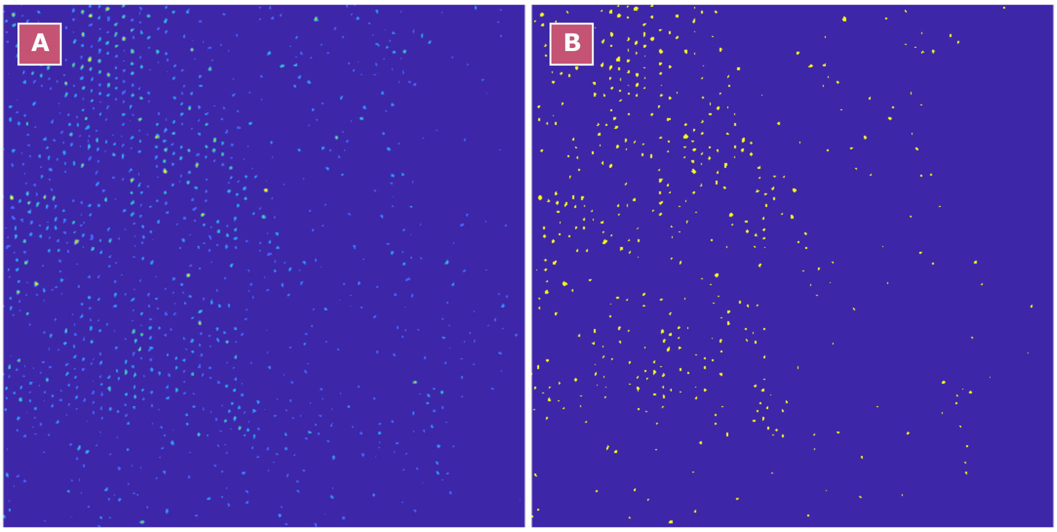

Figure A.5: A: sum of filtered binary images according to criteria specified in the text. B: binary image of A at a certain threshold. These are the identified skyrmion positions.

where skyrmions are most likely to be found. Their positions are therefore identified as the center of mass of the connected regions in this last binary image. The positions are compared with the actual TEM image, as shown in figure A.6.

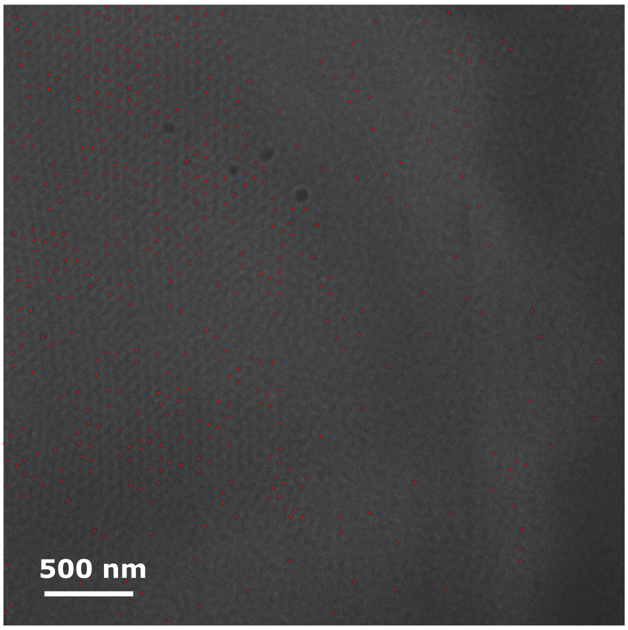

Figure A.6: Final identification result overlayed on the original TEM image.

A.3 Using the Gatan Liquid Helium Cryo-Holder

The following is not an official manual for the operation of the cryo holder, but just reflects my personal experience. Always ask CIME staff before using any equipment.

All of the experiments involving Cu_2OSeO_3 were performed at low temperature and using a Gatan liquid helium cryo-holder. Due to its weight it needs to be hung up to the microscope stage by two springs on each side, see figure A.7. After switching on the turbopump, the holder can be inserted and the pump cycle will be triggered. Hold it by hand for the duration of the pump cycle and then insert fully. Adjust the springs using the screws such that the sample rod in the microscope remains level. Turn the transport dewar such that the pressure gauge is visible from the operating room. The helium transfer tube should not be simply inserted into the holder but rather suspended at the microscope frame such that no additional force is exerted on the holder when inserting the tube, see figure A.8. Prepare a string beforehand. Put on the inflatable latex balloon (within the glove to prevent it from exploding at high pressures) on one end of the transfer tube and slowly insert into the transport dewar, then suspend it on the string and slowly lower it down well into the liquid, see figure A.9. Helium gas will come out at the other end. Adjust the position of the transport dewar if necessary and insert the other end into the sample holder dewar such that it enters without force and does not exert any torque on the holder. Tighten the screw on the holder end. Note that after this point the transport dewar should not be moved at all, since it will not be possible to judge what kind of force the tube will exert on the holder once everything is tightly in place. The worst case would be a pole touch (the gap between the holder tip and the pole piece is only a few mm) and the holder dewar needs to be warmed up and retracted.

Figure A.7: Sample holder with transfer tube, recovery line and exhaust line leading to flowmeter.

Figure A.8: Transfer tube to sample holder suspended at string. Frozen recovery line.

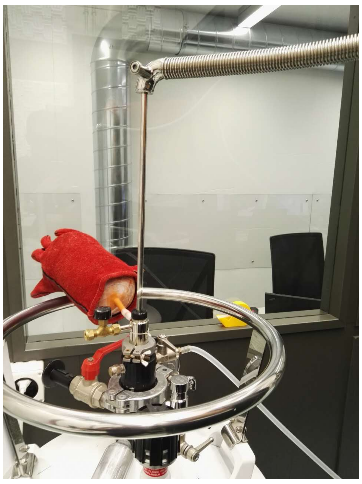

Figure A.9: Transfer line from transport dewar, connected to pressure balloon in glove.

Two helium recovery lines are available in the Titan room. Use one for the transport dewar and the other for the exhaust of the transfer tube on the holder end. Initially, fully open both transfer lines, squeeze the pressure balloon if necessary to achieve an overpressure of around 100 mbar in the transport dewar, ideal for helium transfer. Once liquid helium starts being transferred, a hissing sound in the recovery line becomes noticeable. The manual suggests to observe the helium gas plume at the exhaust without having a recovery line attached. When the plume takes the shape of a Bunsen flame, this is the sign for the start of liquid helium transfer. However, I prefer to recover this bit of helium as well and the valve of the recovery line can be closed or throttled at convenience. Best performance has been achieved following a routine that differs from the one described in the holder manual by leaving the transfer tube attached at all times. This way, a lot of time is saved that would have to be used to warm up the frozen end of the tube with a heat gun and retracting the tube from both the sample and storage dewar. It furthermore allows us to quickly reinitialize the helium transfer once the holder dewar is empty. Attach the flowmeter to the exhaust outlet at the holder dewar and fully open the needle valve. After liquid helium starts to transfer, the temperature will soon decrease rapidly. Continue transfer for about 10 min before closing the recovery line. The pressure in the transport dewar will go up. Slightly throttle the exhaust valve on the storage dewar to release some pressure if necessary. Try not to let the pressure exceed 200 mbar. I had balloons explode at around 250 mbar. Older balloons lose elasticity and break more easily. Adjust the needle valve and exhaust valve on the transport dewar to reach the desired temperature.

A.4 Controlling the Magnetic Field Ramp on an FEI Microscope

For the results presented in the melting chapter, a controlled and continuous magnetic field ramp was necessary. The user interface on the Titan Themis in CIME only allows for manual control via a knob. As shown in the melting chapter, I used a stepper motor and connected it to the knob through a rubber band. This worked well especially for the slow ramps needed for the quasi-equilibrium melting process. However, this method was not really suitable for the fast quenching rates we studied for the Kibble-Zurek mechanism. The interface however does allow a direct control of all lenses of the microscope, see figure A.10.

The lens excitations can be changed incrementally by mouse clicks on the arrow buttons. We automate this part by writing a mouse clicker program that clicks on these buttons at a certain frequency to achieve a controlled ramp using the Python pyautogui library. We furthermore automate the movie acquisition as well. The mouse clicks on the acquire movie button, waits 1 s, which is the time until the acquisition actually starts on this system, then changes the projector lens excitation to rapidly condense and broaden the beam size on the screen, after which the actual ramp is performed by changing the objective lens excitation. The changing beam size prior to the ramp is useful during the subsequent image analysis and acts as a visual trigger for the magnetic field ramp. The same is done once the ramp is finished and the movie acquisition button is clicked again to finish the acquisition.

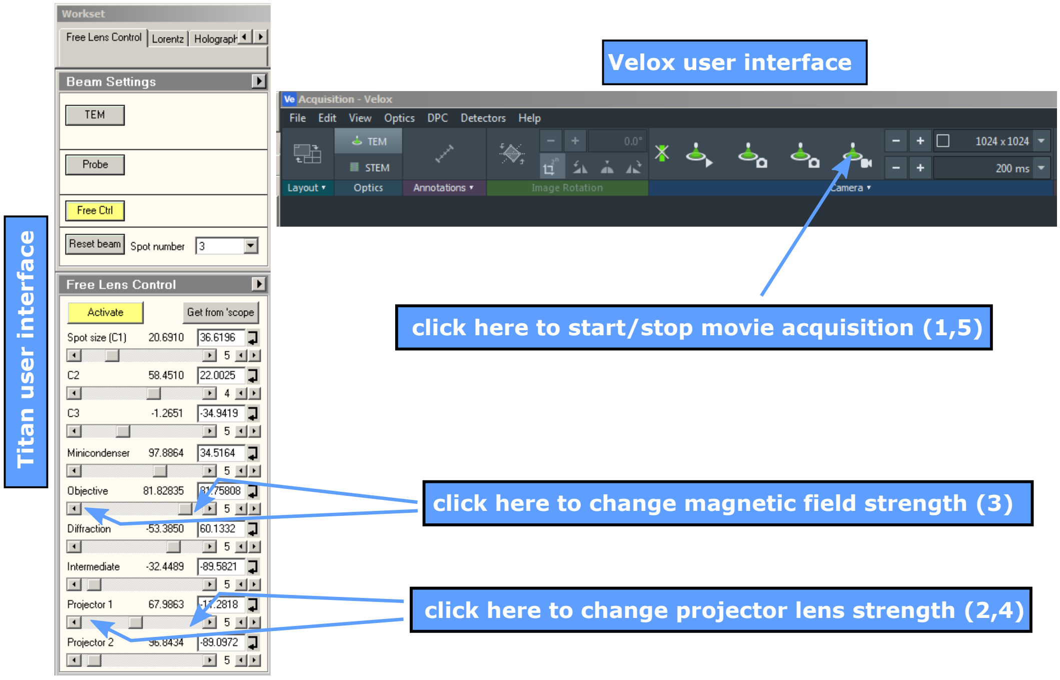

Figure A.10: Microscope and camera user interface. Launch acquisition (1), change projector lens strength as a visual trigger for field ramp (2), field ramp up or down (3), change projector lens strength to mark end of ramp (4), finish acquisition (5).

A.5 Miscellaneous Projects

In this chapter we discuss some projects that were started during this work but are not finished yet. These include an improved technique for the reconstruction of the phase for LTEM imaging, the effect of purposefully introduced defects/holes in TEM lamellae of Cu_2OSeO_3 and the effect of beam intensity in the rotation of skyrmion lattices.

A.5.1 Improved Transport of Intensity Equation for Magnetic Imaging

As the name implies, Lorentz microscopy generates contrast from electrons being scattered by the Lorentz force from in-plane magnetic moments pointing in different directions. In a quantum mechanical description the contrast is generated due to a phase shift of the electron wave function through the magnetic vector potential. The interference with the unscattered electron wave gives rise to differences in intensity recorded on the detector. The so called transport of intensity equation (TIE) can be used to retrieve the phase of the electron waves, which in turn can be used to retrieve the magnetisation of the sample.

The conventional TIE method consists in the acquisition of three images in underfocus, focus and overfocus, respectively. The reconstructed in-plane magnetisation of an FeGe sample with a mixed skyrmion-helical phase is shown in A.12. The crucial quantity in the TIE is the

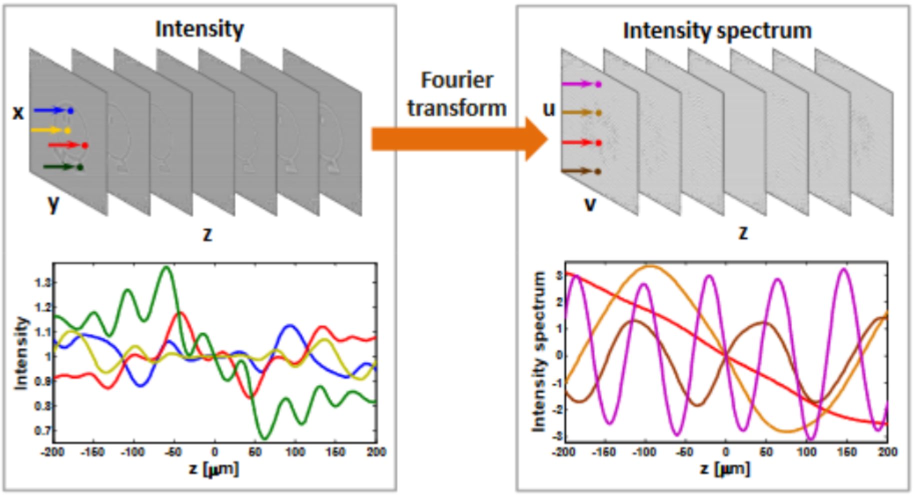

Figure A.11: The reconstruction of the intensity gradient is performed in Fourier space instead of real space. Taken from [113].

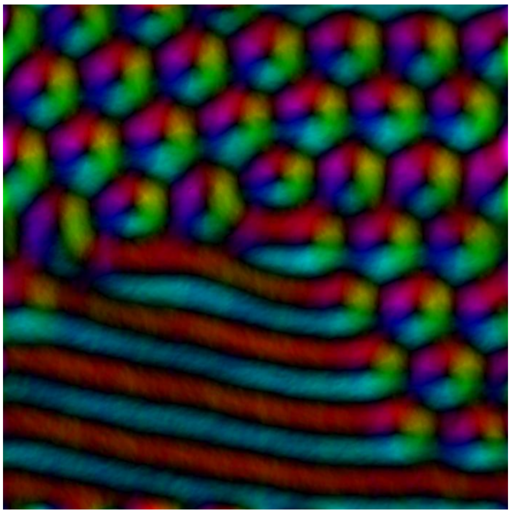

Figure A.12: Magnetisation of FeGe sample as obtained from normal TIE.

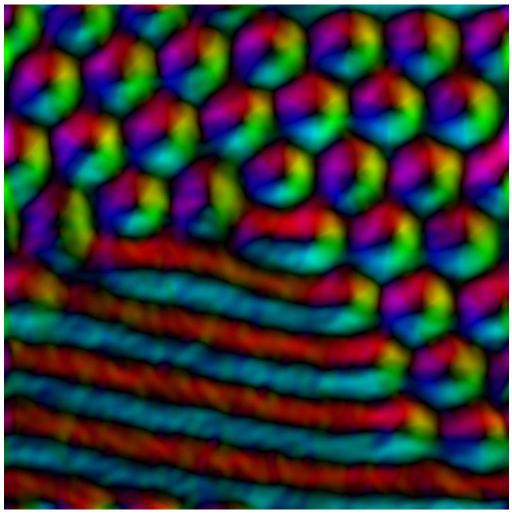

Figure A.13: Magnetisation of FeGe sample as obtained from improved TIE.

estimate of the intensity derivative. However, since intensity is not linear through focus, an estimate of the intensity derivative by finite differences will always be flawed. Generally, the trade off is between signal to noise ratio (high defocus, good for low frequency features in the image) and precision (small defocus to capture the high frequency details in the image). In an optics paper a few years ago [113] a different approach was adopted, see fig. A.11. A series of defocused images is acquired with an exponential spacing in defocus between them and the reconstruction of the intensity derivative is carried out in Fourier space instead of real space, which is much more robust in terms of noise. This is because we can incorporate prior knowledge of how different spatial frequencies are transmitted in a microscope and fit the data accordingly. In principle this approach allows us to capture both coarse and fine features in our images. Applied to magnetic imaging, we see the difference between the conventional TIE reconstruction, see fig. A.12, and the exponentially spaced defocus series, see fig. A.13. This is still work in progress and we will test other magnetic configurations where we expect the difference in quality to be more prominent (textures with both coarse and fine features ideally).

A.5.2 Heat-Induced Clockwise and Anticlockwise Rotation

A number of papers claim a unidirectional rotation of the skyrmion lattice when exposed to a thermal gradient, especially the one created by heating up the sample by electron beam radiation [114, 70]. In [114] the authors explains their observations by a flow of magnons created by the temperature gradient, which drives the rotation via the topological magnon Hall effect. However, depending on the beam intensity we observe both clockwise and anticlockwise rotation, as illustrated in figure A.14.

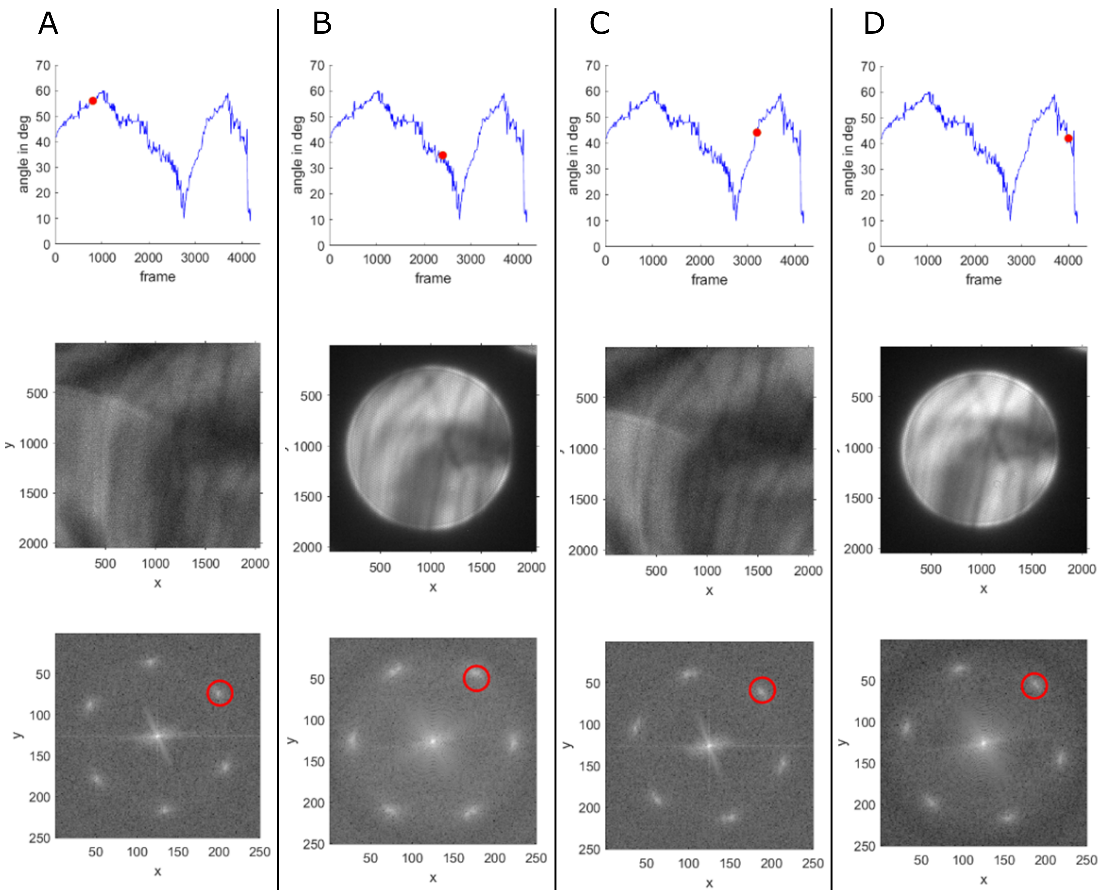

Figure A.14: Clockwise and counter-clockwise rotation of skyrmion lattice as a function of beam intensity.

Acknowledgements

First and foremost I would like to thank my supervisor Prof. Henrik Rønnow for having given me the opportunity to work in his lab for the last few years. I'm very grateful that he placed his trust in me even though he didn't know me and let me explore such a large spectrum of possibilities here at EPFL. When I was in doubt he would say: "just do it". His physical intuition and understanding are truly inspiring. I would also like to thank him for putting together such a wonderful group like LQM. Team spirit is strong and everybody is happy to share their knowledge.

I would like to thank Dr. Ivica Zivkovic as well for having given me the opportunity to come here and the warm welcome almost five years ago, when I first set foot into LQM.

I thank Prof. Fabrizio Carbone for the co-supervision of my thesis and allowing me to be part of LUMES as well. Ghil Berruto and Ivan Madan helped me a lot with their equipment during the first year when I could not use CIME's Titan yet. In the following years particularly Tom Lagrange was my point of reference for many TEM-related questions. He is a true wizard in TEM operation.

Ping Huang helped me a lot in the beginning stages to get up to speed with the project and we remained in close contact throughout the last years to collaborate on multiple projects. In many ways this is a continuation of his PhD work and the fruits of this thesis are the results of his efforts as well. He provided a great deal of valuable input for my research.

The help of Marco Cantoni was invaluable. He was available so many times when I had an issue on either the FIB or the Titan. It was often only thanks to him that I could continue with a sample prep or a TEM session late in the evening or during the weekend. He knows all the quirks of these complicated and sometimes capricious machines. Otherwise Lucie Navratilova was my go-to person when something was the matter with the FIB. Thanks to her, it was always well-maintained.

CMi is another fantastic facility. It offers state-of-the art tools for any microfabrication you can imagine. Its staff is always there to help with using the tools and working together with the users on their ideas to make them happen. I would particularly like to thank Cyrille Hibert, Julien Dorsaz and Joffrey Pernollet for all their input and help.

I had the chance to work within a larger project, the sinergia nanoskyrmionics, which allowed me to exchange with a large number of people who shared a common interest, many of whom were conveniently at EPFL as well: Ping Che, Anna Kukolova, Priyaranjan Baral, Arnaud Magrez, Alexey Sapozhnik and Jian-Rui Soh. Many thanks to Ping Che for the collaboration and helping me in the clean room.

A big thank you goes to Caroline Antonioli Pletscher for her kindness and helpfulness with all administrative matters. Many thanks go to Gerald Benney who always prepared the shiniest and most impeccable crystals but especially for all small and big chats about life. I would also like to thank Arnaud Magrez for providing the nice crystals I was working with and all the chats we had during the last years.

On a daily basis it was always a joy to be part of LQM and this is in large part thanks to the many people that have been there before me, that I have seen come and go and those who will stay for longer. Many of these people are not simply colleagues but friends. I had the chance to try out a few office mates and I have grown very fond of all them: Noore Elahi Shaik who I shared the office for the longest time, Giulia Mirabello, Alexia Vernier and during the last few months Youngroo Lee and Oleg Malanyuk. Even though Giulia's stay was short, I quickly became friends with this Italian whirlwind. The same is true for Alexia, who was by the way kind enough to suffer through the proofreading of this thesis. All other members of LQM helped to create special memories both inside and outside of EPFL: Bhushan Hegde, Saumya Shivam, Priyaranjan Baral, Luc Testa, Virgile Favre, Tarek Vennemann, Peter Babkevich, Ellen Fogh, Loic Favre, Yikai Yang, Jian-Rui Soh, Mina Akhyani, Jonathan Charrière, Daniil Yevtushynsky, Endre Horvath, Lidia Roccofort, Davor Tolj, Richard Gaal, Jana Pásztorová. I have so many great memories with all the cabanes, hikes and other trips we did together! Rarely have I met a person that is so reliably cheerful. Many thanks also go to Richard who knows every corner of the lab and always offered great advice. Thanks to all these people and the great atmosphere, there was not a single day I didn't want to go EPFL.

I had the chance to cross other people during my stay here who enriched my life in various ways: Vladimir Macko, Anton Malovichko, Renato Zanetti, Tzu-Hsien Shen (who also gave me probably the best tips in all matters concerning the clean room), Jonas Diaz, and many more.

I'm grateful for my parents' constant support and especially my Mom, who was and is always there for me. Regular visits back home helped me to re-energise and to overcome moments of sorrow.

In the first chapter I tried to give a flavour of what magnetism is all about. In French magnets are called 'aimants'. This last one therefore goes out to the thief who has taken my heart but has given me so much more in return. Stay close, for life is sweet when you're around.

Bibliography

[1] GM Turner. *North Pole, South Pole: The epic quest to solve the great mystery of Earth's magnetism.* The Experiment, 2011.

[2] AV Kimel, A Kirilyuk, PA Usachev, RV Pisarev, AM Balbashov, and T Rasing. Ultrafast non-thermal control of magnetization by instantaneous photomagnetic pulses. *Nature*, 435(7042):655–657, 2005.

[3] EM Purcell and DJ Morin. *Electricity and magnetism.* Cambridge University Press, 2013.

[4] RB Laughlin and D Pines. From the cover: The theory of everything. *Proceedings of the national academy of sciences of the United States of America*, 97(1):28, 2000.

[5] L Néel. Magnetism and the local molecular field. *Physics: 1963-1970*, 4:318, 1964.

[6] AS Disa, M Fechner, TF Nova, B Liu, M Först, D Prabhakaran, PG Radaelli, and A Cavalleri. Polarizing an antiferromagnet by optical engineering of the crystal field. *Nature Physics*, 16(9):937–941, 2020.

[7] S Mühlbauer, B Binz, F Jonietz, C Pfleiderer, A Rosch, A Neubauer, R Georgii, and P Boöni. Skyrmion lattice in a chiral magnet. *Science*, 323(5916):915–919, 2009.

[8] N Kazantsewa. *Dynamic response of the magnetisation to picosecond heat pulses.* PhD thesis, Universität Konstanz, 2008.

[9] C Schieback, M Kläui, U Nowak, U Rüdiger, and P Nielaba. Numerical investigation of spin-torque using the Heisenberg model. *The European Physical Journal B*, 59(4):429–433, 2007.

[10] WF Brown. *Magnetoelastic interactions*, volume 9. Springer, 1966.

[11] I Dzyaloshinsky. A thermodynamic theory of "weak" ferromagnetism of antiferromagnetics. *Journal of physics and chemistry of solids*, 4(4):241–255, 1958.

[12] T Moriya. Anisotropic superexchange interaction and weak ferromagnetism. *Physical review*, 120(1):91, 1960.

[13] T Moriya. New mechanism of anisotropic superexchange interaction. *Physical Review Letters*, 4(5):228, 1960.

[14] N Kanazawa, S Seki, and Y Tokura. Noncentrosymmetric magnets hosting magnetic skyrmions. *Advanced Materials*, 29(25):1603227, 2017.

[15] THR Skyrme. A non-linear field theory. *Proc. R. Soc. Lond. A*, 260:127–138, 1961.

[16] THR Skyrme. A unified field theory of mesons and baryons. *Nuclear Physics*, 31:556–569, 1962.

[17] H Vakili, J-W Xu, W Zhou, MN Sakib, MG Morshed, T Hartnett, Y Quessab, K Litzius, CT Ma, S Ganguly, MR Stan, PV Balachandran, GSD Beach, SJ Poon, AD Kent, and AW Ghosh. Skyrmionics—Computing and memory technologies based on topological excitations in magnets. *Journal of Applied Physics*, 130(7):070908, 2021.

[18] C Back, V Cros, H Ebert, K Everschor-Sitte, A Fert, M Garst, T Ma, S Mankovsky, TL Monchesky, M Mostovoy, N Nagaosa, SSP Parkin, C Pfleiderer, N Reyren, A Rosch, Y Taguchi, Y Tokura, K von Bergmann, and J Zang. The 2020 skyrmionics roadmap. *Journal of Physics D: Applied Physics*, 53(36):363001, 2020.

[19] A Fert, V Cros, and J Sampaio. Skyrmions on the track. *Nature nanotechnology*, 8(3):152–156, 2013.

[20] G Finocchio, F Büttner, R Tomasello, M Carpentieri, and M Kläui. Magnetic skyrmions: from fundamental to applications. *Journal of Physics D: Applied Physics*, 49(42):423001, 2016.

[21] Z Zhang, Y Zhu, Y Zhang, K Zhang, J Nan, Z Zheng, Y Zhang, and W Zhao. Skyrmion-based ultra-low power electric-field-controlled reconfigurable (SUPER) logic gate. *IEEE Electron Device Letters*, 40(12):1984–1987, 2019.

[22] KM Song, J-S Jeong, B Pan, X Zhang, J Xia, S Cha, T-E Park, K Kim, S Finizio, J Raabe, J Chang, Y Zhou, W Zhao, W Kang, H Ju, and S Woo. Skyrmion-based artificial synapses for neuromorphic computing. *Nature Electronics*, 3(3):148–155, 2020.

[23] M Garst, J Waizner, and D Grundler. Collective spin excitations of helices and magnetic skyrmions: review and perspectives of magnonics in non-centrosymmetric magnets. *Journal of Physics D: Applied Physics*, 50(29):293002, 2017.

[24] AA Kovalev and S Sandhoefner. Skyrmions and antiskyrmions in quasi-two-dimensional magnets. *Frontiers in Physics*, 6:98, 2018.

[25] B Göbel, I Mertig, and OA Tretiakov. Beyond skyrmions: Review and perspectives of alternative magnetic quasiparticles. *Physics Reports*, 895:1–28, 2021.

[26] R Suzuki. Recent development in magnetic-bubble memory. *Proceedings of the IEEE*, 74(11):1582–1590, 1986.

[27] S Paul, S Haldar, S von Malottki, and S Heinze. Role of higher-order exchange interactions for skyrmion stability. *Nature communications*, 11(1):1–12, 2020.

[28] AV Bezvershenko, AK Kolezhuk, and BA Ivanov. Stabilization of magnetic skyrmions by RKKY interactions. *Physical Review B*, 97(5):054408, 2018.

[29] XZ Yu, N Kanazawa, Y Onose, K Kimoto, WZ Zhang, S Ishiwata, Y Matsui, and Y Tokura. Near room-temperature formation of a skyrmion crystal in thin-films of the helimagnet FeGe. *Nature materials*, 10(2):106–109, 2011.

[30] S Seki, J-H Kim, DS Inosov, R Georgii, B Keimer, S Ishiwata, and Y Tokura. Formation and rotation of skyrmion crystal in the chiral-lattice insulator Cu_2OSeO_3. *Physical Review B*, 85(22):220406, 2012.

[31] B Balasubramanian, P Manchanda, R Pahari, Z Chen, W Zhang, SR Valloppilly, X Li, A Sarella, L Yue, A Ullah, P Dev, DA Muller, R Skomski, GC Hadjipanayis, and DJ Sellmyer. Chiral magnetism and high-temperature skyrmions in B20-ordered Co-Si. *Physical Review Letters*, 124(5):057201, 2020.

[32] Y Tokunaga, XZ Yu, JS White, HM Rønnow, D Morikawa, Y Taguchi, and Y Tokura. A new class of chiral materials hosting magnetic skyrmions beyond room temperature. *Nature communications*, 6(1):1–7, 2015.

[33] E Ruff, S Widmann, P Lunkenheimer, V Tsurkan, S Bordács, I Kézsmárki, and A Loidl. Multiferroicity and skyrmions carrying electric polarization in GaV_4S_8. *Science advances*, 1(10):e1500916, 2015.

[34] L Caretta, E Rosenberg, F Büttner, T Fakhrul, P Gargiani, M Valvidares, Z Chen, P Reddy, DA Muller, CA Ross, and GSD Beach. Interfacial Dzyaloshinskii-Moriya interaction arising from rare-earth orbital magnetism in insulating magnetic oxides. *Nature communications*, 11(1):1–9, 2020.

[35] K Litzius and M Kläui. Materials for skyrmionics. In *Magnetic Skyrmions and Their Applications*, pages 31–54. Elsevier, 2021.

[36] R Tomasello, E Martinez, R Zivieri, L Torres, M Carpentieri, and G Finocchio. A strategy for the design of skyrmion racetrack memories. *Scientific reports*, 4(1):1–7, 2014.

[37] S Seki, XZ Yu, S Ishiwata, and Y Tokura. Observation of skyrmions in a multiferroic material. *Science*, 336(6078):198–201, 2012.

[38] S Seki, S Ishiwata, and Y Tokura. Magnetoelectric nature of skyrmions in a chiral magnetic insulator Cu_2OSeO_3. *Physical Review B*, 86(6):060403, 2012.

[39] AJ Kruchkov, JS White, M Bartkowiak, I Živković, A Magrez, and HM Rønnow. Direct electric field control of the skyrmion phase in a magnetoelectric insulator. *Scientific reports*, 8(1):1–7, 2018.

[40] P Huang, M Cantoni, A Kruchkov, J Rajeswari, A Magrez, F Carbone, and HM Rønnow. In situ electric field skyrmion creation in magnetoelectric Cu_2OSeO_3. *Nano Letters*, 18(8):5167–5171, 2018.

[41] L Holzer and M Cantoni. Review of FIB-tomography. *Nanofabrication using focused ion and electron beams: Principles and applications*, 559201222:410–435, 2012.

[42] LA Gianuzzi. Lecture notes on FIB at Microscopy and Microanalysis 2018, Baltimore, 2018.

[43] B-S An, Y Kwon, J-S Oh, Y-J Shin, J Ju, and C-W Yang. Evaluation of ion/electron beam induced deposition for electrical connection using a modern focused ion beam system. *Applied Microscopy*, 49(1):1–5, 2019.

[44] C Pappas, E Lelievre-Berna, P Falus, PM Bentley, E Moskvin, S Grigoriev, P Fouquet, and B Farago. Chiral paramagnetic skyrmion-like phase in MnSi. *Physical review letters*, 102(19):197202, 2009.

[45] W Münzer, A Neubauer, T Adams, S Mühlbauer, C Franz, F Jonietz, R Georgii, P Böni, B Pedersen, M Schmidt, A Rosch, and C Pfleiderer. Skyrmion lattice in the doped semiconductor $Fe_{1-x}Co_xSi$. *Physical Review B*, 81(4):041203, 2010.

[46] XZ Yu, Y Onose, N Kanazawa, JH Park, JH Han, Y Matsui, N Nagaosa, and Y Tokura. Real-space observation of a two-dimensional skyrmion crystal. *Nature*, 465(7300):901–904, 2010.

[47] XZ Yu, N Kanazawa, Y Onose, K Kimoto, WZ Zhang, S Ishiwata, Y Matsui, and Y Tokura. Near room-temperature formation of a skyrmion crystal in thin-films of the helimagnet FeGe. *Nature materials*, 10(2):106–109, 2011.

[48] S Heinze, K Von Bergmann, M Menzel, J Brede, A Kubetzka, R Wiesendanger, G Bihlmayer, and S Blügel. Spontaneous atomic-scale magnetic skyrmion lattice in two dimensions. *nature physics*, 7(9):713–718, 2011.

[49] G Berruto, I Madan, Y Murooka, GM Vanacore, E Pomarico, J Rajeswari, R Lamb, P Huang, AJ Kruchkov, Y Togawa, T LaGrange, D McGrouther, HM. Rønnow, and F Carbone. Laser-induced skyrmion writing and erasing in an ultrafast cryo-Lorentz transmission electron microscope. *Physical review letters*, 120(11):117201, 2018.

[50] T Schönenberger, P Huang, LD Brun, L Guanghao, A Magrez, F Carbone, and HM Rønnow. Direct Visualisation of Skyrmion Lattice Defect Alignment at Grain Boundaries. *Nanoscale research letters*, 17(1):1–6, 2022.

[51] C Phatak, AK Petford-Long, and M De Graef. Recent advances in Lorentz microscopy. *Current Opinion in Solid State and Materials Science*, 20(2):107–114, 2016.

[52] R Tomasello, E Martinez, R Zivieri, L Torres, M Carpentieri, and G Finocchio. A strategy for the design of skyrmion racetrack memories. *Scientific reports*, 4(1):1–7, 2014.

[53] SSP Parkin, M Hayashi, and L Thomas. Magnetic domain-wall racetrack memory. *Science*, 320(5873):190–194, 2008.

[54] AA Omrani, JS White, K Prša, I Živković, H Berger, A Magrez, Y-H Liu, JH Han, and HM Rønnow. Exploration of the helimagnetic and skyrmion lattice phase diagram in Cu_2OSeO_3 using magnetoelectric susceptibility. *Physical Review B*, 89(6):064406, 2014.

[55] JS White, I Živković, AJ Kruchkov, M Bartkowiak, A Magrez, and HM Rønnow. Electric-Field-Driven Topological Phase Switching and Skyrmion-Lattice Metastability in Magnetoelectric Cu_2OSeO_3. *Physical Review Applied*, 10(1):014021, 2018.

[56] Y Nii, T Nakajima, A Kikkawa, Y Yamasaki, K Ohishi, J Suzuki, Y Taguchi, T Arima, Y Tokura, and Y Iwasa. Uniaxial stress control of skyrmion phase. *Nature communications*, 6(1):1–7, 2015.

[57] A Kukolova, S Escobar Steinvall, R Paul, J-B Leran, P Che, M Hamdi, A Mucchietto, D Grundler, and A Fontcuberta i Morral. van der Waals Epitaxy of $Co_{10-x}Zn_{10-y}Mn_{x+y}$ Thin Films: Chemical Composition Engineering and Magnetic Properties. *The Journal of Physical Chemistry C*, 125(17):9391–9399, 2021.

[58] HM Christen and G Eres. Recent advances in pulsed-laser deposition of complex oxides. *Journal of Physics: Condensed Matter*, 20(26):264005, 2008.

[59] LS Langston. Each Blade a Single Crystal. *American Scientist*, 103(1):30, 2015.

[60] RE Hummel. *Understanding materials science: history, properties, applications*. Springer, 1998.

[61] H-H von Grünberg, P Keim, and G Maret. Phase Transitions in Two-Dimensional Colloidal Systems. *Gerhard Gompper and Michael Schick, editors, Soft Matter*, 15(9):41—-86, 2007.

[62] N Romming, C Hanneken, M Menzel, JE Bickel, B Wolter, K von Bergmann, A Kubetzka, and R Wiesendanger. Writing and deleting single magnetic skyrmions. *Science*, 341(6146):636–639, 2013.

[63] N Romming, A Kubetzka, C Hanneken, K von Bergmann, and R Wiesendanger. Field-dependent size and shape of single magnetic skyrmions. *Physical review letters*, 114(17):177203, 2015.

[64] P Huang, T Schönenberger, M Cantoni, L Heinen, A Magrez, A Rosch, F Carbone, and HM Rønnow. Melting of a skyrmion lattice to a skyrmion liquid via a hexatic phase. *Nature Nanotechnology*, 15(9):761–767, 2020.

[65] K Karube, JS White, N Reynolds, JL Gavilano, H Oike, A Kikkawa, F Kagawa, Y Tokunaga, HM Rønnow, Y Tokura, and Y Taguchi. Robust metastable skyrmions and their triangular–square lattice structural transition in a high-temperature chiral magnet. *Nature materials*, 15(12):1237–1242, 2016.

[66] K Karube, JS White, D Morikawa, CD Dewhurst, R Cubitt, A Kikkawa, X Yu, Y Tokunaga, T Arima, HM Rønnow, Y Tokura, and Y Taguchi. Disordered skyrmion phase stabilized by magnetic frustration in a chiral magnet. *Science advances*, 4(9):eaar7043, 2018.

[67] XZ Yu, Y Tokunaga, Y Kaneko, WZ Zhang, K Kimoto, Y Matsui, Y Taguchi, and Y Tokura. Biskyrmion states and their current-driven motion in a layered manganite. *Nature Communications*, 5(1):1–7, 2014.

[68] J Rajeswari, P Huang, GF Mancini, Y Murooka, T Latychevskaia, D McGrouther, M Cantoni, E Baldini, JS White, A Magrez, T Giamarchi, HM Rønnow, and F Carbone. Filming the formation and fluctuation of skyrmion domains by cryo-Lorentz transmission electron microscopy. *Proceedings of the National Academy of Sciences*, 112(46):14212–14217, 2015.

[69] M Nagao, Y-G So, H Yoshida, T Nagai, K Edagawa, K Saito, T Hara, A Yamazaki, and K Kimoto. Real space observation of skyrmion polycrystallization and its domain boundary behavior in $FeGe_{1-x}Si_x$. *Applied Physics Express*, 8(3):033001, 2015.

[70] S Pöllath, J Wild, L Heinen, TNG Meier, M Kronseder, L Tutsch, A Bauer, H Berger, C Pfleiderer, J Zweck, A Rosch, and CH Back. Dynamical defects in rotating magnetic skyrmion lattices. *Physical review letters*, 118(20):207205, 2017.

[71] DR Nelson and BI Halperin. Dislocation-mediated melting in two dimensions. *Physical Review B*, 19(5):2457, 1979.

[72] S Deutschländer, P Dillmann, G Maret, and P Keim. Kibble–Zurek mechanism in colloidal monolayers. *Proceedings of the National Academy of Sciences*, 112(22):6925–6930, 2015.

[73] FA Lavergne, DGAL Aarts, and RPA Dullens. Anomalous grain growth in a polycrystalline monolayer of colloidal hard spheres. *Physical Review X*, 7(4):041064, 2017.

[74] J Wei, B Feng, R Ishikawa, T Yokoi, K Matsunaga, N Shibata, and Y Ikuhara. Direct imaging of atomistic grain boundary migration. *Nature Materials*, 20(7):951–955, 2021.

[75] T Meiners, T Frolov, RE Rudd, G Dehm, and CH Liebscher. Observations of grain-boundary phase transformations in an elemental metal. *Nature*, 579(7799):375–378, 2020.

[76] SL Zhang, WW Wang, DM Burn, H Peng, H Berger, A Bauer, C Pfleiderer, G Van Der Laan, and T Hesjedal. Manipulation of skyrmion motion by magnetic field gradients. *Nature communications*, 9(1):1–8, 2018.

[77] ND Mermin and H Wagner. Absence of ferromagnetism or antiferromagnetism in one- or two-dimensional isotropic Heisenberg models. *Physical Review Letters*, 17(22):1133, 1966.

[78] ND Mermin. Crystalline order in two dimensions. *Physical Review*, 176(1):250, 1968.

[79] JM Kosterlitz and DJ Thouless. Ordering, metastability and phase transitions in two-dimensional systems. *Journal of Physics C: Solid State Physics*, 6(7):1181, 1973.

[80] JM Kosterlitz. Kosterlitz–Thouless physics: a review of key issues. *Reports on Progress in Physics*, 79(2):026001, 2016.

[81] VL Berezinskii. Destruction of long-range order in one-dimensional and two-dimensional systems having a continuous symmetry group I. Classical systems. *Sov. Phys. JETP*, 32(3):493–500, 1971.

[82] VL Berezinskii. Destruction of long-range order in one-dimensional and two-dimensional systems possessing a continuous symmetry group. II. Quantum systems. *Sov. Phys. JETP*, 34(3):610–616, 1972.

[83] VN Ryzhov, EE Tareyeva, YD Fomin, and EN Tsiok. Berezinskii–Kosterlitz–Thouless transition and two-dimensional melting. *Physics-Uspekhi*, 60(9):857, 2017.

[84] BI Halperin and DR Nelson. Theory of two-dimensional melting. *Physical Review Letters*, 41(2):121, 1978.

[85] AP Young. Melting and the vector Coulomb gas in two dimensions. *Physical Review B*, 19(4):1855, 1979.

[86] T Knighton, Z Wu, J Huang, A Serafin, JS Xia, LN Pfeiffer, and KW West. Evidence of two-stage melting of Wigner solids. *Physical Review B*, 97(8):085135, 2018.

[87] JD Brock, A Aharony, RJ Birgeneau, KW Evans-Lutterodt, JD Litster, PM Horn, GB Stephenson, and AR Tajbakhsh. Orientational and positional order in a tilted hexatic liquid-crystal phase. *Physical review letters*, 57(1):98, 1986.

[88] M Cheng, JT Ho, SW Hui, and R Pindak. Observation of two-dimensional hexatic behavior in free-standing liquid-crystal thin films. *Physical review letters*, 61(5):550, 1988.

[89] CA Murray and DH Van Winkle. Experimental observation of two-stage melting in a classical two-dimensional screened Coulomb system. *Physical review letters*, 58(12):1200, 1987.

[90] RE Kusner, JA Mann, J Kerins, and AJ Dahm. Two-stage melting of a two-dimensional collodial lattice with dipole interactions. *Physical review letters*, 73(23):3113, 1994.

[91] U Gasser, C Eisenmann, G Maret, and P Keim. Melting of crystals in two dimensions. *ChemPhysChem*, 11(5):963–970, 2010.

[92] T Adams, A Chacon, M Wagner, A Bauer, G Brandl, B Pedersen, H Berger, P Lemmens, and C Pfleiderer. Long-wavelength helimagnetic order and skyrmion lattice phase in Cu_2OSeO_3. *Physical Review Letters*, 108(23):237204, 2012.

[93] JS White, K Prša, P Huang, AA Omrani, I Živković, M Bartkowiak, H Berger, A Magrez, JL Gavilano, G Nagy, J Zang, and HM Rønnow. Electric-Field-Induced Skyrmion Distortion and Giant Lattice Rotation in the Magnetoelectric Insulator Cu_2OSeO_3. *Phys. Rev. Lett.*, 113:107203, 2014.

[94] DR Nelson, M Rubinstein, and F Spaepen. Order in two-dimensional binary random arrays. *Philosophical Magazine A*, 46(1):105–126, 1982.

[95] K Zahn, R Lenke, and G Maret. Two-stage melting of paramagnetic colloidal crystals in two dimensions. *Physical review letters*, 82(13):2721, 1999.

[96] I Guillamón, R Córdoba, J Sesé, JM De Teresa, MR Ibarra, S Vieira, and H Suderow. Enhancement of long-range correlations in a 2D vortex lattice by an incommensurate 1D disorder potential. *Nature Physics*, 10(11):851–856, 2014.

[97] K Zahn and G Maret. Dynamic criteria for melting in two dimensions. *Physical Review Letters*, 85(17):3656, 2000.

[98] W Koshibae and N Nagaosa. Theory of skyrmions in bilayer systems. *Scientific Reports*, 7(1):42645, 2017.

[99] Y Suzuki, S Miki, Y Imai, and E Tamura. Diffusion of a magnetic skyrmion in two-dimensional space. *Physics Letters A*, 413:127603, 2021.

[100] Y Nishikawa, K Hukushima, and W Krauth. Solid-liquid transition of skyrmions in a two-dimensional chiral magnet. *Physical Review B*, 99(6):064435, 2019.

[101] J Iwasaki, AJ Beekman, and N Nagaosa. Theory of magnon-skyrmion scattering in chiral magnets. *Phys. Rev. B*, 89:064412, 2014.

[102] M Garst, J Waizner, and J Grundler. Collective spin excitations of helices and magnetic skyrmions: review and perspectives of magnonics in non-centrosymmetric magnets. *Journal of Physics D: Applied Physics*, 50(29):293002, 2017.

[103] P Dillmann, G Maret, and P Keim. Two-dimensional colloidal systems in time-dependent magnetic fields. *The European Physical Journal Special Topics*, 222(11):2941–2959, 2013.

[104] TWB Kibble. Topology of cosmic domains and strings. *Journal of Physics A: Mathematical and General*, 9(8):1387, 1976.

[105] TWB Kibble. Some implications of a cosmological phase transition. *Physics Reports*, 67(1):183–199, 1980.

[106] H Murayama and J Shu. Topological dark matter. *Physics Letters B*, 686(2-3):162–165, 2010.

[107] A del Campo. Colloidal test bed for universal dynamics of phase transitions. *Proceedings of the National Academy of Sciences*, 112(22):6780–6781, 2015.

[108] A del Campo and WH Zurek. Universality of phase transition dynamics: Topological defects from symmetry breaking. In *Symmetry and Fundamental Physics: Tom Kibble at 80*, pages 31–87. World Scientific, 2014.

[109] J Dziarmaga and WH Zurek. Quench in the 1D Bose-Hubbard model: Topological defects and excitations from the Kosterlitz-Thouless phase transition dynamics. *Scientific reports*, 4(1):1–6, 2014.

[110] H Watanabe, S Yukawa, Y Ozeki, and N Ito. Critical exponents of isotropic-hexatic phase transition in the hard-disk system. *Phys. Rev. E*, 69:045103, 2004.

[111] A Barman, G Gubbiotti, S Ladak, AO Adeyeye, M Krawczyk, J Gräfe, C Adelmann, S Cotofana, A Naeemi, VI Vasyuchka, et al. The 2021 magnonics roadmap. *Journal of Physics: Condensed Matter*, 33(41):413001, 2021.

[112] I Stasinopoulos, S Weichselbaumer, A Bauer, J Waizner, H Berger, S Maendl, M Garst, C Pfleiderer, and D Grundler. Low spin wave damping in the insulating chiral magnet Cu_2OSeO_3. *Applied Physics Letters*, 111(3):032408, 2017.

[113] Z Jingshan, RA Claus, J Dauwels, L Tian, and L Waller. Transport of intensity phase imaging by intensity spectrum fitting of exponentially spaced defocus planes. *Optics express*, 22(9):10661–10674, 2014.

[114] M Mochizuki, XZ Yu, S Seki, N Kanazawa, W Koshibae, J Zang, M Mostovoy, Y Tokura, and N Nagaosa. Thermally driven ratchet motion of a skyrmion microcrystal and topological magnon Hall effect. *Nature materials*, 13(3):241–246, 2014.

Thomas Schönenberger

+41 78 663 79 47
Chemin des Triaudes 4c
1024 Ecublens
thomas.schoenenberger@alumni.epfl.ch
LinkedIn (click):

Strengths

- Electron microscopy
- Experimental physics
- Data and image analysis
- Clean room microfabrication
- Material science and material characterization

Education

Ecole polytechnique fédérale de Lausanne (EPFL) — **Lausanne, Switzerland**
PhD in condensed matter physics — 2017-2022
Thesis: "Skyrmion Control and Phase Transitions in Cu_2OSeO_3"

Universität Konstanz — **Konstanz, Germany**
Master of Science in physics — 2014-2017
Thesis: "Numerical Studies of Magnetic Domain Structures in Temperature Gradients"
Grade: 1.2/6 ("very good")

Core Experience

Ecole polytechnique fédérale de Lausanne (EPFL) — **Lausanne, Switzerland**
PhD in experimental condensed matter physics — 2017-2022

I used **transmission electron microscopy (TEM)** and developed custom image analysis algorithms to investigate phase transitions in a magnetic material leading to the discovery of a new phase and a publication in Nature Nanotechnology. Another focus was on the development of prototypes of **low power memory devices** based on a new class of **magnetic materials**, which resulted in a first proof of concept.

- Development of new **device fabrication methods**
- Expert in clean room processes, **electron microscopy**, **micro-fabrication**, material characterization techniques and data analysis
- Automation of data acquisition and **data analysis**
- Automation of crystal growth procedures using advanced **image analysis** techniques
- **Supervision** of four master students, leading to one scientific publication
- Established collaborations across multiple labs at EPFL, Switzerland and in Denmark
- Presented results at prestigious international conferences (e.g. Microscopy and Microanalysis 2018 in Baltimore (USA) and APS March Meeting 2020 in Denver (USA)
- Lead projects to completion and publishing of results; two papers published in high impact journals (one paper in Nature Nanotechnology), one under review, two pending

Universität Konstanz — **Konstanz, Germany**
Master project in physics — 2015-2017

14 months project, **computer simulation and modelling** of magnetic systems, programming in C; development of a new theoretical model to explain the mechanism of magnetic domain wall movement induced by heat gradients; potential use in future magnetic storage devices

Institut Néel — **Grenoble, France**
Research intern — 2014

Four month internship; determination of crystal structures of new materials by electron diffraction using **transmission electron microscopy**; results led to a conference proceeding

Additional Experience

Ecole polytechnique fédérale de Lausanne (EPFL) — **Lausanne, Switzerland**
Teaching assistant and supervisor — 2017-2021

Teaching general mechanics, electrodynamics and thermodynamics for bachelor students and leading exercise sessions, preparation and correction of exams

Technical University of Denmark (DTU) **Kopenhagen, Denmark**
Visiting PhD student 2018

One month research stay to carry out experiments and establish collaborations

Summer School "New Trends in Chiral Magnetism" **Lausanne, Switzerland**
Co-organizer 2018

Co-organizer of a one week long summer school on “New Trends in Chiral Magnetism” on the campus of EPFL, organized together with students of three other European universities: TUM (Germany), TUe (Netherlands) and DTU (Denmark); budget planning, invitation of speakers; organizing accommodation, travel and social activities

IAESTE Konstanz **Konstanz, Germany**
Volunteer 2013-2016

Member of the local committee in Konstanz of the International Association for the Exchange of Students for Technical Experience (IAESTE): organizing internships in academia and industry for international students, accommodation, visa procedures, social outings

Skills

Programming and IT
- Matlab (data analysis and algorithm development for image analysis)
- Python (automation of data acquisition, communication with measurement devices)
- C (computer simulations)
- Latex (manuscripts, publications)
- MS office suite

Project management
- Supervision of four master students, leading to one scientific publication
- Organization and budget control of summer school (see additional experience)
- Defining the scope of all projects during the PhD and risk analysis

Microfabrication
- Focused Ion Beam (FIB, Zeiss NVision 40, FEI Nova 600)
- Gatan PIPS Argon-ion polisher for TEM sample preparation
- Clean room processes: photolithography (manual and automated coaters), lift-off, dry and wet etching, thin film deposition of metals and insulators, KOH etching of silicon

Characterization
- Transmission electron microscopy (TEM, FEI Talos, FEI Titan Themis, Philips CM200)
- Scanning electron microscopy (SEM, Zeiss Merlin)
- Energy-dispersive X-ray spectroscopy (EDXS)
- Laue X-ray diffraction for crystal orientation
- Light microscopy
- Electric transport measurements

Methods
- Soldering electronics
- Automating data acquisition procedures
- Automating data analysis of huge TEM data sets (thousands of TEM images)
- Image analysis, development of point detection and extraction algorithms

Languages

- German (native)
- English (C1-C2)
- French (B2-C1)
- Polish (B1-B2)
- Latin ("Latinum", 6 years of study)

Personal Interests

Road cycling with a focus on high mountain passes (Nufenen, Stilfser Joch, Furka, Grimsel,...), rowing, cooking, singing in a Gospel choir (bass), boardgames

Personal details

29, German citizenship, Swiss residence permit B; no military obligation; Swiss driver’s license (type B).